NTNU – Trondheim
Norwegian University of
Science and Technology

Microfluidic Fabrication of Mineralized Alginate Hydrogel Fibers

Stefan Mandaric

Nanotechnology
Submission date: June 2015
Supervisor: Pawel Tadeusz Sikorski, IFY
Co-supervisor: Bjørn Torger Stokke, IFY
Armend Gazmeno Håti, IFY

Norwegian University of Science and Technology
Department of Physics

Abstract

Alginates are a family of naturally occurring polysaccharides that form gels in the presence of Ca^{2+}-ions at physiological conditions. Calcium phosphate mineralized alginates have previously been investigated as a synthetic extracellular matrix in bone tissue engineering. The isotropic nature of hydrogels fails to mimic the directional structure observed at different lengths scales in bone tissue. A composite structure of calcium phosphate mineralized alginate fibers embedded in a matrix of unmineralized alginate gel has been suggested as a method for imitating the structure of bone tissue. The fabrication of mineralized alginate fibers for bone tissue engineering applications using microfluidic devices has been investigated in this work.

Fabrication of mineralized fibers was attempted using coaxial flow in microfluidic channels. A glass capillary microfluidic device was investigated to generate a coaxial flow of sodium alginate and phosphate ions surrounded by a flow of $CaCl_2$. The device was prone to clogging caused by buildup of alginate and minerals at the device surfaces.

A second microfluidic device was designed in an attempt to prevent clogging. A flow of DI water was flown between the sodium alginate and $CaCl_2$to act as a buffer delaying the onset of gelation until the flows cleared the device walls. Device geometries, flow rates and viscosities of the solutions were investigated to find parameters resulting in stable flow. Short lengths of calcium phosphate mineralized alginate fibers were successfully fabricated. Precipitation of CaP minerals and alginate buildup along device walls was decreased in the second device, but still resulted in device failure.

Mineralized fibers were shown to have a inhomogeneous structure with CaP minerals concentrated around the perimeter. Calcium phosphate minerals were observed in SEM micrographs as nano-sized sheets within the gel network. Mineralized fibers were found to have a higher resistance to deformation compared to unmineralized.

Further process development is required for stable fabrication of mineralized alginate fibers. A 3D microfluidic design has been proposed to further separate the sodium alginate flow from device walls in an attempt to prevent buildup of gel and minerals along device walls. In addition, an alternative mineralization process could be used where mineralization occurs outside the microchannels.

Sammendrag

Alginater er biopolymere som danner geler ved å binde Ca^{2+}-ioner. Alginater mineralisert med kalsiumfosfat har tidligere vært brukt som kunstig ekstracellulær matriks til vevsbygging av benvev. Hydrogeler har isotrop struktur som avviker fra den direksjonelle strukturen som er observert over flere lengdeskalaer i naturlig benvev. Et materiale bestående av mineraliserte alginatfibre omgitt av umineralisert alginat kan bli brukt til å imitere strukturen i benvev. Fabrikasjon av mineraliserte alginatfibre ved hjelp av mikrofluidikk vil bli undersøkt i denne oppgaven.

Mikrofluidiske kanaler bestående av glasspipetter har blitt brukt til å generere en koaksial flyt av natriumalginate og fosfationer omkranset av en løsning som inneholder $CaCl_2$. Natriumalginat dannet geler da Ca^{2+}-ioner diffunderte inn i strømmen. Mineralisert alginat bygget seg opp langs mikrokanelene, noe som resulterte i tette kanaler.

Et nytt mikrofluidisk system ble designet der en strøm av vann mellom natriumalginat og $CaCl_2$ble tilsatt for å utsette geling og oppbygging av mineraler langs veggene. Dimensjoner på kanaler, viskositet og pupmehastighet ble optimalisert. Mineraliserte fibre ble fabrikert i en kort periode før kanalene ble tettet som følge av alginate og mineraler langs veggene.

Mineraliserte fibre som ble fabrikert hadde en heterogen struktur der mineraler var konsentrert langs utkanten av fibrene. Mineraliserte fibere ble mindre deformert i løpet av preparasjonsproessen, noe som kan tyde på høyere stivhet i gelen.

Prosessen må forbedres for å oppnå stabil fabrikasjon av mineraliserte fibre. Et nytt tredimensjonalt mikrokanaldesign samt en alternativ mineraliseringskjemi kan benyttes for å redusere oppbygningen av materiale inne i mikrokanalene.

Preface

This report is the master thesis concluding Stefan Mandaric's master of technology degree in nanotechnology (MTNANO), specialization in bionanotechnology, study program at NTNU, completed in the spring semester of 2015. This thesis is an extensions of the author's project work *Microfabrication for mineralized, hydrogel-based materials for tissue engineering applications* [1] from the fall semester of 2014. For this reason some parts of the introduction, theory and methods chapters have been adapted from previous work. Some initial results and figures in section 4.1 have been adapted from the author's project thesis [1] as an introduction to and a reference for the following work.

Acknowledgements

I would like to thank my supervisor Pawel Sikorski for helpful guidance and advice throughout the completion of both my master thesis and preceding project work. A thank you is directed to my co-supervisor, Bjørn Torger Stokke, for generously allowing me to use the microfluidic setup in his lab. Thanks are also due to Armend Gazmeno Håti, for training and assistance with microfluidics. I would also like to thank David Bassett, Sindre Hove Bjørnøy and Jonas Myren Ribe for valuable discussions and insights.

Finally, but most importantly, I would like to thank Hege for her love, patience and support.

The Research Council of Norway is acknowledged for the support to NTNU NanoLab through the Norwegian Micro- and Nano-Fabrication Facility, NorFab (197411/V30). This work was partially supported through Research Council of Norway FRINATEK project ”Mineralized, hierarchical, bioinspired materials for tissue engineering” (project number: 214607).

Table of Contents

List of Figures

Abbreviations

ALP	=	Alkaline phosphatase
BSE	=	Backscattered electrons
CaA	=	Calcium (gelled) alginate
CaP	=	Calcium phosphate
CPD	=	Critical point dryer/critical point dried
ECM	=	Extracellular matrix
(FE)-SEM	=	(Field emission)-scanning electron microscope
HA	=	Hydroxyapatite
NaA	=	Sodium (ungelled) alginate
PDMS	=	Polydimethylsiloxane
PE	=	Primary electrons
PI^-	=	$H_2PO_4^-$, HPO_4^{2-} and PO_4^{3-} -ions
SE	=	Secondary electrons
V_{acc}	=	Acceleration voltage

1 Introduction

Trauma or diseases may cause bone defects that raise the need for substitute materials for repair and reconstruction. Conventional treatments include bone grafting, where bone is harvested from from the patient (autograft) or from a human donor (allograft) to fill the defects [2]. Limited availability of bone grafts and high risk of harvesting surgeries has led to the development of bone substitute materials based on metals, ceramics, polymers and composites. The limited ability of traditional biomaterials to modulate the repair and regeneration of host tissues has constrained their use for tissue-engineering applications and has motivated the development of new materials [3]. Fabrication of live biomaterials that integrate as a natural part of the tissue at the implant site are investigated as alternatives to traditional materials. Cell scaffolds are biomaterials that play the role of artificial extracellular matrix (ECM), providing a temporary environment to support cells to infiltrate, adhere, proliferate and differentiate[4, 5]. Cell scaffolds act as an initial structural support for retaining implanted or endogenous cells and promoting cell growth and matrix production. For maximal functionality, the scaffolds should mimic native tissue, and both functional and mechanical properties are important for the performance post implantation [6]. Bone can be regarded as a hybrid composite composed of a matrix of insoluble collagen scaffolds and nanoscale hydroxyapatite (HA) minerals, giving rise to a material with high stiffness, strength and low density rarely seen in man-made materials [7, 8] There is a great interest in the fabrication of cell scaffolds that can be mineralized in order to mimic bone structure and properties [9].

1.1 Alginates

Alginate systems have shown interesting results within bone regeneration when used as a cell delivery vehicle or to guide tissue repair providing a temporary ECM for cells to infiltrate and migrate while depositing new bone tissue[10]. Alginates are a family of naturally occurring polysaccharides found as a structural component in brown marine algae [11] and as capsular polysaccharides in Gram-negative bacteria *Pseudomonas* [12] and *Azotobacter* [13]. Brown algae, where alginate accounts for up to 40% of the dry

mass, are the main industrial source of the polysaccharide. Alginate forms gels at physiological conditions in the presence of Ca^{2+}-ions. Cell-friendly gelling conditions allow cells to be encapsulated in gels with the preservation of cell viability and function [14]. Alginates are generally biocompatible and ultrapure alginates are available, avoiding the toxicity and immunogenicity of minor contaminants present in conventional, industrial alginates [10]. Insulin-producing cells have been immobilized in alginate microbeads for immunosuppression-free islet transplantation for diabetes treatment [14]. Native alginates have had limited success in bone tissue engineering due to low stiffness and lack of specific contact with cells [3]. Recent advances in modifying the physical and chemical properties in alginate have shown improvement with regards to tissue engineering applications. Covalent binding of RGD-peptide to alginate has been shown to increase cell-matrix interaction and to facilitate differentiation of osteoprogenitor cell down the osteogenic lineage [15, 16] Biomimetic mineralization of alginate beads with hydroxyapatite (HA) has been shown to improve the stiffness of alginate [17, 18] and speed up mineralization by bone forming cells [19]. Alginate fibers have been proposed as a method for mimicking the anisotropic structure of bone at micrometer level. Fibers with a radial inhomogeneous mineralization would provide an isotropic environment that has been hypothesized to direct cell driven mineralization in a inhomogeneous pattern[6]. The fibers also present a convenient method of testing mechanical properties of mineralized alginate[20].

1.2 Aims of This Thesis

Biocomposites such as bone consist of directional structure at different length scales. Hierarchical structures in bone result in anisotropy, where mechanical properties are optimized for external loads in specific directions [8]. Hydrogels are isotropic in their mechanical properties, and mineralized alginate is expected to have isotropic mechanical properties as well. Directional structures may be achieved by dispersing mineralized alginate fibers into a alginate matrix as shown in Figure 1.1. The mineralized fibers could also contain encapsulated cells, and therefore serve as a cell delivery tool for seeding cells into the material in a controlled pattern. The fibers provide a mechanically anisotropic microenvironment that could direct encapsulated cells towards a specific deposition of mineral.

Methods for fabrication of fibers for tissue engineering found in literature include electrospinning, wetspinning, biospinning, interfacial complexation, microfluidic spinning and meltspinning (extrusion) [21]. In this work, two approaches based on microfluidic spinning are investigated as means of making phosphate mineralized calcium alginate fibers in the size range $10\,\mu\mathrm{m}$ – $200\,\mu\mathrm{m}$. Microfluidic spinning relies on a coaxial flow of a prepolymer and a crosslinking agent (sodium alginate and $CaCl_2$ solution, respectively, in the case of calcium alginate fibers) inside a microchannel. The short distance of coaxial flows ensures that encapsulated cells are only briefly exposed to high shear stresses and crosslinking agents. Fibers with diameters ranging from ten to several hundreds of $\mu\mathrm{m}$ can be fabricated with this method. In addition to channel dimensions, flow rates and viscosities of the solutions can be used to control fiber thickness [22]. A single device may therefore be used for fabrication of fibers in a wide range of thicknesses. Incorporation of living cells in calcium alginate fibers fabricated using microfluidic spinning has been

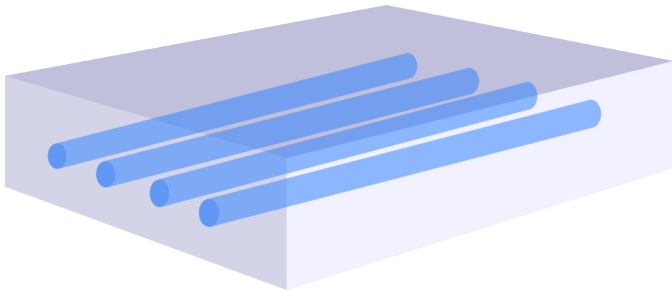

Figure 1.1: Proposed strategy for fabrication of hydrogel scaffolds for tissue engineering with anisotropic mechanical properties. Aligned fibers of mineralized alginate phosphate are dispersed in a non-mineralized alginate matrix. The resulting inhomogenous and anisotropic microenviroment may serve as a template for further mineralization by bone-forming cells.

investigated previously. Shin et al. [23] encapsulated human fibroblast cells in calcium alginate fibers generated by a glass capillary-based device. The authors demonstrated that the cells remained viable after seven days of culture.

Preliminary experiments in the author's project work [1] include microfluidic spinning of calcium alginate fibers in a glass capillary microfluidic device illustrated in Figure 1.2a. A solution of sodium alginate was flown through a pulled micropipette and surrounded by a sheath flow of $CaCl_2$gelling solution. Stable coaxial flow was achieved, resulting in fabrication of calcium alginate fibers. In this work, fabrication of phosphate mineralized calcium alginate fibers using glass capillary devices will be investigated. Simultaneous gelation and mineralization will be attempted using a counter-diffusion approach where phosphate ions are present in the sodium alginate flow. Based on results with glass capillaries a second device with an additional buffer flow between the alginate/phosphate and $CaCl_2$ flow shown in Figure 1.2b is tested. This device consists of rectangular microchannels in PDMS elastomer. Fabricated fibers will be characterized using optical and scanning electron microscopy.

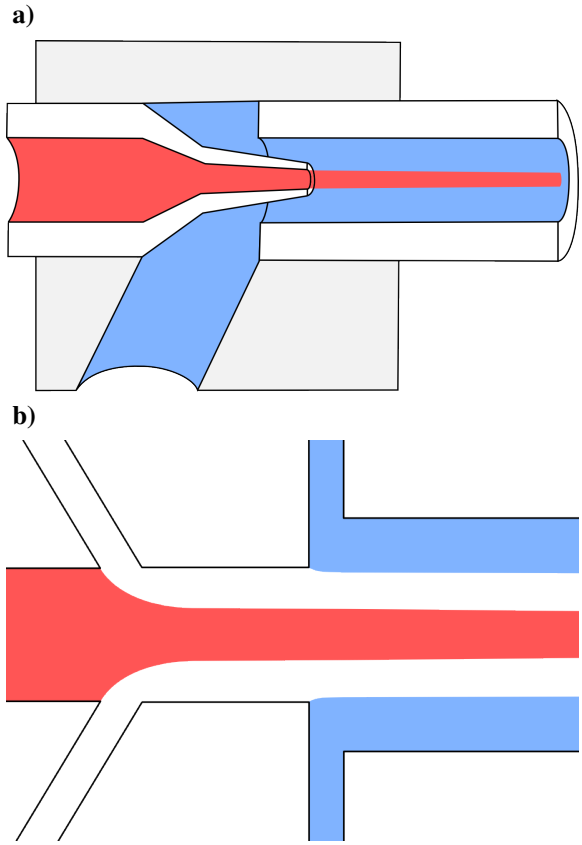

Figure 1.2: Two proposed devices for microfluidic fabrication of calcium alginate fibers. **(a)** A pulled glass pipette(white) is embedded in PDMS(grey) and contains a center flow of sodium alginate(red). Sheath flow of $CaCl_2$(blue) is supplied through a inlet hole in the PDMS. Gelation occurs in the outlet capillary as Ca^{2+}-ions diffuse into the sodium alginate flow. **(b)** Gelation is delayed by a buffer flow(white) between the sodium alginate(red) and $CaCl_2$(blue) flow. Calcium ions have to diffuse across the buffer flow in order for gelation to occur.

2 Theory

2.1 Stucture and Physical Properties of Alginate

Alginates are a family of unbranched polysaccharides consisting of 1,4-linked β-D-mannuronic acid residue(M) and α-L-guluronic acid residue(G). The G and M monomers are C-5 epimers, stereoisomers differing in configuration at the C-5 carbon atom as seen in Figure 2.1. The relative content of monomers as well as their sequential arrangement along the polysaccharide chain differs widely between sources. The fraction of G-residues (F_G) from algal sources varies between 0.4 and 0.7 [24]. Alginate from bacterial sources has greater variation in composition with F_G from 0.1 to 0.9 [25]. The uronic acid monomers appear in homopolymeric blocks (G and M-blocks) or blocks of alternating M and G-residues (MG-blocks). Composition and sequence of M and G blocks in alginate is determined by high-resolution ^{1}H and ^{13}C nuclear magnetic resonance spectroscopy (NMR)[26]. Alginate is a polyanion at physiological pH due to the low pKa values of mannuronic and guluronic acid (3.38 and 3.65, respectively)[27]. The majority of monovalent ions form soluble salts with alginate, whereas divalent cations form gels or precipitates[28].

2.1.1 Gel Formation

Alginate forms continuous networks by chelating divalent ions in intermolecular structures. The Eggbox Model describes the bound calcium as eggs in an eggbox-shaped structure formed by G-blocks[30]. Repeats of G-residues form cavities which serve as binding sites for ions, allowing intermolecular bonds between G-blocks in adjacent chains. As soon as an initial junction between two G-blocks has been made, adjacent molecules in the G-block will align an in an cooperative manner form a eggbox structure. The affinity of G-blocks for cations in increasing order is: $Mg^{2+} \ll Ca^{2+} < Sr^{2+} < Ba^{2+}$[28]. A minimum of 8 to 20 adjacent G residues are needed to form stable junctions in the presence of Ca^{2+}[31]. The eggbox model predicts a maximum binding capacity of 3/4 Ca^{2+}-ions per G-residue at high cation concentrations[32]. MG-blocks are also known to form crosslinks with Ca^{2+},

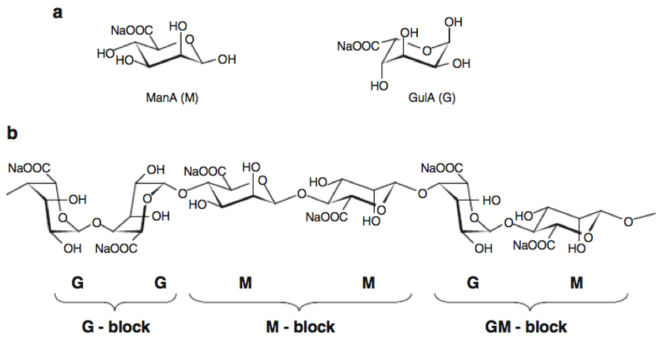

Figure 2.1: Composition of alginate[29]. **a** $^4C_1$ conformation of β-D-mannuronic acid (M) and $^1C_4$ conformation of α-L-guluronic acid (G) **b** A sequence of a G, M and GM block showing ring conformations

either between MG-blocks in two alginate chains or MG-blocks in one chain and G-blocks in another chain[33]. MG-blocks bind $Ca^{2+}$with lower affinity than G-blocks. G blocks play an essential role gelling of alginate since chains consiting exclusively of M-blocks are incapable of forming a gel with calcium[34]. The main structural feature determining gel properties is the M/G composition, giving alginate gels wiht high M content lower strength and stability compared to gels made from high-G alginates[35].

Alginate gels may be made by internal gelation where calcium is supplied by a source within the gel, or external gelation where $Ca^{2+}$from an external reservoir diffuses into the alginate. Formation of alginate beads by external gelation may be accomplished by dripping high molecular weight Na-alginate into a gelling bath of Ca^{2+}-ions as illustrated in figure 2.3. Gelling of the bead surface takes place immediately upon contact with the gelling solution. Gelling is restricted to in a narrow region termed the *gelling region*, that forms around the bead perimeter and travels inwards towards the center of the bead. Movement of the gelling front shows a sqare root of time dependence, indicating the inwards diffusion of Ca^{2+}-ions as the rate detendening factor for the gelling reaction [36]. The change in refractive index that occurs during gelling allows the gelling front to be visualized in phase contrast microscopes[1]. The resulting alginate gel beads will have an inhomogeneous structure with decreasing alginate concentration of alginate in the center caused by the coupled outwards diffusion of alginate and sodium ions.[37]. Adding 0.9% NaCl to the NaA and gelling solution results in more homogenous beads[38].

2.1.2 Calcium Phosphate Mineralized Alginate Gels

Calcium orphophosphates are a variety of calcium phosphates that contain the orthophosphate (PO_4^{3-}) anion[40]. Although other calcium phosphates exist, focus is placds on calcium orthophosphates (from now on refered to as calcium phosphates) because they are the major component of all calcified biological tissues[41]. The phosphate ion carries a negative-three formal charge and is the conjugate base of the hydrogen phosphate ion,

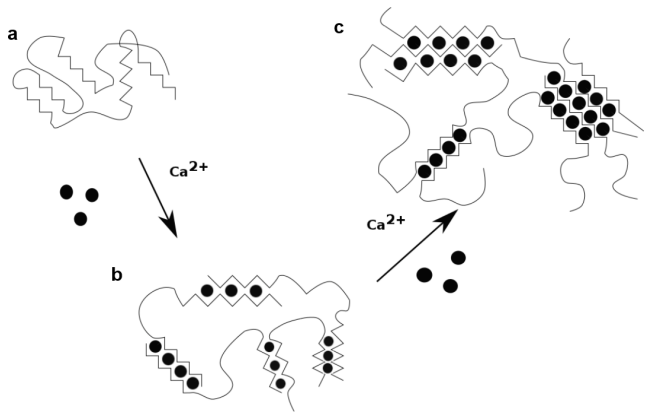

Figure 2.2: The egg-box model of alginate gelling adapted from [39]. **a** Alginate molecule in solutions. The zig-zag regions repsresent G-blocks. **b** Intermolecular bonds between G-blocks are made by chelating Ca^{2+}-ions. **c** Eggboxes grow laterally as Ca^{2+}-concentration increases

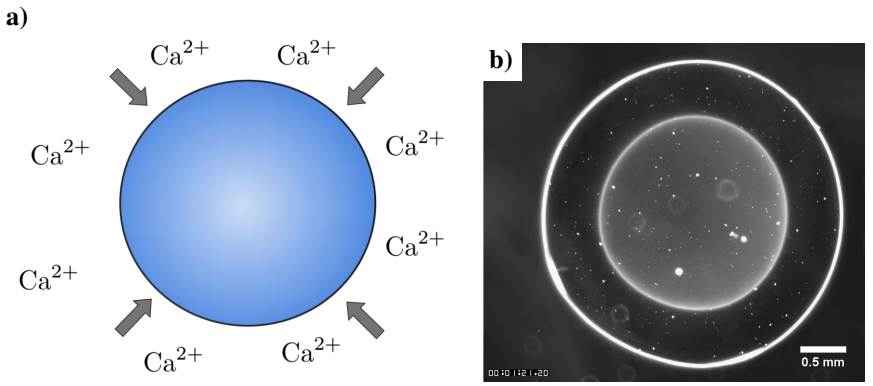

Figure 2.3: External gelation of sodium alginate spheres. **(a)** Ca^{2+}-ions diffuse into the alginate sphere, resulting in inital gelling on the surface which then moves inwards. **(b)** Gelling of a alginate disc takes place in a narrow gelling region that is visible in phase contrast micropes as a bright ring moving towards the center of the disc. The scale bar is $0.5\,\mathrm{mm}$ Image from project thesis [1].

HPO_4^{2-}, which is the conjugate base of $H_2PO_4^-$, the dihydrogen phosphate ion, which in turn is the conjugate base of H_3PO_4, phosphoric acid. The pK_a values for each of the three dissociation reaction are 2.12, 7.21 and 12.67. Phosphates in aqueous solution exist in various degrees of protonation depending on the pH of the solution. At neutral pH, aqueous phosphate solutions consist of $H_2PO_4^-$ and HPO_4^{2-} in the ratio 61.7/38.3. The abbreviation $PI^-$is used for phosphate ions of all degrees of protonation in this text. Calcium phosphates comprise a complex sytem where the stoichiometry, solubility and acidity is different for the various crystalline phases. There are 13 known calcium orthophosphates[40], but not all are stable in aqueous solution at biological conditions. Factors including, pH, temperature, biological molecules, and time affect what type of minerals are formed. The main constituents of human bones are calcium orthophosphates ($\sim$ 60-70 wt%), collagen ($\sim$ 20-30 wt%) and water (up to 10 wt%)[40]. Calcium phosphate in bone occurs mainly in the form of poorly crystalline, non-stoichometric, calcium-deficient, Na-, Mg- and carbonate-containg Hydroxylapatite ($Ca_{10}(PO_4)_6(OH)_2$), often called "biological apatite" (BAp)[42]. Bioapatite crystals exists in the form of $3\,\mathrm{nm}$ thick plate-shaped particles found in the gap regions between collagen fibrils [8, p. 293].

Pure HA is never found in biological system, but is used as a coating on orthopedic implants as its presence on the surface generally improves the guidance of bone tissue along implant surface[43]. HA nanoparticles can control the stiffness of flexible hydrogels, similarly to their reinforcing function in bone tissue. The resulting increase of matrix stiffness has been shown to influence the differentiation of cells towards the osteoblastic (bone forming) phenotype[44].

Mineralized alginate hydrogels may be produced by a counter diffusion method [45] outlined in Figure 2.4, where sodium alginate solution containing high concentrations of phosphate is dripped into a bath of calcium chloride ions. Diffusion of Ca^{2+}-ions into the NaA leads to a simultaneous Ca^{2+}-binding in alginate which leads to gelling as well as precipitation of calcium phosphate (CaP) minerals. Gelling and mineralization occurs in a moving-front fashion shown in Figure 2.4. Phosphate has been shown to slow down the gelling of alginate visualized by slowed movement of the gelling front[1]. The precipitation of CaP minerals consumes Ca^{2+}-ions which results in a smaller amount of Ca^{2+}-ions that are free to bind with alginate resulting a slowed gelling. The outwards counter-diffusion of phosphate results in an inhomogeneous mineral distribution in the gel. Calcium phosphate produced by the counter-diffusion exists predominately in the form of nano-sized HA with low crystallinity [46], similar to the minerals found in bone. The resulting mineralized hydrogels show increased elastic modulus [47]. Human mesenchymal stem cells encapsulated in mineralized alginate beads have been shown to respond by further mineralizing the beads[44]. Both mineralized and non-mineralized alginate beads were shown to provide an environment that enhanced osteogenic differentiation in human mesenchymal stem cells compared with traditional 2D culture.

2.2 Photolithography

Photolithography is extensively used in microfabrication for selective patterning of substrates. The process is commonly used in rapid prototyping in microfluidics to create microstructures that serve as reusable molds for PDMS devices. Light (typically ultra-

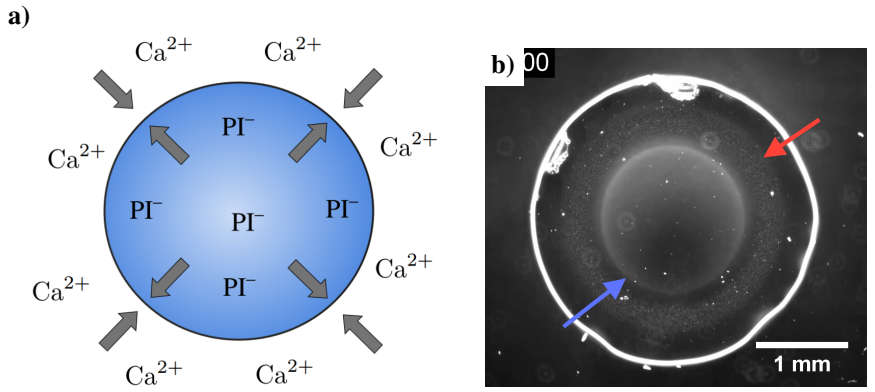

Figure 2.4: Mineralized alginate gels formed by simultaneous Ca^{2+}-induced gelation and precipitation. **(a)** Phosphate ions (PI^-) diffuse outwards as mineralization decreases the concentration in the gelled/mineralized regions. **(b)** The gelling front indicated by blue arrows is weaker and moves slower compared to previous experiments without phosphate. A moving front of minerals indicated by red arrows follows the gelling front and widens over time. Figure adapted from project work[1].

violet, UV) is used to transfer a geometric pattern from a photomask to a thin film of light-sensitive chemical ”photoresist” or ”resist”. Photomasks typically consist of UV transparent soda-lime glass substrate with opaque features of Chromium (Cr) thin film. Photomasks are designed in CAD-software and printed using electron beam lithography (EBL) to achieve sub-micron pattern resolution. Photomasks made from polyester films are an inexpensive alternative to soda-lime masks when high resolution ($< 8\,\mu m$) is not required [48]. The stages in a typical photolithography process for a negative resist are outlined in Figure 2.5. A Si wafer substrate is sprayed with solvents and/or plasma treated to remove contaminants from the surface and improve resist adhesion. The wafer is dehydration baked on hotplates at high temperatures ($> 180\,°C$) to remove adsorbed water molecules from the surface. An uniform layer of resist with controlled thickness is applied using spin coating. Spin parameters (spin speed, spin time and ramp rate) and resist properties (solvent chemistry and viscosity) control film thickness. The spin coated wafer is heated to evaporate excess solvent and improve adhesion between resist and wafer and to prevent the resist from sticking to the mask during exposure. A mask aligner is used to selectively expose area of the resist with UV light. A photomask is placed in contact with the substrate, limiting UV exposure to transparent regions of the mask. Required exposure dose is determined by resist type and thickness. In the case of negative resists, exposure initiates photochemical reactions that decreases the solubility of the resist. A post-exposure baking step increases the kinetics of the photochemical reaction. The sample is submerged in a developer solution which selectively dissolves non-exposed resist, leaving resist structures corresponding to transparent features (a negative image) on the photomask. The resulting photoresist features may either form permanent structures or serve as temporary masks for subsequent etching or deposition processes.

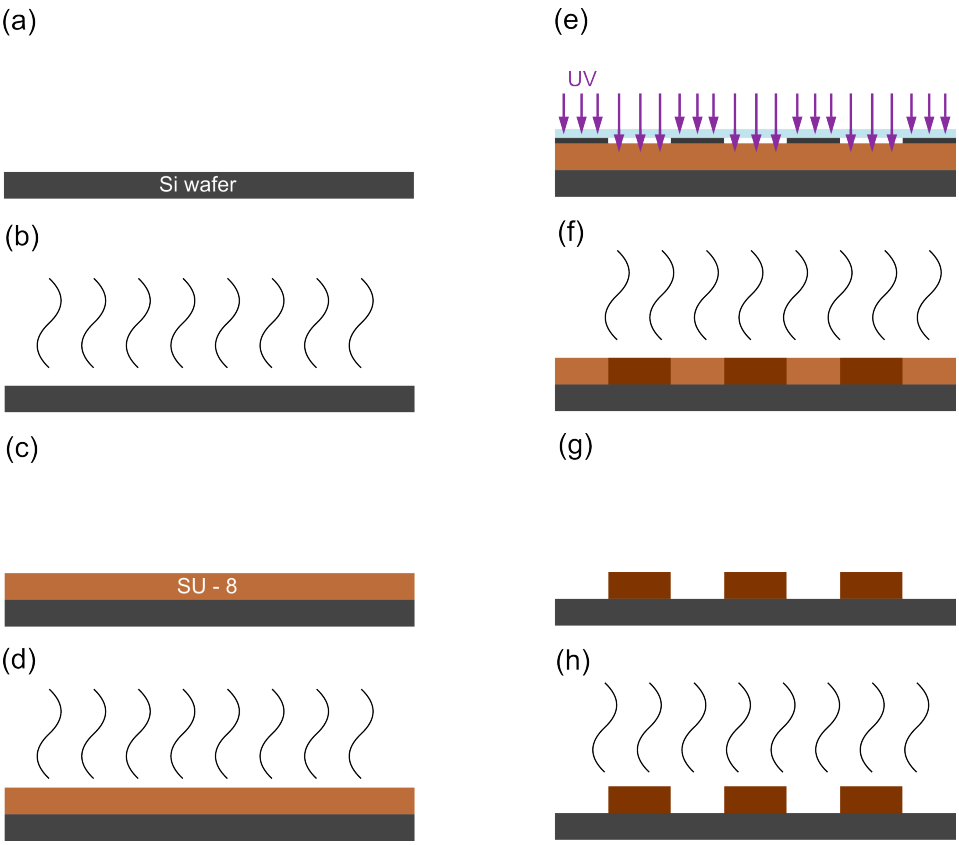

Figure 2.5: Steps in a typical photolithography process with negative SU-8 resist. **(a)** Wafer clean: Spraying with solvents and/or plasma cleaning to remove surface contaminants **(b)** Dehydration bake: remove absorbed water molecules from the surface **(c)** Spin coating: a thin layer of photoresists with controlled thickness is uniformly applied **(d)** Soft-bake: heat treatment to evaporate excess solvents **(e)** Alignment and exposure: selective irradiation to initiate photoresist cross-linking **(f)** Post-exposure bake: promotes cross-linking of the exposed resist **(g)** Development: selective etching of non-exposed photoresist **(h)** Optional hard bake step if the resist forms a permanent layer of the structure

2.2.1 SU-8 Photoresist

SU-8 is an epoxy-based negative tone resist commonly used in high aspect ratio photolithography [49]. SU-8 photoresist may be used for films with thickness range up to $500\,\mu\mathrm{m}$ for a single coating and $1200\,\mu\mathrm{m}$ when multiple coatings are applied[50]. Features with up to 20:1 aspect ratios have been achieved in SU-8 using optimized UV lithography [51]. High chemical and mechanical stability after processing enables use of SU-8 as a mold material for PDMS-based microfluidics[52]. The main components of SU-8 are a Bisphenol A Novolak epoxy oligomer resin and triarylsulfonium hexafluroantimonate salt photoacid generator[49]. Cyclopentanone is used as a solvent to enable the resist to be applied using spin-coating. Solvent content and chemistry determines viscosity and wetting properties of the resist, which is important for thickness and uniformity of the resist film. Excess solvent is evaporated during the soft-baking step, leaving behind a film of photoacid generator and epoxy resin. Irradiation of the resist is typically performed using the i-line of mercury lamps corresponding to a wavelength of 365 nm. The photoacid generator in irradiated regions of the resist decomposes to form acid that protonates the epoxides on the oligomer. The protonated groups undergo cross-linking with neutral epoxides when temperature is increased in the post-exposure baking step. The cross-linking results in insoluble resist in irradiated areas. Development performed by immersion in propylene glycol methyl ether acetate which removes unexposed resist, leaving behind features corresponding to transparent regions of the photomask.

2.2.2 Mask Alignment and Exposure

Mask aligners are used to align the photomask with the light-sensitive substrate and control exposure. Depending on mask aligner design, the mask is either in direct contact with the substrate, in close proximity or the mask is projected on to the sample using an optical system[53]. Direct contact, also known as hard contact, minimizes diffraction by bringing the mask in direct contact with the substrate. Hard contact is prone to contamination of both the substrate and the mask. Resolution problems arise in the immidiate area around a particle. For proximity contact, or soft contact, the mask is positioned $2.5\,\mu\mathrm{m}$ to $25\,\mu\mathrm{m}$ above the substrate. Resolution is lower compared to hard contact because of light scattering of UV rays passed through the mask. Proximity contact is less prone to contamination and mask wear is reduced. Projection aligners employ a mirror system to project a mask with a 1:1 image onto the wafer surface. Projection aligners are mainly used in IC fabrication while contact aligners are most common in research.

2.3 Soft Lithography

Soft lithography is a set of methods for micro- and nanofabrication that rely on a patterned ”soft” elastomer as the mask, stamp or mold. Soft lithography techniques include microcontact printing, replica molding, microtransfer molding and micormolding in capillaries[54]. Patterns and structures with lateral dimensions of about $30\,\mathrm{nm}$ to $500\,\mu\mathrm{m}$ can be fabricated, with several advantages over traditional photolithograpy-based microfabrication. Soft lithography is not limited by optical diffraction or optical transparency

and does not require advanced photolithographic procedures. Soft lithography is applicable to a wide array materials whereas photolithography is limited to photoresists and traditional semiconductor materials. Most importantly, soft lithography enables low-cost and rapid micro/nanofabrication that can be performed in ambient laboratory environments.

2.3.1 PDMS

Poly(dimethylsiloxane) (PDMS) is a elastomer commonly used for channels in microfluidics fabricated by soft lithograpy. PDMS is a silicon-based organic polymer with the repeating unit $SiO(CH_3)_2$. PDMS used in casting is supplied in two components, a base and a curing agent. Silicon hydride (Si-H) groups present in the curing agent react with vinyl groups $SiCH{=}CH_2$ in the base, cross-linking the polymer[55]. Curing is typically performed at elevated temperatures to speed up the process. Cross-linking results in the formation of a elastomeric imprint of the mold. The low surface energy and high elasticity of PDMS allows the cured polymer to be released from the mold without damaging the features. PDMS is optically transparent for wavelengths down to $300\,\mathrm{nm}$, allowing channels to be observed with optical and fluorescence microscopy [54]. The surface of unmodified PDMS is hydrophobic[56]. Hydrophobic PDMS channel walls are difficult to wet with aqueous solutions and prone to adsorbion of hydrophobic contaminants. Treatment with oxygen plasma renders the surface hydrophilic due to the formation of silanol groups on the surface. The oxidized PDMS surface is unstable in air and reverts to a hydrophobic state over time.

2.3.2 Replica Molding

Replica molding duplicates the shape, morphology and structure present in a master by casting with an elastomer such as PDMS as shown in Figure 2.6. Masters are typically produced by photolithography and serve as reusable molds. A prepolymer mix of PDMS base and curing agent is poured into the mold and conforms to the three dimensional shape of the mold. After curing, the elastomer is peeled of resulting in an inverted copy of the mold. Replica molding is a reliable, simple and inexpensive method of replicating structures in the master with nanometer resolution. Once peeled from the mold the PDMS replica must be sealed to a flat surface to form enclosed channels. The sealing surface can be PDMS or another material, typically glass. Reversible sealing occurs when the PDMS is brought into contact with a flat surface. The PDMS can conform to minor imperfections of the surface and form van der Waals bonds that are reversed by simply peeling the PDMS off of the surface. Reversible bonding occurs at room temperature and forms watertight seals capable of withstanding low pressures ($< 30\,\mathrm{kPa}$)in the capillaries[56]. Peeling PDMS off the surface breaks the reversible bonds. Irreversible seals to certain materials are made by exposing both surfaces to oxygen plasma before bringing them into contact. The oxygen plasma introduces silanol groups ($Si{-}OH$) at the expense of methyl groups ($Si{-}CH_3$) [57]. Silanol groups condense and form covalent $Si{-}O{-}Si$ bonds with glass. Irreversible bonds are capable of withstanding higher pressures of $200\,\mathrm{kPa}{-}350\,\mathrm{kPa}$ [56]. Peeling will result in the bulk PDMS breaking.

Durability of the mold is improved by silanization treatment to prevent the elastomer from sticking. The mold is exposed to silane vapor which forms covalent $Si{-}O{-}Si$ bonds

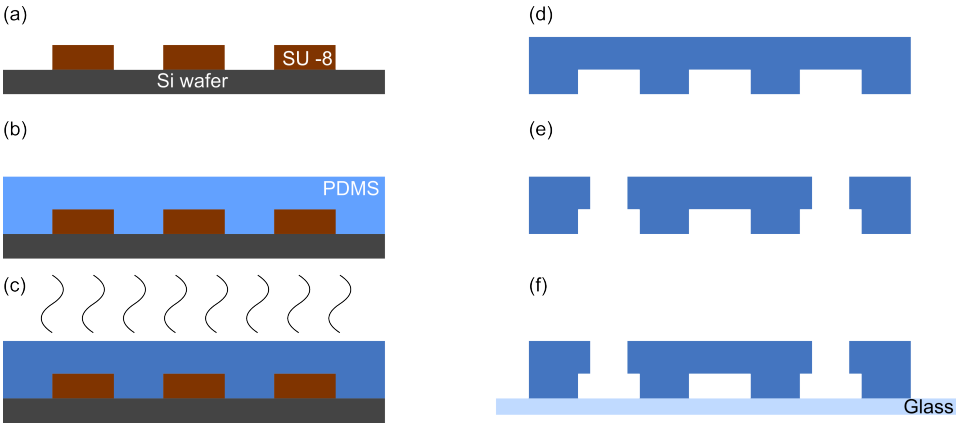

Figure 2.6: Typical steps in replica molding of microfluidic channels. **(a)** A SU-8 patterned silicon wafer is silanized to reduce adhesion between PDMS and the master. **(b)** A prepolymer mix of PDMS base and curing agent is pored into the mold. **(c)** PDMS cross-linking is accelerated by baking in an oven. **(d)** The cross-linked PDMS is peeled off the master. **(e)** Holes are punched for inlets and outlets. Debrees are removed with adhesive tape. **(f)** The PDMS is permanently bonded to a glass slide in order to form closed channels.

with the substrate. The silanized mold can be used to fabricate more than 50 PDMS replicas [54].

2.4 Flow in Microchannels

Microchannels can be defined as channels whose dimensions are less than $1\,\mathrm{mm}$ and greater than $1\,\mu\mathrm{m}$[58]. Flows in microscale devices are dominated by factors such as surface tension and fluidic resistance, far exceeding body forces such as gravity or electrostatic fields[59]. Microfluidics can be used to achieve high control over chemical and physical properties such as concentration, temperature, shear force, reaction time, etc. resulting in more uniform reaction conditions[60]. This section provides a brief introduction to concepts in fluid mechanics relevant to microfluidic fiber fabrication.

2.4.1 Viscosity

The viscosity of a fluid measures its resistance to gradual deformation by shear or tensile stress[61]. The viscosity μ represents the relation between applied shear stress τ and shear rate $\dot{\gamma}$:

$$\tau = \mu\dot{\gamma} \tag{2.1}$$

Materials that satisfy the linear relation between stress and strain in equation 2.1 are referred to as Newtonian fluids. Most small molecule solutions such as water are Newtonian. Non-newtonian fluids have a shear rate depending viscosity $\mu(\dot{\gamma})$, resulting in a non-linear

relation between stress and strain. Viscosity of a liquid is given via the power law equation:

$$\mu = K\dot{\gamma}^{n-1} \tag{2.2}$$

where $n > 2$ for shear thickening fluids, $n < 2$ for shear-thinning fluids and $n = 2$ for Newtonian fluids. K is a constant for the liquid. Diluted polymer solutions as well as blood and aqueous solutions of proteins are examples of non-newtonian fluids.
Shear rate $\dot{\gamma}$ quantifies the rate at which a shearing deformation is applied to a material. The share rate for Couette flow, a fluid flowing between two parallel plates, one moving at constant speed and the other one stationary is[61]

$$\dot{\gamma} = \frac{v}{h} \tag{2.3}$$

where v is the velocity of the moving plate and h is the distance between the plates. Shear rates for Couette flow serve as an order of magnitude estimate for shear rate where h is the smallest dimension of the flow[62]. Microfluidic flows are prone to high share rates and share stresses due to small channel dimensions.

2.4.2 The Reynolds Number

The Reynolds number is defined as the ratio of inertial forces to viscous forces and quantifies the relative importance of these two types of forces[63]. The Reynolds number is used to quantify flow, mixing and thermal transfer characteristics of fluids across different media and length scales[61]. For flow in a straight channel, the Reynolds number is defined as:

$$\mathrm{Re} = \frac{\rho V D_H}{\mu} \tag{2.4}$$

where ρ is the fluid density, V is fluid velocity and μ is the viscosity of the fluid. D_H is the hydraulic diameter, which equals the diameter in the case of a pipe geometry. For a square channel of height *h* and width *w*, the hydraulic diameters is:

$$D_H = \frac{2wh}{w+h} \tag{2.5}$$

Flows with low Reynolds number are dominated by viscous forces. Laminar flow occurs for Re below a threshold value (< 2100 in a pipe[64, p. 207]) and can be described by parallel sheets of fluid that flow past each other with no disruption between the sheets. There are no currents perpendicular to the flow direction, nor swirls or eddies. Mixing between the layers is limited to diffusion only. For low Reynolds numbers, the flow field is time independent for a steady driving force for the flow. For Re greater than a threshold value (> 4000 in a pipe[64, p. 207]), the fluid enters the turbulent flow regime characterized by chaotic flow behavior with rapid variation of pressure and flow velocity in time and space that results in increased lateral mixing. Microfluidic systems are generally dominated by laminar flow due to low flow velocity and characteristic length, which results in low Re conditions.

2.4.3 Governing Equations

The governing laws of fluid motion can be derived using a control volume approach and conservation laws. Mass is conserved in a control volume which gives the continuity equation:

$$\frac{\partial \rho}{\partial t} + \nabla \cdot (\rho \mathbf{v}) = 0 \tag{2.6}$$

where ρ is the density and $\mathbf{v}$ is the velocity of the flow. Liquids are commonly assumed to be incompressible and density is treated as constant. This leads to the continuity equation for incompressible materials:

$$\nabla \cdot \mathbf{v} = 0 \tag{2.7}$$

The Navier-Stokes equations are based on the law of conservation of momentum on a control volume and describe the motion of viscous fluid substances. With incompressible flow and constant viscosity, the Navier–Stokes equations read[65]:

$$\rho \left(\frac{\partial \mathbf{v}}{\partial t} + \mathbf{v} \cdot \nabla \mathbf{v} \right) = -\nabla p + \mu \nabla^2 \mathbf{v} + \mathbf{f} \tag{2.8}$$

where $\mathbf{v}$ is the flow velocity, p is the pressure and f represents body forces. Although the Navier-Stokes solutions can not be found in the general case, for certain geometries and flow conditions approximations can be made so the N-S equation can be simplified and solved by direct integration. One important case is Stokes flow where inertial forces are small compared to viscous forces and may be ignored. Stokes flow formally requires Re $\ll 1$, however in practice Re < 1 is sufficient to neglect inertial effects[62]. Neglecting inertial terms in the N-S equations 2.8, yield the Stokes equation:

$$\nabla p = \mu \nabla^2 \mathbf{v} + \mathbf{f} \tag{2.9}$$

Equations 2.7, 2.8 and 2.9 form the basis for calculations of many microfluidic flows. Boundary conditions must be specified when solving the equations. Most commonly the flow velocity is assumed to be zero along all stationary walls, this is referred to as the no-slip boundary condition.

2.4.4 Flow in Cylindrical Microchannels

Hagen–Poiseuille flow in a uniform pipe with circular cross-section may be derived directly from the Navier-Stokes equations. For laminar flow without acceleration through a long (relative to pipe diameter) pipe an analytical solution of equation 2.8 gives the velocity profile of the fluid flow v_z in the axial direction of the pipe[61]

$$v_z(r) = \frac{R^2}{4\mu} \left(-\frac{\Delta P}{L} \right) \left[1 - \left(\frac{r}{R} \right)^2 \right] \tag{2.10}$$

with pressure difference ΔP between pipe ends separated by a distance L. The pipe has a radius R and radial distance from the center of the pipe is denoted r. Fluid flows in a parabolic profile with maximum velocity in the center of the pipe $(r = 0)$ and zero flow

velocity at the pipe walls ($r = R$). Mean flow velocity $\langle v_z \rangle$ is found by integration over the cross sectional area of the pipe

$$\langle v_z \rangle = \frac{1}{\pi R^2} \int_{\text{area}} v_z dA = \frac{R^2}{8\mu} \left(-\frac{\Delta P}{L} \right) \tag{2.11}$$

Equation 2.10 may then be rewritten

$$v_z(r) = 2\langle v_z \rangle \left[1 - \left(\frac{r}{R} \right)^2 \right] \tag{2.12}$$

which shows that maximum flow velocity $v_{\text{max}} = 2\langle v_z \rangle$ in the center of the pipe. The total flow rate in the pipe is found from the mean flow velocity $\langle v_z \rangle$ and pipe cross sectional area

$$Q = \langle v_z \rangle \pi R^2 = \frac{\pi R^4}{8\mu L} \mid \Delta P \mid \tag{2.13}$$

2.4.5 Flow in Rectangular Microchannels

Laminar flow in square channels is if interest because common microfabrication techniques yield rectangular microchannels. In the limiting case where the channel in Figure 2.7a is much wider than the height $h \ll w$. A pressure driven flow where a pressure drop Δp acts over a length l results in a parabolic velocity profile:

$$v_z(y) = \frac{\Delta p}{2\mu L} \left(\left(\frac{h}{2} \right)^2 - y^2 \right) \tag{2.14}$$

Flow velocity is zeros along the walls at $y = \pm h/2$ in accordance with the no-slip boundary condition. Volumetric flow rate Q in the channel is found by integration across the channel height:

$$Q = w \int_{-h/2}^{h/2} v_z(y) dy = \frac{w h^3 \Delta p}{12\mu L} \tag{2.15}$$

and average velocity by dividing with channel cross section:

$$U = \frac{h^2 \Delta p}{12\mu L} \tag{2.16}$$

In the general case, the axial velocity in the cross-sectional (x, y) plane as well as volumetric flow rate is known analytically in terms of Fourier series [62, p. 26]. Figure 2.7b shows flow velocity along the center plane $y = 0$ (across the channel when observed from above). For geometries where $w/h > 2$ the flow profile is increasingly flat. Due to the no-slip boundary conditions, the flow profile is parabolic in a region of width $\sim h$ For $h/w < 0.7$ the flow rate may be approximated [62]:

$$Q = Q_0 \left(1 - \frac{6(2^5)}{\pi^5} \frac{h}{w} \right) \tag{2.17}$$

where Q_0 is the flow rate for the limiting case $h \ll w$ in equation 2.15. Flow in a rectangular channel may be regarded as parabolic across the shortest dimension (typically height in microfluidic channels). For wide channels, flow rate is uniform across the width except for regions of width $\sim h$ where the velocity approaches zero to satisfy the no-slip conditions.

2.4.6 Hydraulic Circuit Analysis

Hydraulic circuits show many similarities to electric circuits and many be analyzed in an analogous way. In the case of $Re \ll 1$ and $w, h \ll L$ equation 2.15 may be rewritten:

$$\Delta p = R_H Q \quad \text{where} \quad R_H = \frac{12\mu L}{wh^3} \tag{2.18}$$

which is analogous for Ohm's law for circuits ($\Delta V = RI$). R_H is the hydraulic resistance, which is highly dependent on channel geometry ($\mathrm{O}\left(h^3\right)$). A similar relation is found for cylindrical flow in equation 2.13. A list of fluid-mechanical analogs for electrical circuit elements are found in reference [62]. As a result, circuit analysis may de used for analyzing hydraulic flow. An analog to electrical capacitance is hydraulic compliance. Fluid volume in a channel section may change as a function of pressure due to compression of bubbles or deformation of the wall (microfluidic channels are commonly made in PDMS, an elastomer). The resulting expression for capacitance in a section of channel is:

$$Q_C = C_h \frac{d(\Delta p)}{dt} \tag{2.19}$$

where $Q_c = Q_{\text{inlet}} - Q_{\text{outlet}}$ is the capacitic flow and C_h is the hydraulic equivalent to C.

2.4.7 Microfluidic Mixing and Coflow

Two flows brought in contact in a microfluidic Y-shaped channel in Figure 2.8 will flow in a laminar fashion for low Re numbers. Transport of chemical species across the flows is limited to diffusion, which is governed by the diffusion equation:

$$\frac{\partial c}{\partial t} = D \frac{\partial^2 c}{\partial x^2} \tag{2.20}$$

Where c is the concentration of chemical species and D is the diffusivity of the chemical. Ionic species in aqueous have $D \approx 10^{-9} \mathrm{m}^2\,\mathrm{s}^{-1}$ and polymers/oligomers are in the range $10^{-11} \mathrm{m}^2\,\mathrm{s}^{-1} - 10^{-14} \mathrm{m}^2\,\mathrm{s}^{-1}$, depending on molecular weight. In the case if microfluidic coflow in a straight rectangular channel, the system can be modeled by a infinite 1D domain across the channel width with initial conditions $c = c_\infty$ for $x < 0$ (left channel), and $c = 0$ for $x \geq 0$ (right channel). The solutions is

$$c = \frac{1}{2} c_\infty \mathrm{erfc}\left(\frac{x}{2\sqrt{Dt}}\right) \tag{2.21}$$

An illustration of this solution is in Figure 2.8. As the two flows downstream, solutes from the high concentration flow diffuse into the low concentration steam. The diffusive mixing continues until both flows have the steady-state concentration $c_\infty/2$. The degree of mixing

can be controlled by mean flow rate and channel length. The distance $l = \sqrt{Dt}$ is the diffusion length scale, where concentrations is approximately half of end concentration. The diffusion length scale denotes the characteristic length over which diffusion has occured at a time t. For a reservoir of given reservoir size R, the time required for diffusive mixing is in the order of

$$t_{\text{diff}} = \frac{R^2}{D} \tag{2.22}$$

In order to achieve mixing in a channel, the diffuion time t_{diff} must be in the order of the flow residence time $t_{\text{residence}} = L/U$ for flow in channel of length L. For two miscible streams of fluid through a channel of width W at a characteristic velocity U, the characteristic width W at which mixing occurs is:

$$L = PeW \quad \text{where} \quad Pe = \frac{UW}{D} \tag{2.23}$$

An channel length of $\sim L$is required for significant mixing to occur. Low Pe numbers and channel width allows mixing to take place in shorter channel lengths.

2.4.8 Laminar Flow Patterning

In the high-PE, low-Re regime commonly found in microfluidic systems, laminar patterning can be used to control spatial position and thickness of flows. As multiple channels join into one, flow rates can be used to control the co-flow. A great versatility of microfluidics comes from the fact that both geometry and flow rates change the resulting flow. One geometry gives a range of possible thicknesses. For the example channel seen in Figure 2.9, a central flow Q_2 is squeezed by a flow Q_1. Far downstream from the junction, the height-average flow is uniform across the width of the channel. In this case, the conservation of flow gives a relative width of the central channel $Q_2/(Q_1 + Q2)$. A narrow central flow can be achieved with dimensions much smaller than channel geometries by using appropriate flow rates. The distribution of chemical species in microfluidic channels can be controlled with control of channels depths, channel width or input pressures.
For flow in a cylindrical geometry in glass capillary devices in Figure 1.2a, the core flow radius R_s depends on flow rates according the the relation [66]

$$R_s = R\left[1 - \left(\frac{Q_{\text{sheath}}}{Q_{\text{sample}} + Q_{\text{sheath}}}\right)^{1/2}\right]^{1/2} \tag{2.24}$$

Q_{sample} is the flow rate in the pulled capillary, Q_{sheath} is the flow rate of the surrounding flow and outlet pipe radius is R.

Microchannels fabricated by photolithography are most suitable for 2D designs, resulting in rectangular channels with constant height. Highly viscous and miscible two-fluid flows can be used to form elaborate 3D fluid configurations in simple rectangular channels by utilizing self-lubrication phenomena. Cubaud et al. [67] have shown that coaxial flow may be generated in square micro channels where a high viscosity flow is surrounded by a lower viscosity flow in a flow focusing junction. The lower viscosity component

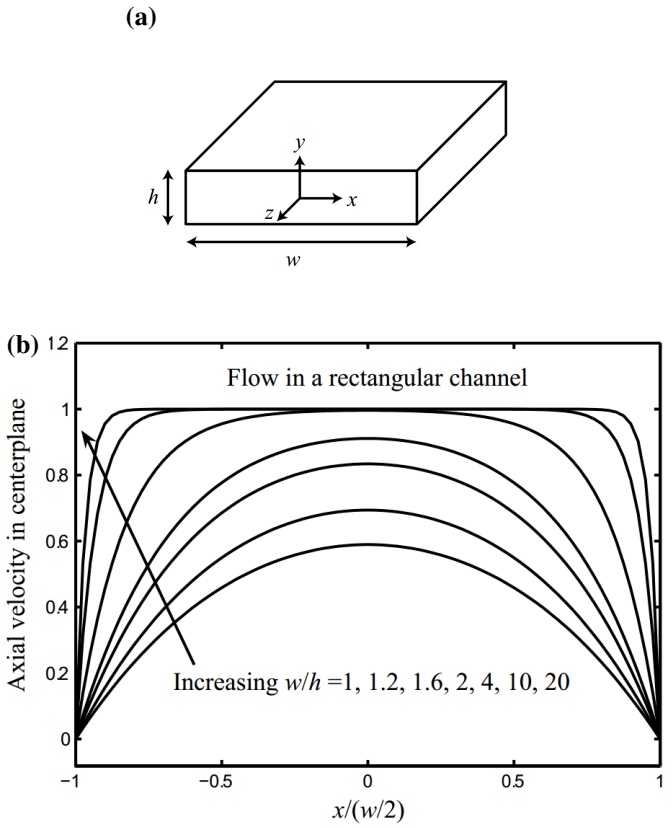

Figure 2.7: Flow profiles in square microchannel. **(a)** Geometry of square channel discussed in this section. The axes are centered in the center of the channel. **(b)** Axial flow velocity in the centerplane $(y = 0)$. Each line corresponds to a ration of channel width to height. Flow velocity is parabolic for square channels $(w/h = 1)$ and approaches constant in the center of the channel for wide channels $(w/h < 4)$. Flow velocity approaches zero towards the walls due to the no-slip condition. Adapted from referance [62]

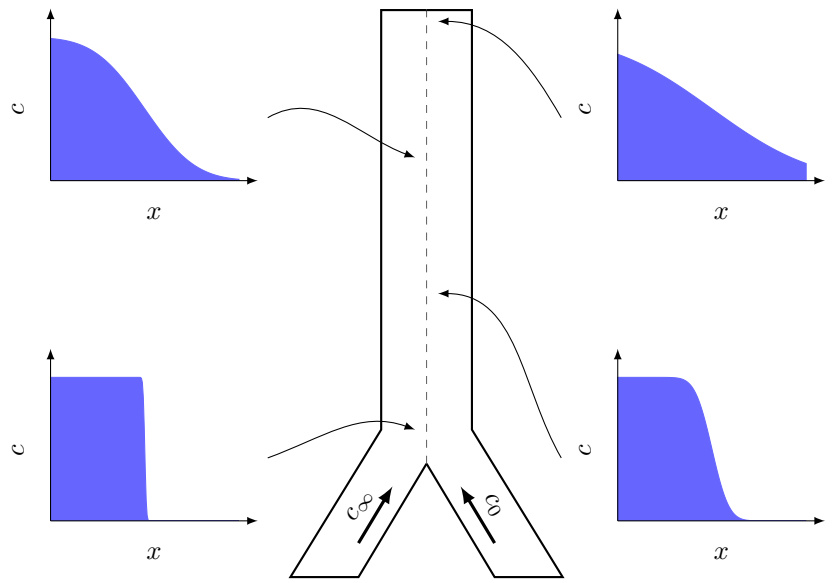

Figure 2.8: Diffusive mixing in microchannels occurs when solutions of different concentrations are flown in the same channel. Concentration gradients decrease downstream of the junction as mixing time increases. Solute distribution approaches constant across the channel width for sufficiently long channels.

tends to migrate into regions having higher shear stresses near the walls, whereas the higher-viscosity components migrates into the center of the channel where shear stresses are lower. Flow configurations are dependent on initial conditions like injection scheme, geometry and flow rates. Figure 2.10 illustrates the case of a flow focusing junction in a square channel where a higher viscosity fluid V is injected in the central channel and a less viscous fluid F is introduced in the side-channels. A single viscous thread of the fluid V is formed lubricated by the less viscous fluid F.

2.5 Scanning Electron Microscopy

The scanning electron microscope (SEM) shown in Figure 2.11 uses an electron beam to characterize the of surface morphology and compositions of a sample[68]. Electrons from a source are accelerated and focused into a small diameter probe that is raster scanned across the sample surface. Signals produced by the interaction between surface atoms in the sample and the electron probe are collected by detectors inside the microscope chamber. Only a small portion of the sample is illuminated at any time, the field of view is divided into picture elements (pixels) and the probe remains stationary at each pixel for a certain dwell time before jumping to the next one. An image representation of the sample can be assembled pixel-by-pixel where brightness corresponds to signal intensity. Microscopy is performed in vacuum to reduce scattering of electrons by gas molecules inside the instrument.

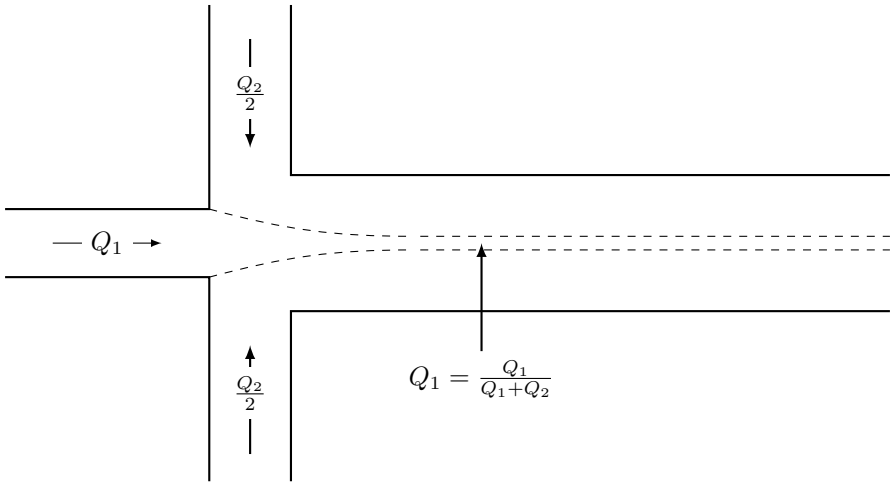

Figure 2.9: Laminar flow patterning allows flow widths to be manipulated by changing flow rates of the streams. A transition zone occurs in the junction before flow of stable width is achieved.

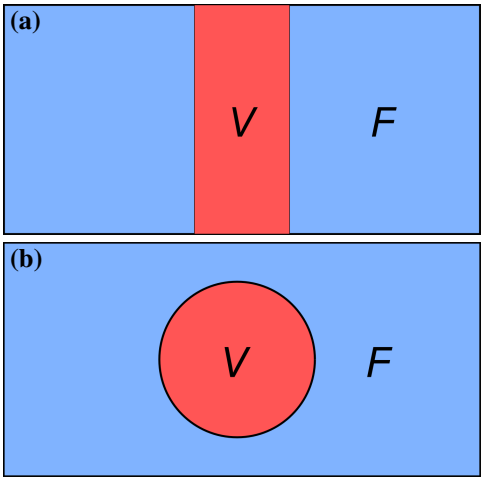

Figure 2.10: Flow lubrication for two-fluid miscible flows. **(a)** A higher viscosity fluid V is surrounded by a less viscous fluid F in a square channel junction. **(b)** A viscous thread of V is formed downstream of the junction lubricated by F.

2.5.1 Instrument Overview

Free electrons are generated in the SEM by an electron source (electron gun) via thermoionic emission, field emission, or a combination known as Schottky emission. Field emission is the preferred design in high resolution SEMs as high current density and low energy spread yields lower aberrations in electron optics[68]. The field emission gun consists of a sharp tungsten needle cathode and an extractor anode maintained at a positive potential relative to the tungsten needle. Electrons are emitted from a small area at the tip of the tungsten wire where a extremely high surface electric field in the order of $10^9\ \mathrm{V\,m^{-1}}$ allow electrons to escape through the surface potential barrier by quantum-mechanical tunneling, a process known as field emission[68]. A high surface electric field is achieved with only a few kV extractor anode bias due to the small radius of the tungsten cathode. Once free from the metal surface the electrons are accelerated to their final kinetic energy by a second set of anodes producing a electric field parallel to the optical axis. The potential difference between the tungsten needle and the accelerating anode is known as the acceleration voltage V_{acc}. The anodes have an annular design which blocks electrons with velocity vector that deviates from the optical axis. A series of magnetic lenses consisting of copper coils surrounding the optical axis are used to focus the electron beam analogously to glass lenses in an optical microscope. One important difference from optical microscopes, is that the focal length of the magnetic lenses can be manipulated by changing the lens current. As with optical systems, the magnetic lenses are prone to spherical and chromatic aberrations as well as astigmatism. Scanning coils within the final lens (or directly above, depending on the instrument design) produce an electrical field perpendicular to the optical axis that allows the probe to be deflected and scanned across the sample. A series of apertures throughout the column are used to exclude off-axis electrons and control beam brightness. The final diameter and aberrations of the electron probe largely determines the spatial resolution of the SEM, as features smaller than the probe diameter can not be resolved do to the image formation procedure. Probe diameters of 1 nm are attainable with a field emission gun-equipped SEM (FE-SEM)[69].

2.5.2 Interaction Volume

Primary electrons (PE) in the electron probe undergo elastic and inelastic scattering by atoms in the sample. The kinetic energy of the electrons is reduced by a range of inelastic scattering events until they are eventually brought to rest and absorbed into the solid. Due to multiple scatterings, the path of a single electron is highly variable, however macroscopic quantities may be determined by averaging over large populations of electrons. The penetration depth, how deep primary electrons can travel before their kinetic energy is dissipated, is given by the approximate formula[71]:

$$R = \frac{aE_0^r}{\rho} \tag{2.25}$$

where $a \approx 10\,\mu\mathrm{g\,cm^2}$, $b \approx 1.35$, ρ is the density of the specimen and E_0 is electron energy given in keV. The interaction volume shown in Figure 2.12b contains most of the scattered primary electrons, it's size is dependent on the penetration depth. Signals generated in the SEM are primarily the result of electron-sample interactions within the interaction volume.

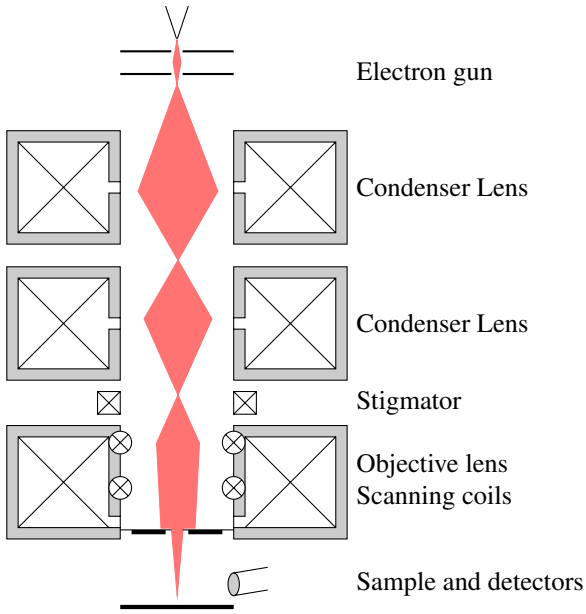

Figure 2.11: Principal components of a Scanning Electron Microscope. Electrons are generated by field emission in the electron gun and accelerated by positively biased electrodes. A series of magnetic lenses focus the electron beam into a probe that is scanned across the sample by scanning coils. Signals produced by sample-beam interactions are collected by detectors in the sample chamber. All components are enclosed in a vacuum chamber. Adapted from V. Ottesen[70], with permission.

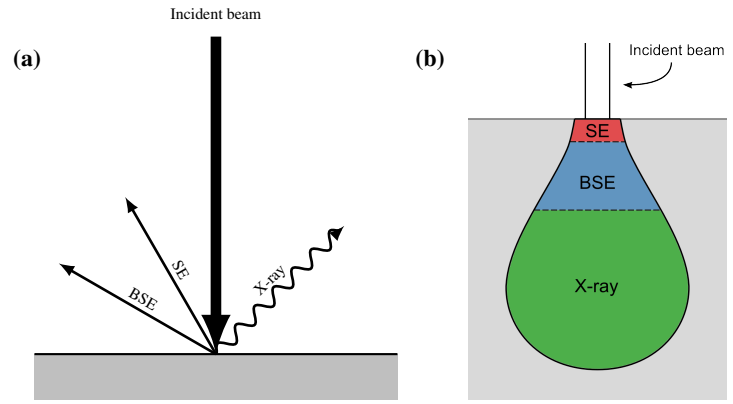

Figure 2.12: Interactions between the sample and primary electrons. **(a)** Some of the signals produced that may be used in the SEM. **(b)** The interaction volume and regions from which SEs, BSEs and X-rays may be detected. Redrawn from Goodhew et al.[69]

A smaller volume leads to a more localized signal. From equation 2.25 is clear that low electron energy and high sample density is preferable for achieving a localized signal. A wide range of signals are produced in the interaction volume, both electrons and photons of various energies are emitted from the sample. Imaging with secondary electron detectors are used to study alginate in this work and will be covered in detail.

2.5.3 Secondary Electrons

Secondary electrons allow the sample surface composition and topography to be characterized with high resolution. Energy lost in inelastic scattering of PE is transferred to valence electrons of scattering atoms. A small portion of the transferred energy is spent in ionizing the atoms producing secondary electrons (SE) inside the sample. The remaining energy exists as kinetic energy in the secondary electrons allowing them to travel inside the sample. The secondary electrons have low kinetic energies compared to PE (typically 1 - 100 eV), Only SE generated near the sample surface are able to escape into the vacuum and reach the detector. As a result, the detected SE signal originates from a small region of the interaction volume that is closest to the surface. The image generated by SE is a property of the surface structure (topography) of the sample. Contrast in SE images is dependent on composition and orientation of the sample surface. The secondary electron yield $\delta(0)$ is the average number of escaping SE per PE. Typical values are in the range 0.1 - 10 and depend on sample composition and PE energy E_0. SE yield also depends on the angle between incoming electrons and the sample surface which results in topographical contrast. Reimer[71] shows an increasing secondary electron yield $\delta(\phi)$ when the angle ϕ between the incident beam and the surface normal increases:

$$\delta(\phi) = \frac{\delta(0)}{\cos(\phi)} \tag{2.26}$$

2.5.4 Backscattered Electrons

Backscattered electrons (BSE) are PE that have been ejected from the sample by high-angle ($\approx 180°$) elastic scattering processes. Since elastic scattering involved minimal energy transfer, BSE are distinguished form SE by their kinetic energy, which is not to far below the primary-beam energy. BSE yield η is highly dependent on the atomic number yield Z as seen in Egerton[68]:

$$\eta \propto Z^2 \tag{2.27}$$

In addition, BSE are able to traverse through the sample for longer distances compared to SE due to higher kinetic energy. The collected BSE signal originates from a depth of several 100 nm, as opposed to the few nm for SE[69]. In conclusion, BSE provides a compositional contrast from the internal of the sample, while SE primarily provides mainly a topographical contrast.

2.5.5 Coating and Charging

Non-conducting samples require preparation before examination in the SEM. Electrostatic charging may occur when the sample is exposed to the electron beam and there is no direct path to ground. Charge buildup presents a problem as it deflects the PE probe, resulting in image distortions or fluctuations in image intensity. Primary electrons that are captured by the sample result in a local buildup of negative charge. At the same time SE and BSE are released by the sample which leads to positive charging. In order to maintain local charge neutrality, the combined SE and BSE yield must be one, which means that on average, one electron exits the sample per electron entering. Acceleration voltage may be chosen to reduce charging effects. High V_{acc} tends to induce negative charge as PE penetrate deep into the sample and generated SE are unable to escape. Decreasing V_{acc} increases SE yield resulting in neutral or positive charging, which is less critical. Typical values of V_{acc} for insulating samples are in the range 1kV – 10kV[68].

Coating the sample with a thin film of metal is an alternative method of eliminating charging by increasing the conductivity on the surface. Film thickness of 10-20 nm is enough to prevent charging of most specimens [68]. The film thickness usually exceeds the SE penetration depth which means that the signal originates in the film itself instead of the sample. It is therefore important the film follows the sample contours closely and any features caused by the coating layer are distinguishable from the substrate itself. In addition high aspect ratio features can be more challenging to coat.

2.5.6 Imaging of Hydrogels

Liquid containg samples such as hydrogels need to be to be dehydrated in order to be compatible with the high-vacuum conditions inside the SEM. When allowed to air dry, a liquid-air interface forms and the subsequent surface tension exerts forces compressing the drying sample. Artifacts caused by surface tension such as collapsing of porous networks are readily observed in SEM images of air-dries samples[72]. Critical point drying (CPD) eliminates the problem of surface tension. In supercritical fluids, there is no phase boundaries and surface tension between the liquid and gaseous phase, and densities are

equal[73]. Placing a specimen in a liquid that is subsequently brought to a supercritical state and removed allows drying while preserving structure.

3 Experimental

3.1 Preparation of Alginate and Calcium Solutions

Materials. High-G sodium alginate from FMC BioPolymer AS (Protanal LF 2005, LOT: S21483), *Laminaria hyperborea* stipe, $F_G = 0.68$, $F_{GG} = 0.57$, $F_{MM} = 0.21$ and $F_{GM} = 0.11$. $CaCl_2 \cdot 2\,H_2O$, $HNa_2O_4P \cdot 7\,H_2O$, $H_2NaO_4P \cdot 2\,H_2O$ and NaCl from Sigma-Aldrich. Milli-Q water.

Method. A 1.8% (w/v) solution of sodium alginate was prepared by dissolving alginate in 0.9% (w/v) NaCl solution. The solution was stirred overnight and stored at $4\,^{\circ}\mathrm{C}$ between experiments. In the case of phosphate ion containing sodium alginate solution, NaCl and $HNa_2O_4P \cdot 7\,H_2O$/$H_2NaO_4P \cdot 2\,H_2O$ (in a 61:39 ratio) was dissolved in MilliQ water. Sodium alginate solutions containing $50\,\mathrm{mM}$ – $300\,\mathrm{mM}$ phosphate ions (PI^-) were prepared. The pH was adjusted to 7.2 with $1\,\mathrm{M}$ HCl and NaOH. Calcium solution was prepared by dissolving $CaCl_2 \cdot H_2O$ and 0.9% (w/v) NaCl in Milli-Q water.

3.2 Fabrication of Glass Capillary Devices

Materials. FEMTO plasma cleaner from Diener Electronic. Sylgard®184 elastomer kit (PDMS pre-polymer and curing agent) from Dow Corning. Borosilicate glass capillaries with inner and outer diameter of 1.5 mm and 3.0 mm, respectively. Pulled borosilicate glass capillaries supplied by NTNU glass workshop. EA 3450 Epoxy glue from Loctite. Polyethylene micro medical tubing with $0.86\,\mathrm{mm}$ internal diameter and $1.32\,\mathrm{mm}$ outer diameter from Scientific Commodities Inc.

Method. The glass capillary microfluidic device was assembled as described by Jeong et al.[66]. Figure 3.1 shows the process of fabrication. A 3.5 cm long glass pipette with outer diameter of 3 mm was used to mold the center hole. Cured PDMS blocks were fixed to a 8 cm diameter Petri dish using double sided adhesive tape. Both ends of the

pipette were attached to PDMS blocks using double sided tape. A mixture of pre-polymer and curing agent in a 10:1 ratio was mixed and stirred for 5 min before being poured into the petri dish until covering the blocks and pipette. The PDMS was degassed in a vacuum desiccator for 30 min to remove bubbles, followed by curing in oven for 2 hours at $80\,^{\circ}\mathrm{C}$. The cured PDMS was removed from the petri dish and the embedded pipette was carefully extracted using 70% ethanol as a lubricant. The PDMS was cut into a 1 mm by 5 mm rectangle using a scalpel. A hole for the sheath flow was made with a $1.5\,\mathrm{mm}$ hole puncher. Glass pipettes pulled by hand with inner diameter of $50\,\mu\mathrm{m}$ - $250\,\mu\mathrm{m}$ and length of $5\,\mathrm{cm}$ were supplied from the NTNU glass workshop. The PDMS substrate and pulled glass capillary were oxygen plasma treated for 12s with 50% O_2 and $50\,\mathrm{W}$ RF generator power in the plasma cleaner. Using 70% ethanol as a lubricant, the pulled glass capillary was inserted into the center hole and permanently bonded by curing for 4 h at $80\,^{\circ}\mathrm{C}$. At the opposite side of the entrance hole, a straight glass capillary was inserted and bonded in the same way. Microfluidic tubing for sample flow was inserted into the pulled pipette and glued in place using epoxy glue. Tubing for the sheath flow was glued to a a blunt end syringe tip and attached into the sheath flow hole.

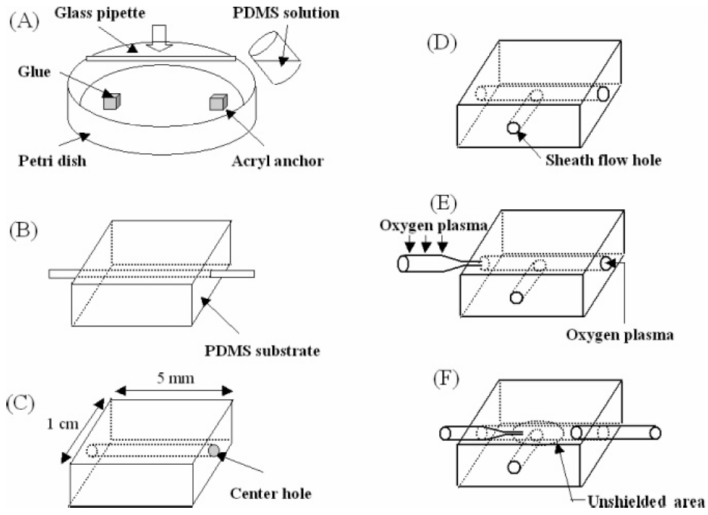

Figure 3.1: Schematic of glass capillary device fabrication[66]. **(A)** PDMS anchors are fixed to a petri dish, a glass capillary is bonded to the anchors using adhesive tape. A mix of PDMS pre-polymer and curing agent is added and cured **(B)** The cured PDMS is removed from the petri dish and excess material is cut away. **(C)** The glass capillary is extracted leaving a cylindrical channel in the PDMS **(D)** Hole for sheath flow is made using a hole puncher. **(E)** Oxygen plasma treatment and bonding of pulled glass capillary. **(F)** Oxygen plasma treatment and bonding of non-pulled glass capillary for outlet channel.

3.3 Microfabrication of PDMS Devices

Materials. $320\,\mu m$ thick Si wafers from University Wafers with diameters of 2 and 4 inches. Polos Spin 150 Spin coater. MA6 Mask Aligner (SÜSS Microtech). SU-8 Series 2 and 2100 Negative Photoresist (Micro-Chem), mr-Dev 600 developer (Micro Resist technology). Polyester film photomasks with 128,000 dpi resolution from JDPhoto. AutoCAD 2015 for mask design. Sylgard®184 elastomer kit (PDMS pre-polymer and curing agent) from Dow Corning. Trichloro(1H,1H,2H,2H,perfluorooctyl)silane 97% (Sigma-Aldrich)

Method. Photomasks were designed in AutoCAD. Polyester film photomasks with 128,000 dpi resolution were supplied from JDPhoto. Silicon wafers with 2 inch and 4 inch diameters were patterned using a standard SU-8 photolithography process. A thin layer ($700\,nm$) of SU-8 2 resist was applied to improve adhesion between the Si wafer and SU-8 structures. Features of $90\,\mu m$ height were fabricated with SU-8 2100 resist. Exposure was performed with $275\,W$ from a Hg-lamp (i-line) in a MA6 aligner with polyester film masks in soft contact mode. Processing steps are described in detail in Appendix section A. The molds were treated with silane to prevent PDMS sticking. Microfluidic channels were produced using a standard replica molding process. Silanized molds were placed in plastic petri dishes and degassed PDMS plepolymer was poured over. After curing, PDMS was peeled off the molds. Inlet holes were made with a $1.5\,mm$ UniCore puncher. Closed channels were made by bonding the PDMS cast to a glass slide after plasma treatment. Inlet holes were covered with adhesive tape to prevent contamination. Processing steps for PDMS replica molding are described in detail in Appendix section B.

3.4 Quality Control of PDMS Devices

Materials. Zeiss AxioScope A1 Reflected light microscope with AxioCam ICc 3 CCD color camera. Dektak 150 Profilometer. Cressington 208 HR B Sputter Coater for SEM Sample Prep. Hitachi TM3000 Table Top SEM.

Method. Photomasks and SU-8 molds were characterized with the AxioScope A1 optical microscope in bright field mode. Feature sizes were measured from micrographs using ImageJ software.

SU-8 molds and PDMS casts were prepared for microscopy in the table top SEM using the same process. Cross sections of molds were prepared by scribing the patterned Si wafer perpendicularly to the channel directions. PDMS channels were cut with a scalpel to produce cross sections. The samples were mounted to an SEM stub using conductive carbon tape and sputter coated with $5\,nm$ Pt/Pd (80/20) to prevent charging. The sample holder was tilted to capture cross sections. All table top SEM micrographs used a V_{acc} of $5\,kV$.

Height of the SU-8 microstructures was measured using a Dektak profilometer. Line scans were performed along a $800\,\mu m$ line perpendicular to the channel direction. Average step height between substrate and features was calculated using the profilometer software.

Table top SEM micrographs of PDMS devices were captured after gelation experiments to investigate buildup of alginate and minerals inside the device channels. The

PDMS was gently peeled off the PDMS coated glass slide by hand. The PDMS was left to dry at room temperature for at least $24\,\mathrm{h}$. Thin cross sections of the channel were made using a scalpel. The cross sections were mounted to a sample holder and sputter coated using the same process described earlier in this section.

3.5 Rheometry

Materials. Malvern Kinexus rotational rheometer with $2°$, 50 mm (CP2/50) conical shear plate and Passive Solvent Trap. Dextran from *Leuconostoc* spp. $M_r \sim 450,000 - 650,000$ from Sigma-Aldrich.

Method. Dextran was dissolved in Milli-Q water at room temperature and stirred overnight to create 10% (w/v) solution. The solution was further diluted to concentrations in the range 0.5% to 10% by adding Milli-Q water and stirring. Dextran solutions were stored in the fridge between experiments. Sodium alginate solutions were prepared as described in section 3.1. Rheometry was performed with share rate ramp of $10\,\mathrm{s}^{-1}$ – $1500\,\mathrm{s}^{-1}$ on a logarithmic scale, with 20 measurements per decade. Experiments were performed at $20\,°\mathrm{C}$ and measurements were repeated three times per sample. Rheometry was performed at five dextran concentrations: 0.5%, 1%, 2%, 5% and 10% as well as three alginate concentrations: 0.5%, 1% and 1.8%.

3.6 Microfluidic Setup and Operation

Materials. Olympus IX 70 inverted microscope with Olympus UPlanFl 4x/0.13NA, 10x/0.30NA and 20x/0.50NA objectives. Microscope mounted Photron SA-3 high speed camera. PhD ultra syringe pumps (Harvard Apparatus). Polyethylene micro medical tubing with $0.86\,\mathrm{mm}$ internal diameter and $1.32\,\mathrm{mm}$ outer diameter from Scientific Commodities Inc.

Method. Glass capillary devices were oriented horizontally as shown in Figure 3.2 to allow observation in optical microscopes. Outlet flow was was collected in a plastic petri dish where a hole was drilled for the outlet pipe. Microscope slides were used to support the device in a level position. Sodium alginate and $CaCl_2$ solutions were pumped with separate syringe pumps.
Glass capillary devices were mounted in a vertical position as shown in Figure 3.3 held in place by a clamp. The end of the outlet pipe was submerged in a collection bath of Milli-Q water.
Figure 3.4 shows the PDMS microfluidic device mounted in a 4 inch plastic petri dish and secured with adhesive tape. The petri dish was filled with Milli-Q for fiber collection. The three inlet flows were supplied using three separate syringe pumps and microfluidic tubing.
Operation of the devices was viewed using the Fastcam in Live View-mode. Videos were recorded with screen capture software.

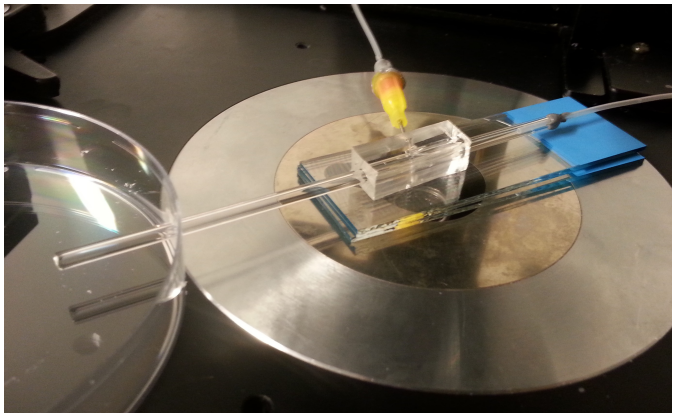

Figure 3.2: Glass capillary device in horizontal orientation allows operation to be observed using an optical microscope. Outlet flow is collected in a petri dish. Glass slides are used to support the device in a horizontal position for easier observation. The microfluidic tubes are connected to syringe pumps that are not shown.

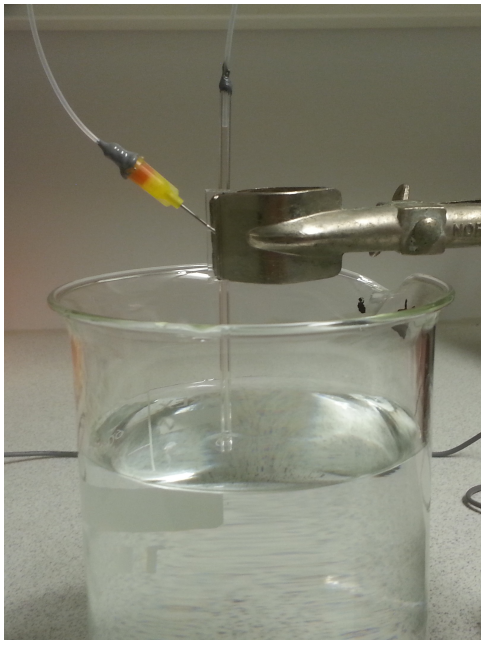

Figure 3.3: Glass capillary device in vertical orientation. Outlet flow is submerged in a collection bath. The microfluidic tubes are connected to syringe pumps that are not shown.

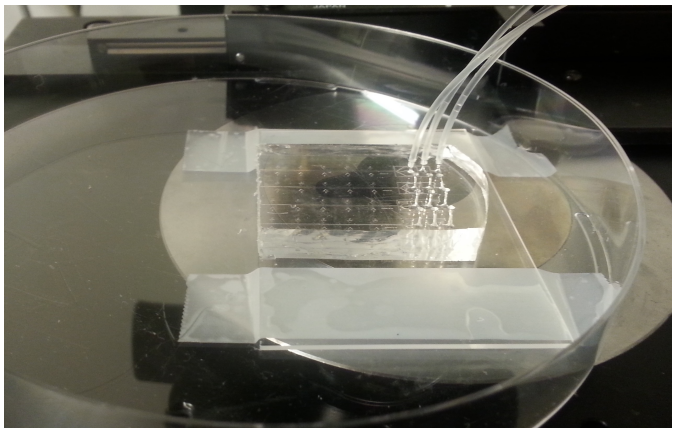

Figure 3.4: PDMS microfluidic device mounted to a plastic petri dish for collection of fibers and observation in optical microscope. The microfluidic tubes are connected to syringe pumps that are not shown.

3.7 Characterization of Alginate Fibers

Materials. Olympus IX 70 inverted microscope with Olympus UPlanFl 4x/0.13NA, 10x/0.30NA and 20x/0.50NA objectives. Microscope mounted Photron SA-3 high speed camera. Emitech K850 Critical Point Dryer. Cressington 208 HR B Sputter Coater for SEM Sample Prep. Hitachi S-5500 FE-SEM. Acetone and Ethanol (Sigma-Aldrich). Agarose, A9539 (Sigma-Aldrich). Leica V1 1000S Vibratome.

Method. Fibers fabricated in the devices were collected as specified in section 3.6 and transferred to a 96-well plate using a micropipette. The fibers were observed in a inverted optical microscope in bright field and phase contrast. Images were captured with microscope-mounted high speed camera using the accompanying software (FASTCAM Viewer). Fiber dimensions were measured from micrographs using ImageJ software.

The fibers were embedded into agarose cylinders and critical point dried (CPD) for field emission SEM (FE-SEM) characterization. Using a plastic pipette, a 3% (w/v) agarose solution was applied over the fibers in well plates. The agarose solution was prepared by dissolving agarose in cold water and stirring while heating until all was dissolved. The well plate was left at $4\,^{\circ}\mathrm{C}$ for 48 hours for the agarose to solidify. The fiber-containing agarose cylinders were extracted from the well plate and cut into $200\,\mu\mathrm{m}$ sections with a vibratome. The slices were dehydrated in ethanol using a series of increasing concentrations of 50%, 60%, 70%, 80%, 90%, 96% and 100% with 10 minutes per solution. The samples were placed in a final bath of acetone before being loaded into a critical point drier (CPD) where drying was performed according to the instrument manual. Shortly, the sample chamber was filled with acetone and pre-cooled to $5\,^{\circ}\mathrm{C}$. Acetone was exchanged with liquid CO_2 while keeping temperate at $5\,^{\circ}\mathrm{C}$. The system was then heated to a supercritical state and CO_2 was slowly vented from the chamber. The dried samples were mounted on SEM stubs using adhesive copper film. A $5\,\mathrm{nm}$ film of Pt/Pd (80/20) was sputter coated on

the samples. Samples were characterized in a Hitachi S-5500 FE-SEM using a secondary electron detector. Acceleration voltage of $2\,\mathrm{kV}$ was used in all micrographs unless stated otherwise.

4 Results

This work has focused on the development of microfluidic devices for fabrication of mineralized calcium alginate fibers. This chapter starts out by describing fabrication of glass capillary devices and microfluidic spinning of calcium alginate fibers as a continuation of the author's project work [1]. The method is extended to fabrication of mineralized alginate fibers by a counter-diffusion approach. A new device design based on results with glass capillary devices is presented. The microfabrication process of the PDMS-based device is characterized. Flow rates, fluid viscosities and design modifications are investigated to find conditions for stable flow. Using these parameters, mineralized and unmineralized fibers are fabricated and collected for characterization. Gel structure and mineral distribution is characterized with optical microscopy and field emission SEM.

4.1 Glass Capillary Devices

Fabrication strategies for alginate fibers involve coaxial flow of sodium alginate solution (NaA) surrounded by a flow of $CaCl_2$solution inside a microchannel. Gelation occurs inside the microchannel when Ca^{2+}-ions diffuse into the NaA flow and form gelled calcium alginate (CaA). The $CaCl_2$flow serves several purposes. In addition to providing Ca^{2+}-ions for gelation, it lubricates the alginate flow to prevent alginate from coming in contact with the device walls. Size of the CaA fibers can be controlled through flow focusing by modifying relative flow rates of the two flows. The two fluids are arranged into a coaxial flow by the nozzle design of the device where NaA flows through a pulled glass capillary centered inside a second, wider glass capillary. The $CaCl_2$solution flows around the pulled capillary, and the flows join along the tip of the pulled glass capillary.

Glass capillary devices were assembled as described in section 3.2. The pulled glass capillaries supplied by NTNU glassblåserverksted were fabricated by manual pipette pulling, which resulted in poor control over tip diameter. Capillaries received had internal diameters in the range $50\,\mu\mathrm{m}$ to $240\,\mu\mathrm{m}$. Devices for fiber fabrication were assembled from glass capillaries with tip diameters of $100\,\mu\mathrm{m}$ – $140\,\mu\mathrm{m}$. The pipette tips were fragile and prone to breaking during assembly, which in turn affected geometry of the tip.

Glass capillary devices were mounted in a horizontal orientation as described in section 3.6 to allow observation of flows in a optical microscope. The two flows in the glass capillary devices had to be initiated stepwise to prevent clogging. Gelation occurred rapidly whenever NaA and $CaCl_2$solutions were in contact, so stable coaxial flow had to be maintained in order to prevent buildup of alginate inside the outlet channel. In order to prevent blockage of the outlet pipe, the sheath flow of $CaCl_2$solution was initiated first. When stable sheath flow was achieved and all air bubbles were cleared from the device, the core flow of NaA was initiated. Sheath flow was kept constant at $100\,\mathrm{mL\,h^{-1}}$ while core flow rate was adjusted to achieve stable coaxial flow. Stable coaxial flow and fabrication of continuous fibers was achieved for core flows in the range $25\,\mu\mathrm{L/\,min}$ – $100\,\mu\mathrm{L/\,min}$. Fore core flow rates below $25\,\mu\mathrm{L/\,min}$ only resulted in short segments of fiber could be fabricated due to discontinuous NaA flow.

The alginate fibers formed spiral curls in the outlet pipe, as shown in Figure 4.1. The curl density increased with core flow rate. For core flow rates exceeding $100\,\mu\mathrm{L/\,min}$ the device was frequently clogged by buildup of fibers inside the device. Devices in the horizontal orientation were prone to clogging as fibers were stuck to the edge of the outlet capillary and the device was filled with gelled alginate as shown in the time lapse in figure 4.2. Shortening the outlet capillary from $5\,\mathrm{cm}$ to $2.5\,\mathrm{cm}$ increased stability of the device, but clogging could not be eliminated completely in the horizontal orientation. Fibers fabricated were sufficiently gelled in the shortened outlet capillary to be handled with tweezers without breaking.

Mounting the device in a vertical orientation with the outlet submerged in DI water as shown in section 3.6 eliminated clogging caused by fibers sticking to the end of the outlet capillary. Fibers fabricated over a range of NaA flow rates were collected and observed by optical microscopy in phase contrast mode as described in section 3.7. Micrographs of collected fibers in Figure 4.3 show that fibers remain in a coiled shape. Cross sections of the fibers indicate a cylindrical geometry. Fiber diameters measured from micrographs are presented in Figure 4.4, and indicate that fiber thickness is dependent on flow rates of the two coaxial flows. Mean diameter was calculated from 10 measurements along the fiber length for each flow rate. Thickness of the fibers was found to increase with relative NaA flow rate. The fibers had a smooth surface with small variations in diameter.

4.2 Mineralization in Glass Capillaries

Experiments have shown that unmineralized CaA fiber may be fabricated using glass capillary microfluidic devices. As a next step, the fabrication of mineralized CaA fibers by a counter-diffusion approach was investigated. For mineralization by the counter-diffusion approach, phosphate ions (PI^-) were added to the NaA flow. Precipitation of calcium phosphate minerals (CaP) would occur at the same time as gelation in the presence of Ca^{2+}-ions in the outlet capillary.

Identical devices, flow rates and procedures were used for mineralization experiments. Sodium alginate solution containing $50\,\mathrm{mM}$ – $200\,\mathrm{mM}$ PI^-were used in attempts of producing mineralized alginate fibers. All solutions were prone to rapid buildup of alginate gel inside the device and subsequent clogging. Clogging resulted in the buildup of white mass that is likely CaA gel containing CaP minerals inside the pulled capillary and outlet

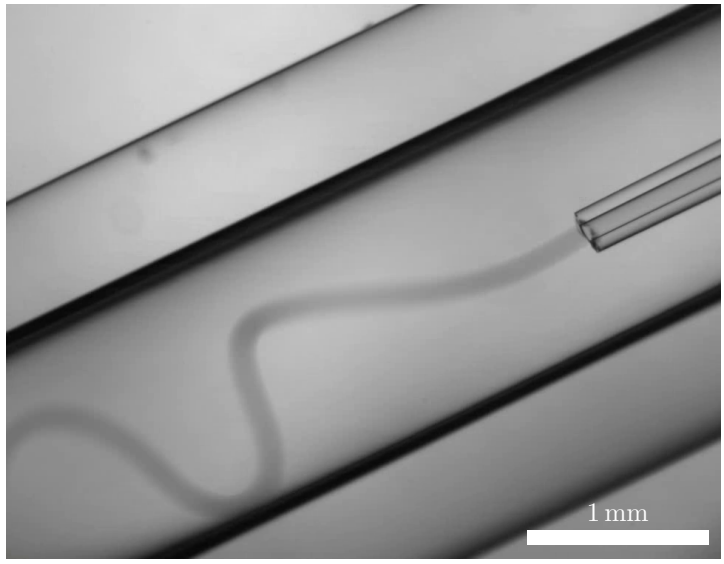

Figure 4.1: Optical micrograph of gelation in glass capillary microfluidic device. The sodium alginate solution flowing out from the pulled glass capillary is surrounded by a sheath flow of $CaCl_2$. Gelation occurs immediately downstream of the pulled pipette and the gelled fiber forms curls as it flows in the outlet capillary. Red dye (Allura Red AC) has been added to the NaA flow for visualizing the fibers in bright field. Core flow rate is $25\,\mu L/\,min$. Adapted from the author's project thesis[1].

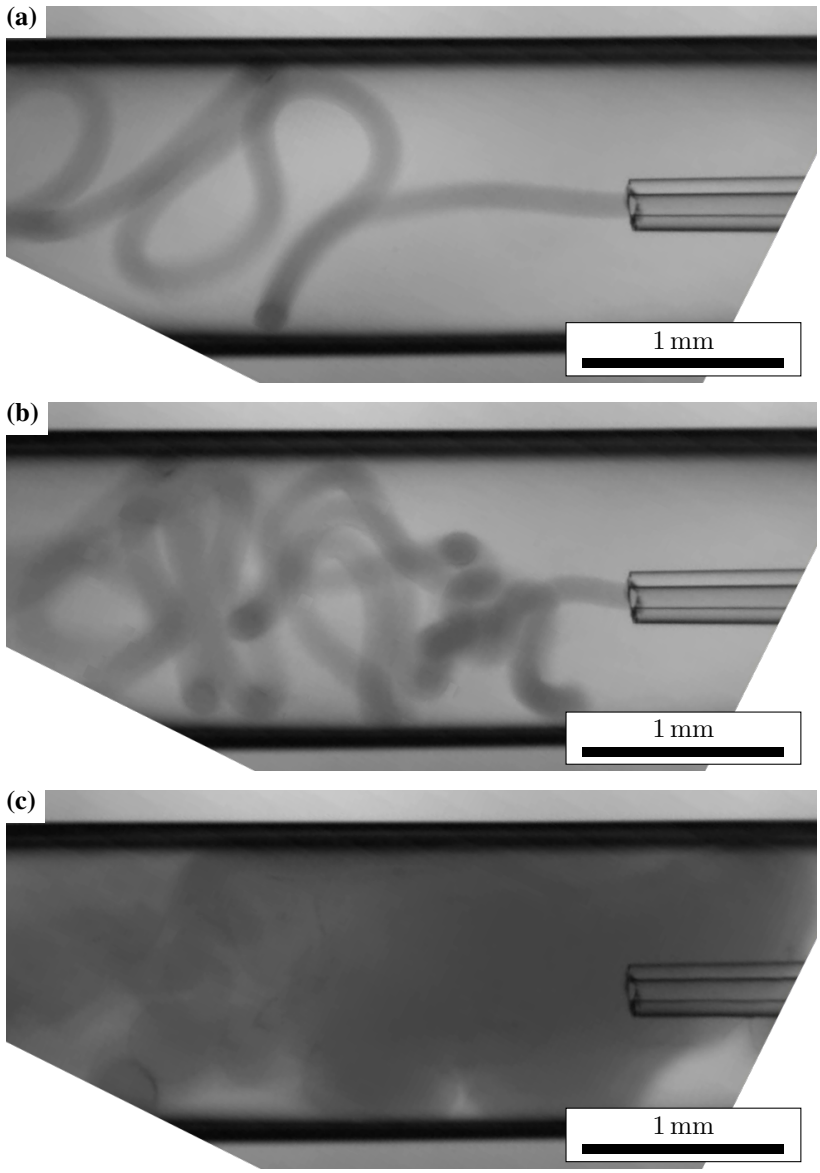

Figure 4.2: Time series of clogging caused by fibers sticking to the device outlet. **(a)** The alginate fibers stick to the end of the outlet channel (downstream, not shown) and fibers build up inside the outlet channel. **(b)** Fibers fill up the outlet capillary. **(c)** Coaxial flow is disrupted and the section of the outlet pipette close to the pulled pipette is filled with CaA and clogged. Flow direction is right to left in all figures.

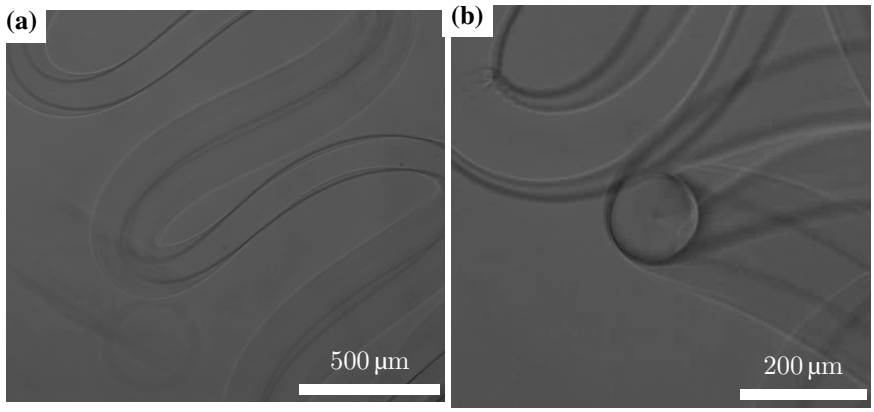

Figure 4.3: Phase contrast optical micrographs of gelled alginate fibers fabricated with glass capillary microfluidic devices that have been collected in a DI water bath. **(a)** Fibers retain curled structure in the collection bath. Curls are formed during flow in the outlet capillary. $25\,\mu\mathrm{L}/\,\mathrm{min}$ core flow rate. **(b)** A fiber is oriented perpendicularly to the focal plane, revealing the circular cross section. Core flow rate for this fiber in this figure is $50\,\mu\mathrm{L}/\,\mathrm{min}$

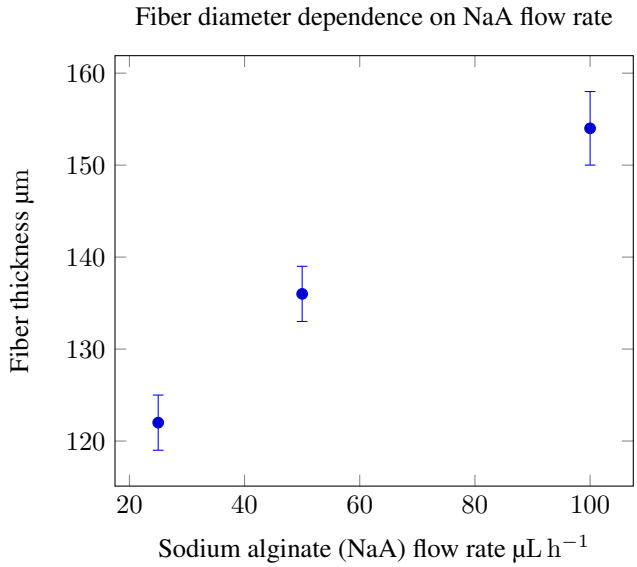

Figure 4.4: Fiber thickness for different NaA flow rates. Fiber thickness was measured from optical micrographs at 10 positions along the fiber. Error bars correspond to one standard deviation of the mean. Sheath flow rate was kept constant at $100\,\mathrm{mL\,h^{-1}}$ for all experiments.

channel. Attempts in unclogging the devices by flushing DI water were not successful.

Two distinct types of clogging were observed. The first one was buildup of mineralized CaA inside the pulled glass capillary and device failure before coaxial flow was achieved. Reverse flow of $CaCl_2$into the pulled glass capillary was observed during initiation of the sheath flow. The presence of Ca^{2+}-ions led to formation of mineralized CaA inside the pulled glass capillary when NaA flow was initiated. The second type of clogging occurred after a short period of stable coaxial flow and resulted in the buildup of mineralized CaA in the outlet capillary. Approximately $50\,\mathrm{cm}$ of fiber could be collected for $200\,\mathrm{mM}$ PI^-concentration before clogging occurred in vertically oriented devices. Clogging occurred slower in NaA solution with lower PI^-concentration. Collected fibers as well as gel forming inside the device had a white appearance by eye, indicating the presence of calcium phosphate minerals. Time series of the clogging in Figure 4.5 show the accumulation of mineralized CaA at the tip of the pulled pipette. Accumulation began along the surface at the tip of the pulled capillary, where the NaA and $CaCl_2$flow joined. Growth continued along the NaA/$CaCl_2$interface until the accumulated gel blocked the outlet capillary. The dark appearance of the gel in bright field micrographs indicates the presence of minerals. Accumulation and clogging was accelerated by disturbances in the flow such as bubbles and particles.

Stable fabrication of mineralized fibers by a counter-diffusion approach in glass capillary devices was not achieved due to the rapid clogging caused by accumulation of mineralized alginate inside the microchannels. Gelation took place as soon as the two flows joined along the tip of the pulled capillary. Reverse flow of $CaCl_2$into the pulled glass capillary also led to clogging upstream of the junction. In order to overcome the clogging the flows must be better separated during initiation and gelation must be delayed until the streams are no longer in contact with the capillary tip.

4.3 Mask Design for the PDMS Device

A new microfluidic device was designed to overcome the gel buildup issues encountered with glass capillary devices discussed in the previous section. The device was based on the same principle as previously where NaA and $CaCl_2$flows are brought in contact and gelation occurs inside a outlet microchannel. The rapid gelation and mineralization of NaA upon contact with $CaCl_2$was the primary cause of device failure for glass capillary devices. For the new design, a third flow of DI water between the NaA and $CaCl_2$was added to delay the onset of gelation in the outlet channel. The water flow was designed to act as a diffusion barrier where Ca^{2+}-ions have to diffuse across in order for gelation to occur. Thickness of the buffer flow would be controlled via flow rates to prevent gelation along walls of the device. The buffer would also prevent gelation upstream of the junction due to reverse flow $CaCl_2$during initation of flow. The flow of NaA would be separated from top and bottom wall of the device by the self-lubricating properties of multicomponent flows described in section 2.4.8.

The channel design is illustrated in Figure 4.6. The three inlets for NaA, buffer and $CaCl_2$are labeled Q_1, Q_2 and Q_3, respectively. Inlets designed by Armend Håti contained arrays of square pillars with $12.5\,\mu\mathrm{m}$ spacing to prevent large particles from the solutions from entering the device and disrupting flow. The three flows were joined in two successive

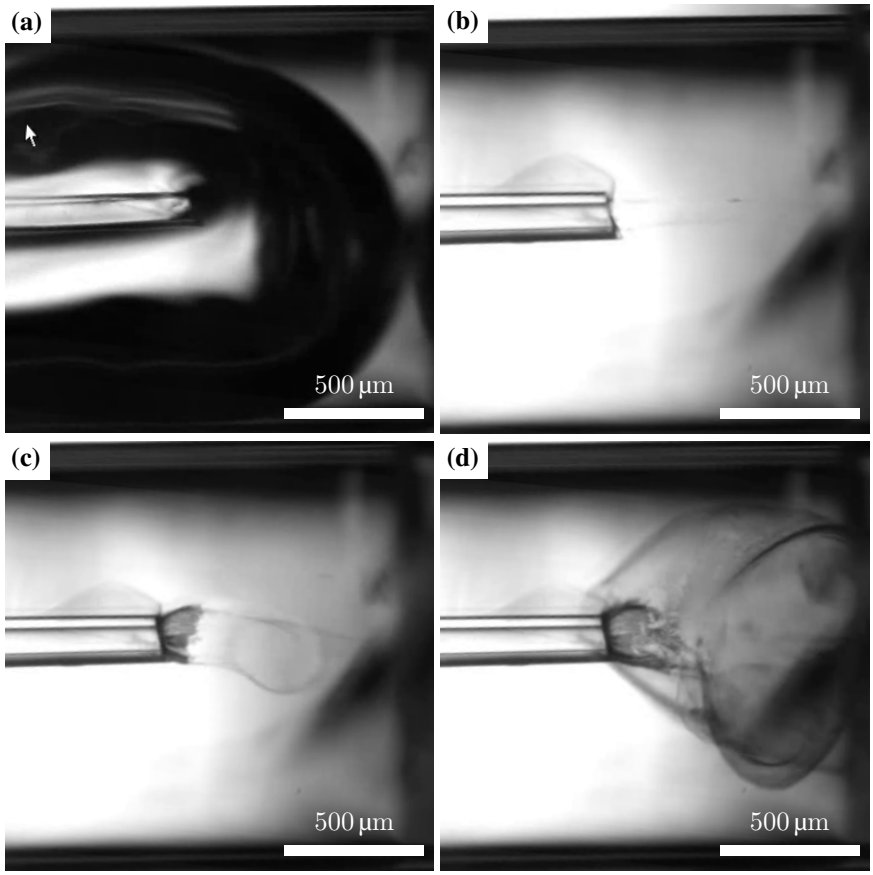

Figure 4.5: Time series of clogging in glass capillary devices caused by buildup of mineralized CaA at the pulled pipette tip. Frames are extracted from a video of the gelation process captured with a optical microscope in bright field mode as described in section 3.6. CaA is mostly transparent in bright-field mode, but alginate accumulating along device walls has a darker appearance due to the presence of minerals. **(a)** Air bubbles in the NaA flow disturb the coaxial flow. **(b)** Alginate residues form at the tip of the capillary when flow is disturbed. Minerals forming result in a darker appearance of the residues. **(c)** Mineralized CaA grows where the two streams join. **(d)** The growing CaA plug disturbs flow which results in gelation across the outlet capillary and device failure.

junctions (labeled A and B in Figure 4.6) spaced $400\,\mu\mathrm{m}$ apart. NaA (Q_1) and buffer flow (Q_2) are joined in junction A, followed by $CaCl_2$ flow (Q_3) in junction B. Gelation would occur inside a $3\,\mathrm{cm}$ long and $400\,\mu\mathrm{m}$ wide outlet channel. Triangles were places at $5\,\mathrm{mm}$ intervals along the outlet channel to help with distance measurements during flow experiments. A microscope slide was bonded to the PDMS so that the end of the outlet channel extended beyond the edge of the slide. An outlet for the gelled fibers was formed by trimming off the end of the outlet channel extending beyond the glass slide. Flow resistances (long regions of narrow channels) were added upstream of all junctions to prevent reverse flow. All channels were designed with a height of $90\,\mu\mathrm{m}$. Illustrations of all PDMS based microfluidic devices are shown in Appendix section C.

4.4 Microfabrication and Quality Control

Microchannels in PDMS elastomer were fabricated using a replica molding process. Molding would assure minimal variations in channel geometry between devices. Photolithography with SU-8 photoresist was used for mold fabrication. Each step of the device fabrication was characterized as described in section 3.4 and will be presented in this section.

Photomask: Polyester film masks were used in this project as an alternative to quartz masks due to lower cost and faster processing times. Masks were inspected in a optical microscope to check for wear and pattern deviations from the design. Figure 4.7 shows micrographs of an inlet section of the mask. Opaque regions of the mask are covered with a dark photographic emulsion while transparent regions appear bright. Small micrometer-sized black spots in the bright regions are part of the photographic film and did not have any effect on the lithography process. Wear on the masks after 5 exposures resulted in scratches seen in Figure 4.7a that were only cosmetic. The smallest features of the mask design were the square arrays in the inlet filters shown in Figure 4.7b. A rounding of the filter edges was observed in the photomasks, compared to the square features in the mask design in Figure 4.6. The rounding of corners did not have a significant on the device geometry. The smallest features on the mask, the spacing between filter squares was measured to $13 \pm 0.8\mu\mathrm{m}$ (mean $\pm$ SD) across 10 measurements. The designed spacing was $12.5\,\mu\mathrm{m}$. The designed pattern was found to be well reproduced in the polyester film masks.

Photolithography: Photolithography was performed according to the resist datasheet with $90\,\mu\mathrm{m}$ resist thickness. Spin coating of the SU-8 2100 resist for the structural features was highly prone to bubble formation. A spoon was used to apply photoresist, and bubbles were formed as resist was applied to the wafer. Due to the high viscosity of the resist, bubbles did disappear when the wafer was left to rest for several minutes. Some bubbles disappeared during soft-baking, while others remained permanently on the device. Edge beads with width of approximately $1\,\mathrm{cm}$ appeared during soft bake. Due to the size of the design, the exposed pattern overlapped with the edge bead in 2 inch wafers. As a result, edge beads could not be removed without damaging the pattern. By using 4 inch wafers for substrate, the edge bead did not overlap with the pattern and could be removed with a swab before alignment and exposure.

The wafers were characterized after resist development using optical microscopy. Figure 4.8 shows micrographs of the master where SU-8 2100 features appear bright green

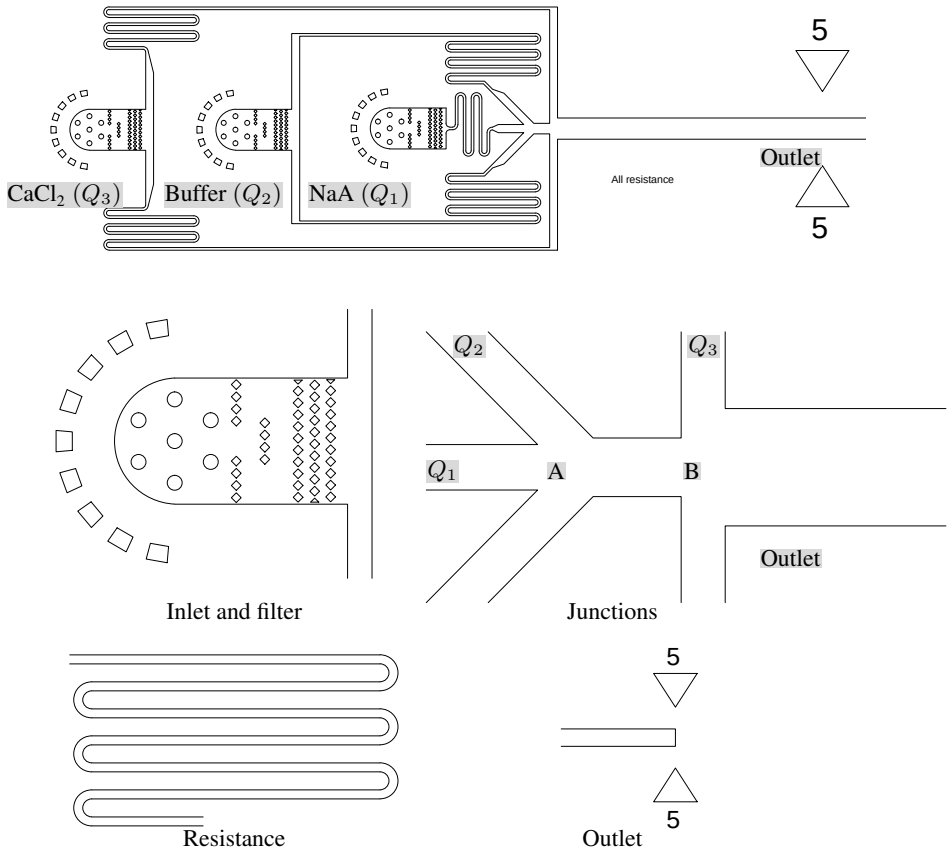

Figure 4.6: Design of the PDMS device for microfluidic fabrication of CaA fibers. The top figure shows a overview of the device with inlets for the three flows and the outlet pipe labeled. Only the first $5\,\mathrm{mm}$ of the $3\,\mathrm{cm}$ long outlet pipe are shown. The inlets contain filters consisting of arrays for square pillars. Flows are brought in contact in two junctions labeled A and B. Resistance channels are narrow curving sections located upstream of the junction to prevent reverse flow. The end of the outlet channel is designed like a closed channel. The end is trimmed off after bonding to glass, resulting in an outlet for the CaA fibers.

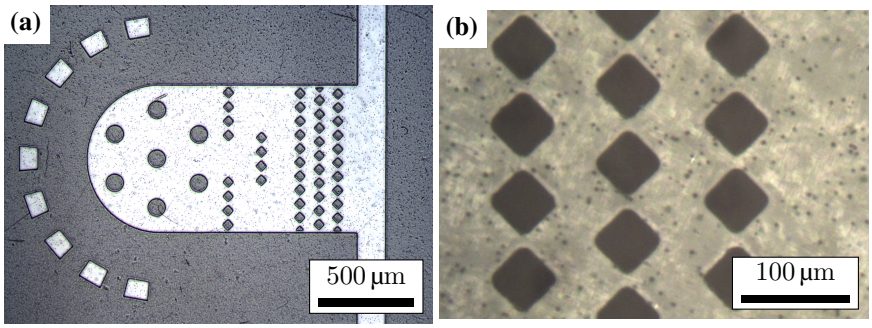

Figure 4.7: Optical micrographs of a polyester film photomask. **(a)** Large features in the pattern are reproduced without any deviations from the design. Scratches in the mask caused by wear are observed after five alignments, but do not affect the lithography process. **(b)** Square pillars that make up the filters have rounded edges. Spacing between the pillars is not significantly affected by the edge rounding.

on a purple background of Si wafer covered with adhesion layer of SU-8 2. A close-up of the filter features in Figure 4.8b reveals stress lines in the photoresist around sharp edges. Although sidewall geometry is hard to characterize in this setup, but signs of narrowing inside the filter holes can be seen by the presence of rings in the bottom of some holes. Bright regions observed along edges shown in in Figure 4.8c are likely caused by delamination of the photoresist from the wafer. Delamination typically occurred along long straight lines or sharp corners. Delamination did not have a large effect on durability of the structures as molds were reused more than 10 times without any features releasing from the Si substrate. Bubbles in the photoresist resulted in deformed channels shown i Figure 4.8d where width and height of the channel was decreased. Most bubbles could be avoided by aligning the mask so that regions of resist with bubbles are unexposed and removed during development. Width of all microchannels was measured from micrographs and found to corresponded well with designed dimensions.

Even height of the channels is critical for maintaining stable flow throughout the channels. Uneven height results in resistance variations and flow acceleration. Height of the features was measured using a profilometer for quality control. The height profile measured across the channels at six points along the structures: the $CaCl_2$ inlet, the buffer inlet, between the two junctions, 5 mm downstream of the second junction, 15 mm downstream and 30 mm downstream. A line scan was performed perpendicularly to the flow direction and an average step height along the line was calculated with respect to the substrate. Feature heights at the described positions are shown in Figure 4.10a for 2 and 4 inch wafers where each sample is represented as a separate line. The 2 inch wafers show large variations in thickness along the channel length for all samples. Maximum thickness for 2 inch wafers of approximately $120\,\mu m$ was measured at the end out the outlet channel, which overlapped with the edge bead. The 4 inch wafers had a more uniform feature height of approximately $90\,\mu m$ across the whole pattern.

A tabletop SEM was used to examine sidewall profile of the structures. A cross section of a $50\,\mu m$ wide channel in Figure 4.9 shows nearly vertical sidewall profiles with a small

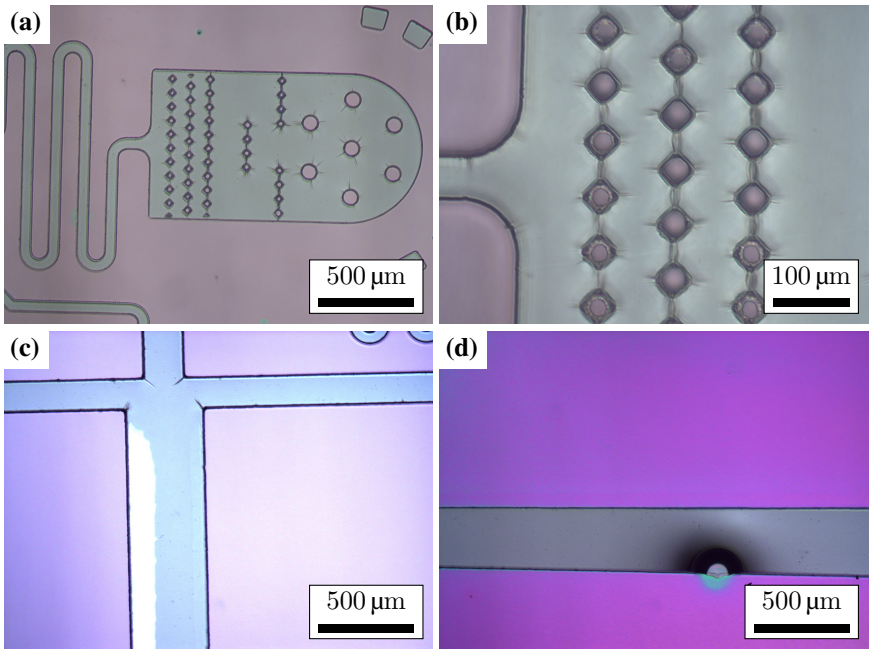

Figure 4.8: Micrographs of SU-8 mold fabricated by photolithography. SU-8 features are green, on a purple background of SU-8 2 covered Si wafer. **(a)** Large features of the $CaCl_2$ inlet are reproduced well. **(b)** Higher magnification of filters reveals stress lines and sloping walls inside the pillars. **(c)** Delamination of the resist is visible by bright features along edges. **(d)** Circular defects where the substrate has not been wetted properly by the resist.

widening at the bottom $5\,\mu m$. The top of the structures is flat, which was also observed in profilometer line scans.

PDMS cast: The PDMS cast was characterized using a table top SEM for quality control of the final geometry. A micrograph of an inlet in Figure 4.11a shows an imprint of the SU-8 features is formed in the PDMS. The protruding filters appear to be narrowing, and some are torn off at the base. A side view of the filter features in Figure 4.11b further shows the narrowing of the filter pillars. The narrowing does not affect the height of the pillars. Sidewalls in the channels are vertical as observed in micrographs of the junction in Figure 4.11c and the cross section of a $50\,\mu m$ channel in Figure 4.11d. The quality of the filter features was inconsistent across inlets in the same channel. Micrographs in Figure 4.12 are shown for the NaA inlet in (a) and the $CaCl_2$ inlet in (b). The two micrographs show a different degree of pattern rounding which indicated that photolithography quality is inconsistent across the pattern.

The fabrication process investigated in this section has been shown to reproduce microfluidic channels with width of $50\,\mu m$ and above consistently with high quality. Smaller features such as filters are prone to varying degrees of rounding and narrowing.

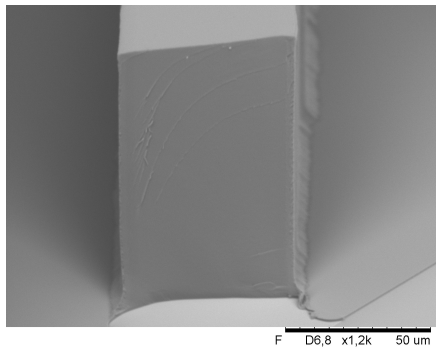

Figure 4.9: Table top SEM micrograph of a SU-8 mold. A cross section of the channels was made by scribing the Si wafer perpendicularly to the channel direction. The sample has been coated with $5\,\mathrm{nm}$ Pt/Pd (80/20) to prevent charging. Sidewalls are vertical with a widening at the bottom $5\,\mu\mathrm{m}$.

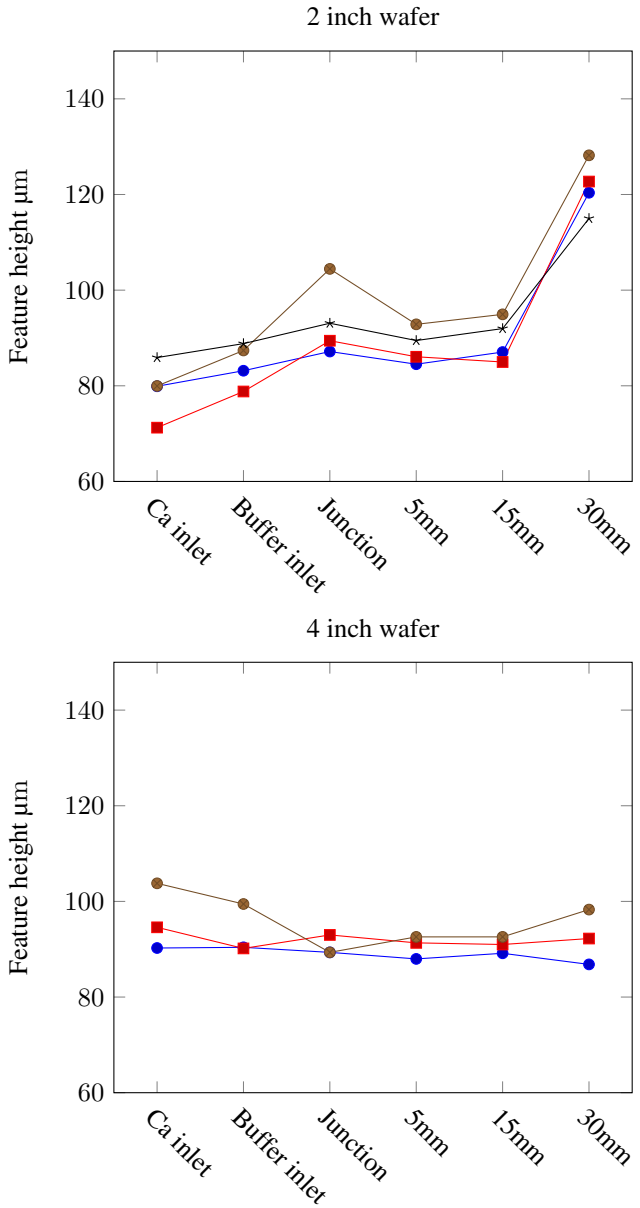

Figure 4.10: Height of the SU-8 features measured by profilometer at different positions along the structure. Position specified by the horizontal axis. Each line corresponds to a wafer and has been plotted separately to highlight variability between samples. Spacing between the points along the horizontal axis is not even and lines are drawn only for visibility. Data from 2 inch and 4 inch wafers is plotted separately.

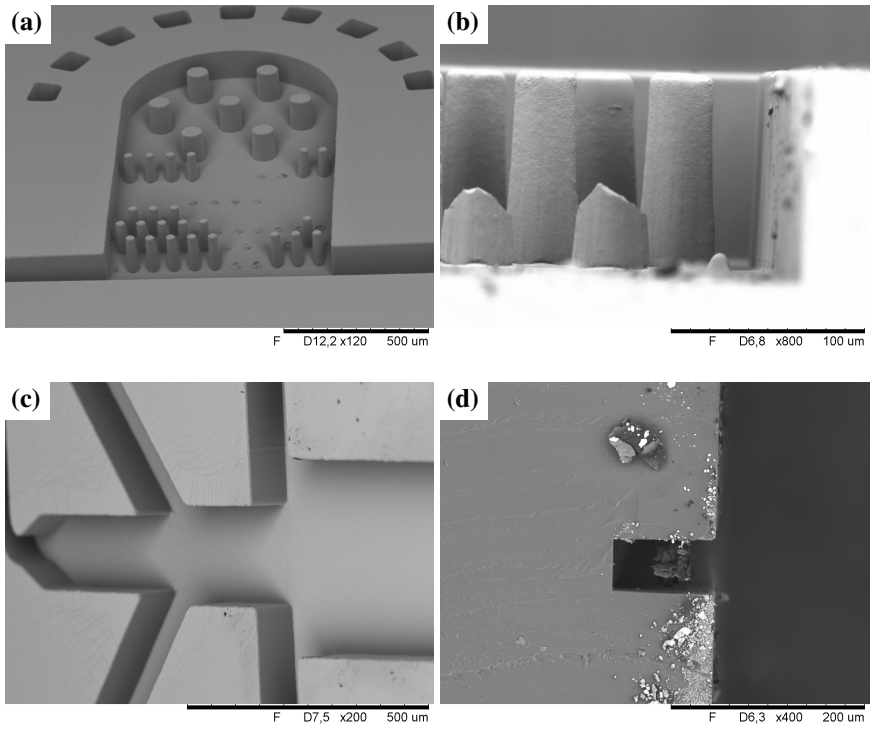

Figure 4.11: Table top SEM micrographs of devices after PDMS molding. **(a)** Overview of inlet. **(b)** Junctions and outlet channels. **(c)** Side view of filters shows narrowing. **(d)** Cross section of $50\,\mu\mathrm{m}$ channel shows vertical sidewalls.

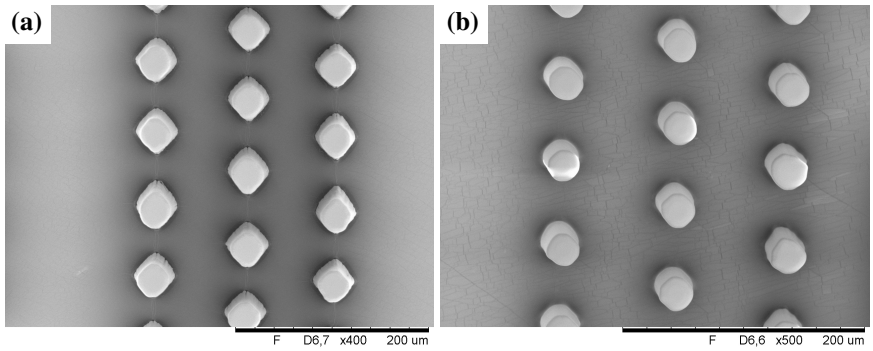

Figure 4.12: Table-top SEM micrographs of filter pillars. Square pillars that are part of the filters have varying degree of rounding between inlets. **(a)** NaA inlet shows some rounding at the top, but pillars square in the bottom. **(b)** $CaCl_2$ inlet is rounded at both top and base, indicating lower quality of photolithography process.

4.5 Flow Viscosities

Preliminary flow experiments with PDMS devices showed unstable flows and frequent reverse flow of NaA into the buffer channel which was likely caused by large difference in viscosity between the NaA flow and the buffer/$CaCl_2$ flows. Increasing viscosity of the buffer and $CaCl_2$flow would be attempted to eliminate flow instabilities due to viscosity mismatch. High molecular weight dextran would be added to the buffer/$CaCl_2$flows in order to increase flow viscosity. Dextran is a complex branched glucan which has previously been used as a thickening agent for flows in microfluidic devices[74]. The thickening properties of dextran are highly dependent on concentration.

The viscosity of NaA and dextran solutions at a range of concentrations were investigated using rheometry as described in section 3.5. Shear rates encountered in the microfluidic device depend on channel geometry and flow rates, with an estimated shear rate of $600\,\mathrm{s}^{-1}$ for typical values using equation 2.3. Viscosity was measured over a range of relevant shear rates due to the non-Newtonian nature of polymer solutions, results are shown in Figure 4.13. Alginate solutions are plotted as black while dextran are colored. Alginate shows a shear-thinning behavior while dextran is shear-thickening. Alginates have a 10-100 times higher viscosity than dextran solutions of equal concentrations for the in at the measured experimental conditions. The viscosity of 1.8% NaA solution that is used in flow experiments could not be matched with examined dextran solutions. However, the increase in viscosity compared to DI water may be sufficient to achieve stable flow.

Shear rate in the experiments was limited to $< 1500\,\mathrm{s}^{-1}$ due to slippage at the fluid/wall interface. Slippage for 1.8% NaA occured around $2000\,\mathrm{s}^{-1}$ and resulted in a sudden drop in apparent viscosity of the sample.

4.6 Determining Stable Flow Conditions

Experiments were performed to find flow rates for NaA s(Q_1), buffer (Q_2) and $CaCl_2$ (Q_3), as labeled in Figure 4.6, which resulted in stable flow in the device. Stable flow is the term used for parallel flow of all thee fluids in the outlet channel without any time-dependent fluctuations. Initial experiments had shown that unstable flows resulted in gel forming inside the microchannels, either inside the outlet channel or upstream of the junction in channels 2 and 3, resulting in clogging and irreversible damage to the device. For experiments in this section, Ca^{2+}-ions were not added to the "gelling" stream Q_3, instead Q_3 and Q_2 were the same solution (DI water or dextran solution). Clogging was therefore avoided in the case of reverse flow. The effect of four parameters (Q_1, Q_2, Q_3 and dextran concentration) was investigated using the PDMS microfluidic device described in previous sections.

In the first experiments flow rates Q_1 and Q_2 (corresponding to flows entering junction A in Figure 4.6) were modified while keeping Q_3 constant at $6\,\mathrm{mL\,h}^{-1}$. The NaA stream Q_1 was kept at 500, 1000 or 1500 $\mu\mathrm{L\,h}^{-1}$ while the buffer flow rate Q_2 was decreased stepwise from 1000 $\mu\mathrm{L\,h}^{-1}$ to 50 $\mu\mathrm{L\,h}^{-1}$. The edge between flows 1 and 2 could be visualized in the optical microscope using phase contrast mode due to the difference in refractive index between NaA and water/dextran solutions. No edge could be seen between

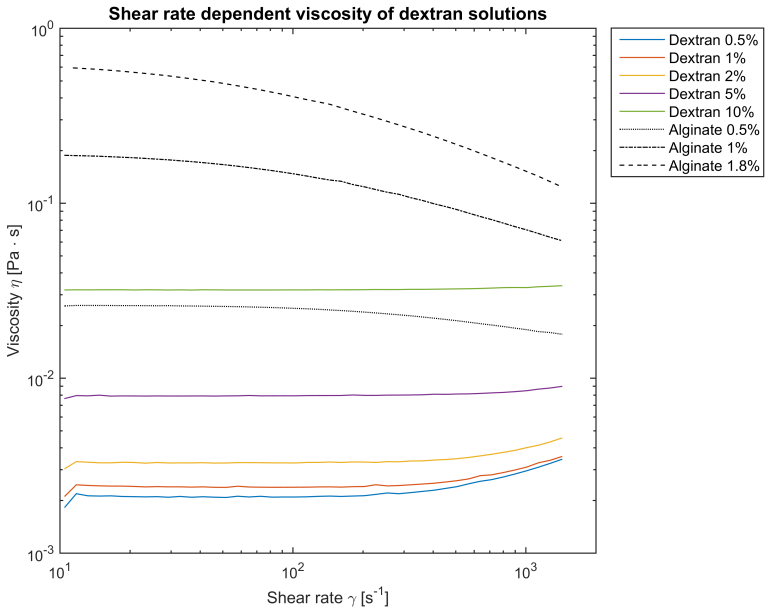

Figure 4.13: Viscosity of alginate solutions (black) and dextran solutions (colored) as measured by rheometry. Alginates exhibit a shear thinning behaviour while dextrans are shear thickening. Viscosity for both polymer solutions increases with solute concentrations. Alginate solutions are more viscous than dextran solutions with equal concentration.

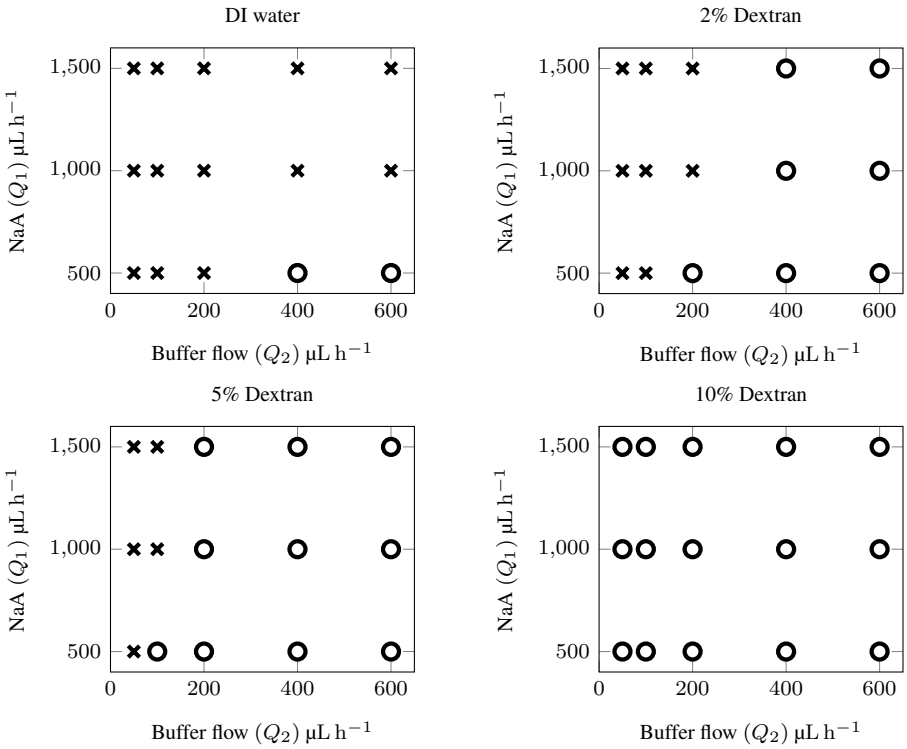

Figure 4.14: Stability of flow in the PDMS device as a function of NaA flow Q_1 and Buffer flow Q_2. Flow rate Q_3 was kept constant at $6\,\mathrm{mL\,h^{-1}}$ in all experiments. Stable coaxial flow is labeled ○, while parameters resulting in reverse flow into the buffer channels are marked with ×. Dextran concentration for flows 2 and 3 is indicated in the plot title.

flow 2 and 3.

Flow experiments were performed with DI water and dextran solutions of 2%, 5% and 10% (w/v) in flows 2 and 3. Results for each solution are shown in Figure 4.14 where ○ indicates stable coflow in the outlet channel and × indicates failure. In all cases of failure, flow 1 and 3 would flow into channel 2 when Q_2 was below a threshold flow rate. Conditions where $Q_2 > 600\mu\mathrm{L\,h^{-1}}$ have been omitted in the figures for clarity because stable flow was achieved in all cases except for $Q_1 = 1500\,\mu\mathrm{L\,h^{-1}}$ where stable coflow was not achived without the use of dextran for any flow rate Q_2.

High flow rates of buffer were needed to achieve stable flows without the use of dextran to increase viscosity. Increasing NaA flow rates, required an increase in flow rate and/or viscosity of the buffer stream to prevent reverse flow. In the case of 10% dextran in flow 2 and 3, stable flows were achived with $Q_2 = 50\,\mu\mathrm{L\,h^{-1}}$ for all investigated flow rates of NaA.

Stable flow rates for junction B were investigated using the same procedure as for junction A. Buffer flow Q_2 was kept constant while changing flow rates Q_1 and Q_3. Results presented in Figure 4.15 have the combined flow rate Q_2+Q_3 as the horizontal axis. In the

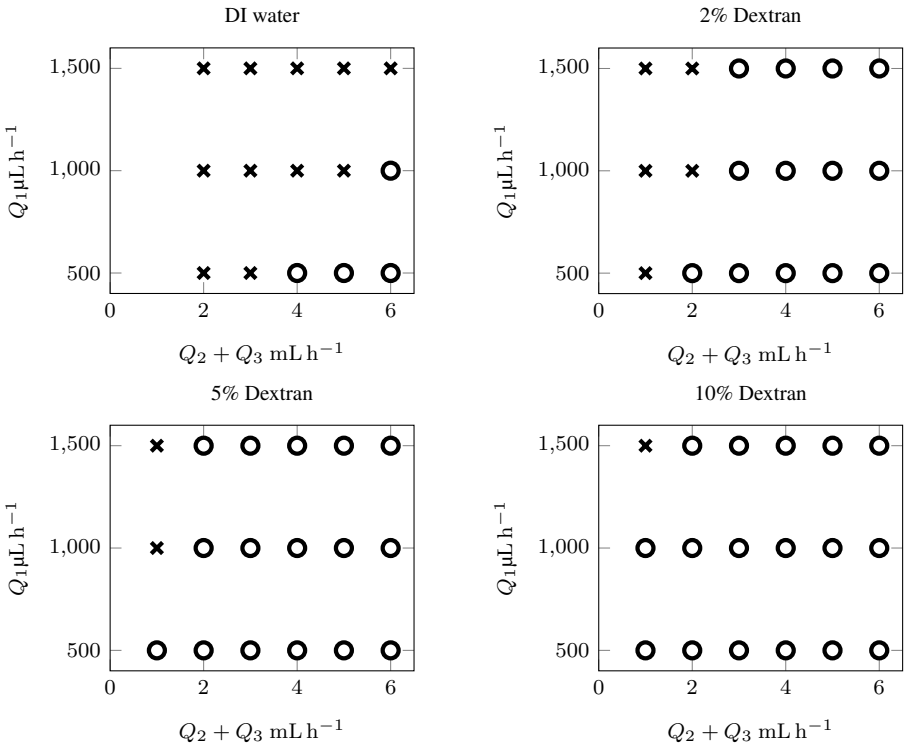

Figure 4.15: Stability of flow in the PDMS device depends on NaA flow rates Q_1 and gelation flow rates Q_3. Stable coaxial flow is labeled ○, while parameters resulting in reverse flow into the buffer channels are marked with ×. Dextran concentration for flows 2 and 3 is indicated in the plot title. Flow rate of the buffer solution Q_2 was $1000\,\mu\mathrm{L\,h^{-1}}$ for experiments with DI water and $400\,\mu\mathrm{L\,h^{-1}}$ for experiments with dextran solutions.

case where only water was flown in channel 2 and 3 shown in Figure 4.15a, Q_2 was kept constant at $1000\,\mu\mathrm{L\,h^{-1}}$. For dextran solution flows shown in Figure 4.15b, c and d, Q_2 was kept constant at $400\,\mu\mathrm{L\,h^{-1}}$. Flow rates of Q_3 below a threshold resulted in reverse flow in channel 2, the same failure as observed for flow experiments in junction A. Reverse flow in channel 3 was not experienced for any flow rates. As with junction A, increased NaA flow Q_1 required an increased Q_3 to retain stable flow. Increasing the viscosity of flows 2 and 3 increased stability for low flow rates of Q_3. Results for $Q_2+Q_3 > 6\,\mathrm{mL\,s^{-1}}$ are omitted in the plots for clarity. For these conditions, stable flow was achieved in all cases except for DI water flow and $Q_1 = 1500\,\mu\mathrm{L\,s^{-1}}$.

Flow rate experiments have shown that unstable flows result in reverse flow into channel 2. Buffer flow rates Q_2 must be higher than a threshold to sustain stable flow in the outlet channel. Increasing the viscosity of the buffer and gelling flows allows stable flow to be achieved at lower buffer flow rates. Lower buffer flow rates allow for a smaller diffusion barrier and rapid gelation of NaA in the outlet channel.

Table 4.1: Geometry variations in the tested designs. Two alternative designs were investigated to find parameters for stable flow. The effect of resistance channels and width of buffer channel was tested. All channel designs are shown in Appendix C.

Design name	Resistance channels	Buffer channel width
Original design	Channel 1, 2 and 3	$150\,\mu\mathrm{m}$
No resistance	None	$150\,\mu\mathrm{m}$
Narrow buffer	Channel 1, 2 and 3	$50\,\mu\mathrm{m}$

4.7 Channel Geometry Modifications

There are numerous possibilities for modifying the device design. Options include width, length, height and shape of all microchannels. In this section two geometry modifications are investigated in an attempt to overcome weaknesses with the first PDMS device design. An overview of designs investigated is shown in Table 4.1, and schematics of the designs are shown in appendix section C.

The first design modification involved removing all resistance channels and replacing them with straight channels. Results from microfabrication of devices in section 4.4 have shown that SU-8 features are prone to delamination around corners and edges. A simpler design would remove most of the bends that are susceptible to delamination. Decreased channel length also made it easier to avoid bubbles in the photoresist during the alignment process. Flow experiments identical to the ones described in the previous section were performed with 5% dextran solution in a device without any resistance channels. Results shown in Figure 4.16 indicate that devices without resistance channels are more prone to reverse flow for low Q_2 and Q_3.

A second design modification involved increasing flow resistance in the buffer channel buffer channel in junction A by narrowing width from $150\,\mu\mathrm{m}$ to $50\,\mu\mathrm{m}$. The design was tested at identical conditions as previous designs. Results in Figure 4.17 show increased flow stability compared to the original design in Figure 4.14c and 4.15c. Flow experiments indicated that design of the buffer channel is critical for achieving stable flow. Increasing flow resistance by adding narrow, long resistance channels upstream of the junction allows stable flow to be maintained for lower buffer flow rates. This in turn enables thinner buffer flow widths and more rapid gelation in the outlet channel. The narrow buffer channel design would be used for further experiments and fiber fabrication.

4.8 Fabrication of Unmineralized Fibers

Gelation experiments in PDMS microfluidic devices were started with the fabrication of unmineralized CaA fibers. The narrow buffer channel design characterized in the previous section, illustrated in Figure C.3, was used for fabrication of CaA fibers due to improved stability compared to the original design. Viscosity of channels 2 and 3 was increased with the addition of 10% (w/v) dextran. Flows were initiated in a specific order to prevent gelation occurring upstream of the outlet channel. Buffer flow was initiated with a high flow rate $Q_2 = 5000\,\mu\mathrm{L\,h^{-1}}$ until the whole device is filled with liquid. Gelling solution flow was started with a flow rate of $500\,\mu\mathrm{L\,h^{-1}}$, and left to run until a clear contrast between the

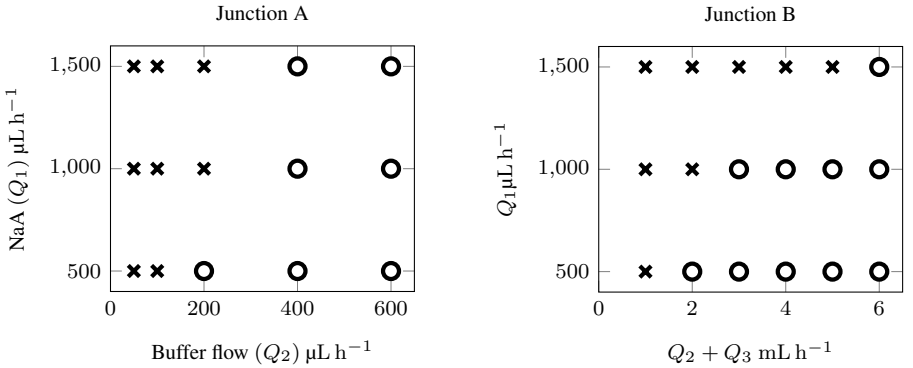

Flow rates experiments with the "No resistance" design from table 4.1. Stable coaxial flow is labeled ○, while parameters resulting in reverse flow into the buffer channels are marked with ×. Flows 2 and 3 were thickened with 5% dextran.

Figure 4.16: Flow rates experiments with the "No resistance" design

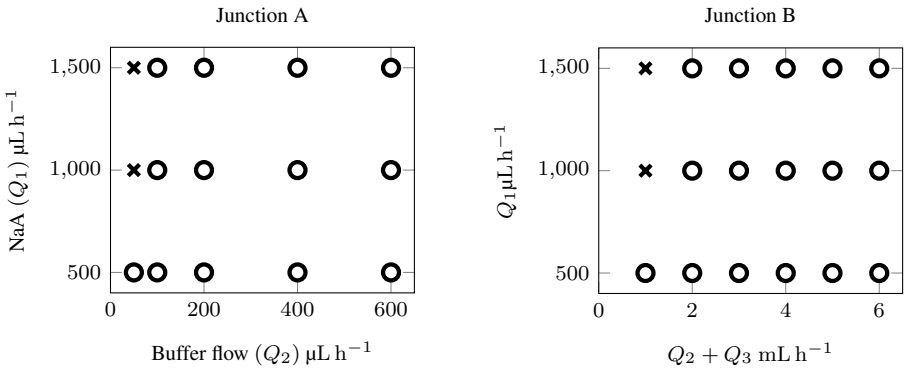

Figure 4.17: Flow rates experiments with the "Narrow buffer" design from table 4.1. Stable coaxial flow is labeled ○, while parameters resulting in reverse flow into the buffer channels are marked with ×. Flows 2 and 3 were thickened with 5% dextran.

two flows is seen in the outlet channel using phase contrast. NaA flow was then initiated with a flow rate of $Q_1 = 500\,\mathrm{mL/hour}$. The stepwise flow initiation was successful in preventing reverse flow during setup. The thick buffer stream prevented any gelation inside the device, and ungelled NaA solution was flowing out of the outlet for buffer flow rates of $5000\,\mu\mathrm{L\,h^{-1}}$. These flow rates were kept until all bubbles were cleared from all channels and the stream thickness was constant in the outlet flows (because of capacitance). Flow in the outlet channel was continuously observed with a optical microscope in phase contras mode where the boundary between the parallel flows was clearly visible.

Gelation was initiated by decreasing buffer flow rate to $Q_2 = 800\,\mu\mathrm{L\,h^{-1}}$ while simultaneously increasing gelling solution flow rate to $Q_3 = 6\,\mathrm{mL\,h^{-1}}$. Optical micrographs of the outlet channel where gelation occurred are shown in Figure 4.18. Edges between the three flows are clearly visible close to the junction. Only one edge is observed approximately $5\,\mathrm{mm}$ downstream of the junction where where Ca^{2+}-ions have diffused across the buffer stream. Gelled fibers undergo a buckling deformation as the flow velocity decreases close to the device outlet.

Fibers formed curls as they were brought to rest in the fluid-filled petri dish. Gelled fibers were collected with a plastic pasteur pipette and transferred to a micro well plate for observation in optical microscope. Unmineralized fibers were not visible in brightfield, but could be observed in phase contrast mode as seen in Figure 4.19a. The fibers had a smooth surface and even surface. Cross sections of the fibers were observed where the fiber was oriented perpendicularly to the focal plane as shown in Figure 4.19b, and revealed an elliptical shape. NaA flow rate Q_1 was increased to fabricate thicker fibers. Fiber thickness measured for different NaA flow rates show increased thickness as well as ratio between major and minor axis. Fiber dimensions measured from optical micrographs of fiber cross sections are presented in Figure 4.20.

Particles accumulated in the NaA channel during operation as shown in Figure 4.21. Accumulation typically occurred where channels narrowed or in channel bends. Large particles, likely to be undissolved alginate, could be observed bowing between or above pillars in the inlet filters. Accumulation of particles in the NaA channel lead to clogging upstream of junction A after hours of device operation.

4.9 Fabrication of Mineralized Fibers

Fabrication of mineralized fibers in glass capillary devices was not successful due to the accumulation of mineralized gel along device walls. To counter this problem, a PDMS-based device was manufactured where NaA and $CaCl_2$flows were separated by a buffer flow to delay the onset of gelling/mineralization. Results in the previous section demonstrate the successful fabrication of unmineralized fibers. Next, fabrication of mineralized fibers was investigated using the counter-diffusion approach with PI^-ions present in the NaA flow. Fabrication of mineralized fibers was performed using the same procedures and flow rates as for unmineralized fibers in the previous section.

Fibers were sufficiently gelled to be collected without breaking for all investigated NaA flow rates in the range of $500\,\mu\mathrm{L\,h^{-1}}$ – $2500\,\mu\mathrm{L\,h^{-1}}$ and PI^-concentrations in the range $100\,\mathrm{mM}$ – $300\,\mathrm{mM}$. Collected fibers had a white appearance by eye, and dark regions along the edge were observed in bright field in optical microscope as shown in Figure

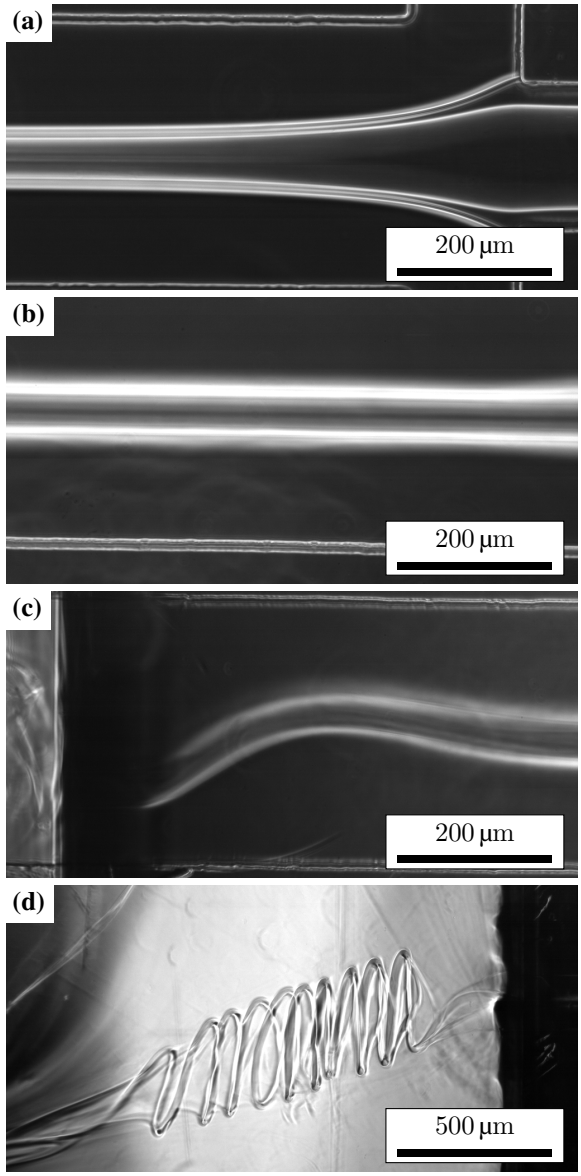

Figure 4.18: Phase contrast optical microscope images of gelation in a PDMS microfluidic device. Flow direction is from right to left in all figures. **(a)** Interfaces between the tree flows are observed close to the junction. Flow focusing results in a narrowing NaA and buffer flow. **(b)** 5 mm downstream in the outlet channel, only one interface is observed as Ca^{2+}-ions diffuse across the buffer flow. **(c)** Gelled fibers undergo a buckling deformation as the flow velocity decreases close to the device outlet. **(d)** Fibers form coils in the collection bath.

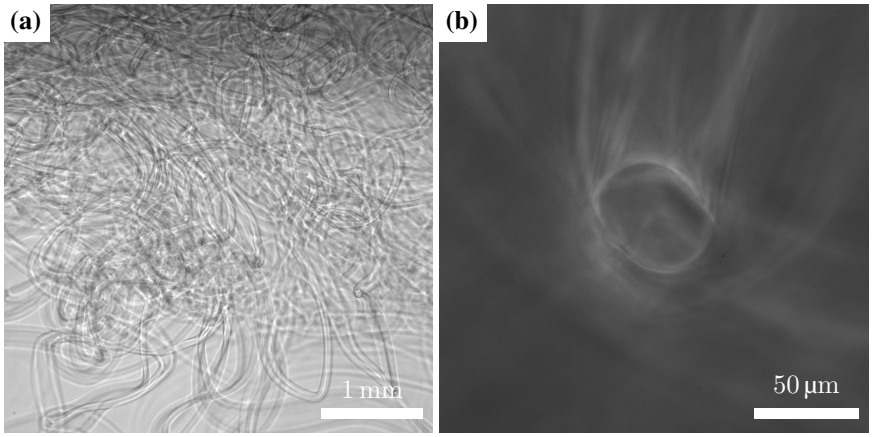

Figure 4.19: Optical micrographs of collected CaA fibers. **(a)** Collected fibers are visible in phase contrast. **(b)** Fibers have a elliptical cross section that is visualized when the fiber is oriented perpendicular to the focal plane.

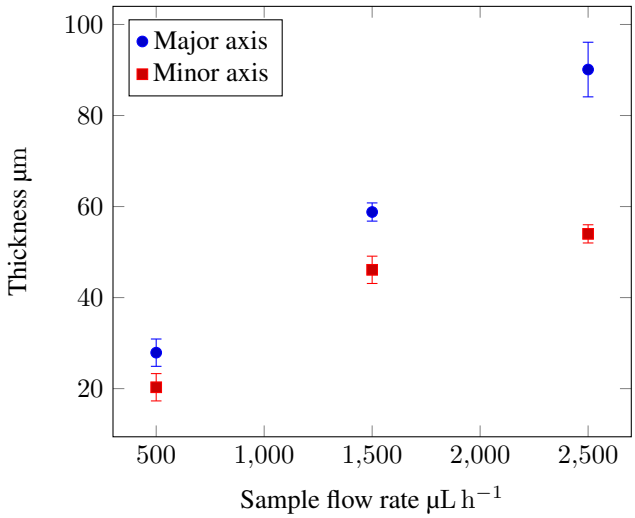

Figure 4.20: Fiber thickness for different NaA flow rates in a PDMS device. Fibers have a elliptical cross section, each color represents one of the ellipse axes. Dimensions have been measured using optical microscopy. 10 measurements were performed along the fiber length. Error bars are one standard deviation of the mean.

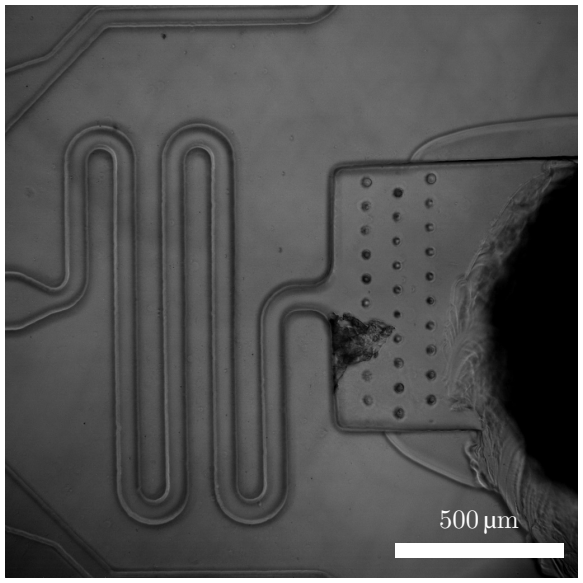

Figure 4.21: Phase contrast optical micrograph of particles accumulating in the NaA inlet, downstream of the filters

4.22, which are likely to be minerals formed along the perimeter of the fiber. Increasing phosphate concentration resulted in more visible minerals. Fibers with $300\,\mathrm{mM}$ PI^-had a less smooth surface and less homogeneous thickness compared to fibers with lower mineral content.

Stable flow and fiber fabrication was maintained for approximately 10 min with $100\,\mathrm{mM}$ PI^-, while only a few minutes were achieved for $300\,\mathrm{mM}$ PI^-. Buildup of mass along the top and bottom of the outlet channel resulted in reverse flow into the buffer channel, gelling upstream of the junction and clogging. A buildup of alginate and minerals on the PDMS surface at the top of the outlet channels shown in Figure 4.23. For buffer flow rates of $800\,\mu\mathrm{L\,h^{-1}}$ buildup occurred approximately $5\,\mathrm{mm}$ downstream of the junction and could be observed in optical microscope as a black line situated at both edges between the alginate and buffer flows. The thickness of the deposited materials widened downstream, resulting in a central mass widening downstream until reaching the end of the outlet channel. As more material was deposited, flow was disturbed which led to irregular shape and dimensions of the collected fibers. When the mass covered a large section of the outlet channel, the device broke down due to reverse flow of NaA and $CaCl_2$into the buffer channel. Flows with low PI^-concentration below $50\,\mathrm{mM}$ were not prone buildup of materials in the outlet channel. High-speed videos captured $5\,\mathrm{mm}$ downstream of the junction indicate that small particles start growing at the wall but are flushed away for low PI^-concentrations, for higher PI^-concentration they remain and grow.

Experiments with modified surface chemistry of the channels were performed in an attempt to decrease buildup. The PDMS channels become hydrophilic for a period after plasma treatment during the glass bonding stage of fabrication. By filling the channels with

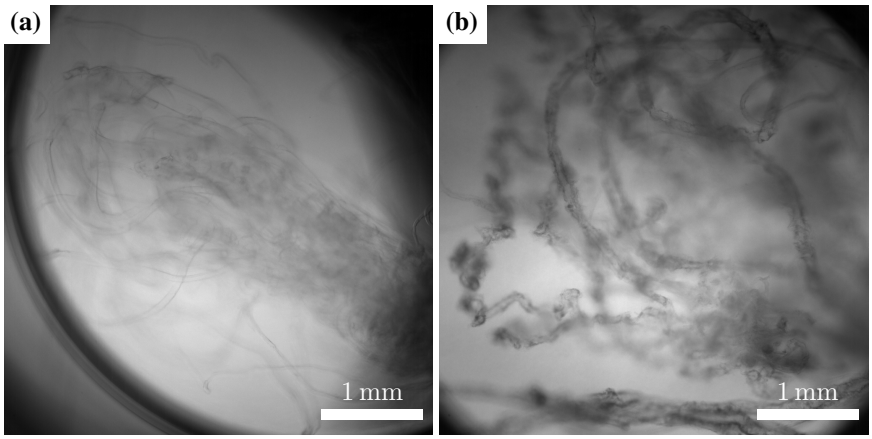

Figure 4.22: Optical micrographs of mineralized fibers in bright field. Minerals form dark regions at perimeters of the fiber in brightfield mode. Phosphate ion content in NaA flow during fabrication was: **(a)** $100\,\mathrm{mM}$ PI^- **(b)** $300\,\mathrm{mM}$ PI^-

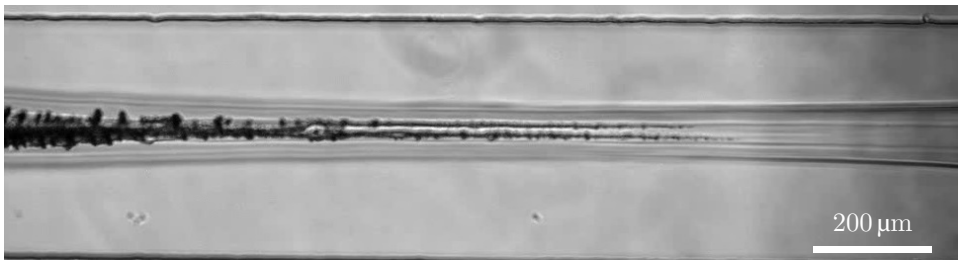

Figure 4.23: Optical micrograph of CaP and alginate buildup along top/bottom walls of the outlet channels. Dark features are caused by mineralized alginate. Flow direction is from right to left.

water shortly after bonding, the hydrophilic surface chemistry was maintained during flow experiments. In a second experiment, hydrophobic channels were made by spin coating a thin film of PDMS onto glass slides before bonding the device. Neither hydrophobic nor hydrophilic surface treatments were effective in limiting buildup of minerals/alginate and clogging.

Devices where PDMS was spun on glass could be peeled apart, separating the bottom surface from the rest of the channel and revealing the internal surface of the microchannels. This method was used to study the buildup process using a table top SEM as described in section 3.4. Flow was stopped when buildup was observed, but before clogging occured. Micrographs in Figure 4.24 show the progression of mineral/alginate buildup. Particles with sizes below $10\,\mu\mathrm{m}$ are observed during early stages of buildup. At later stages, the whole surface of the channel is covered in material.

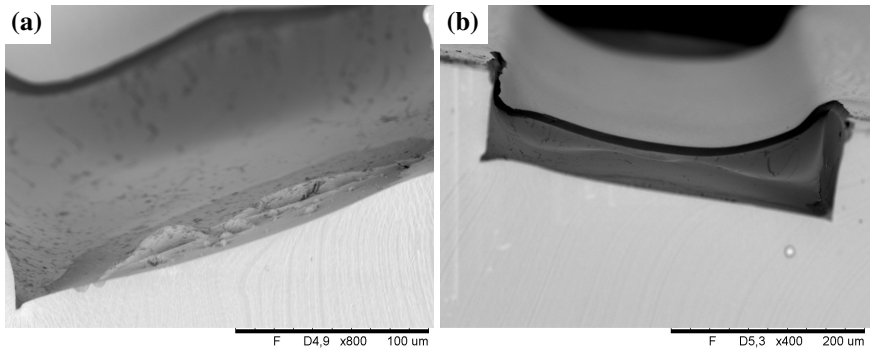

Figure 4.24: Table top SEM micrographs of outlet channels during different stages of alginate/CaP buildup. **(a)** In early stages, small particles ($< 10\,\mu m$) are observed along the top and bottom surfaces of the outlet channel. **(b)** A buildup of materials progresses, the whole surface of the channel is covered

4.10 SEM Characterization of Fibers

Collected fibers were characterized using FE-SEM as described in section 3.1. Fibers were embedded in an agarose hydrogel for mechanical support and to prevent unintended drying during sample preparation. Cross sections of the cylinders were prepared with a vibratome to study the internal structure. The preparation procedure is explained in section 3.1.

FE-SEM micrographs of unmineralized and mineralized fiber cross sections is shown in Figure 4.25. Ellipse shaped fibers are surrounded by agarose. Parallel lines observed in both alginate and agarose are likely caused by the vibratome blade during sectioning. Fibers with higher mineral content shrunk less during sample preparation and remained in contact with the agarose matrix while unmineralized and low-mineralized fibers shrunk and released. Micrographs reveal an uneven surface of the fibers with highest mineral content consistent with optical microscope images in Figure 4.22b.

The alginate microstructure in regions near the edge and center of fibers are shown in FE-SEM micrographs in Figure 4.26. Unmineralized CaA fibers have a dense structure throughout the cross section. Mineralized fibers have a denser structure close to the perimeter, compared to the center. Porosity if the fibers increased with mineral content.

Higher magnification micrographs of 200 mM PI^- fibers in Figure 4.27 show sheet-like structures not present in unmineralized alginate that are likely CaP minerals. More minerals are present at the edge compared to the center of mineralized fibers. Backscattered electron images in Figure 4.27c reveal a anisotropic distribution of minerals with higher concentration around the perimeter.

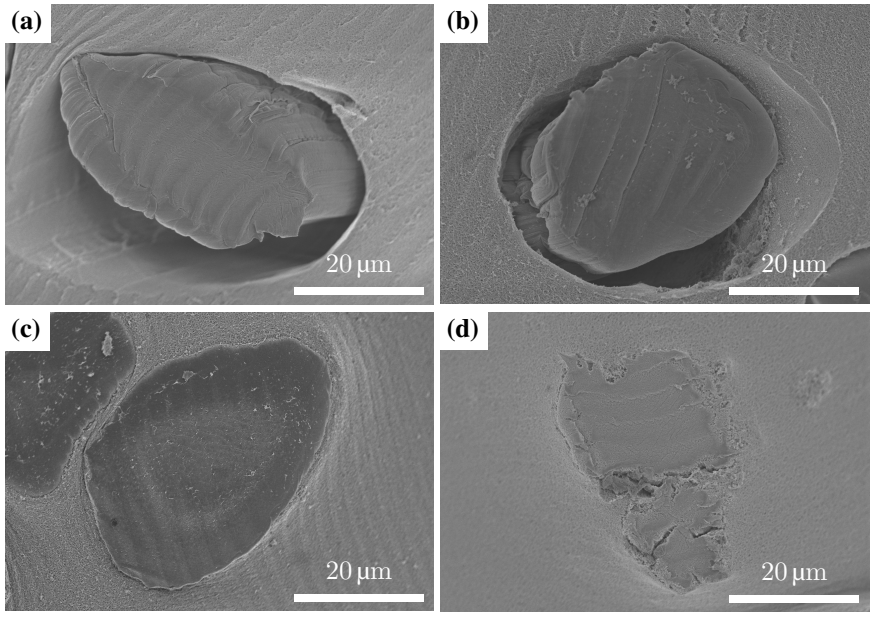

Figure 4.25: FE-SEM micrographs of CaA fibers embedded in agarose. Phosphate content in NaA flow: **(a)** Unmineralized **(b)** 100 mM PI^- **(c)** 200 mM PI^- **(d)** 300 mM PI^-

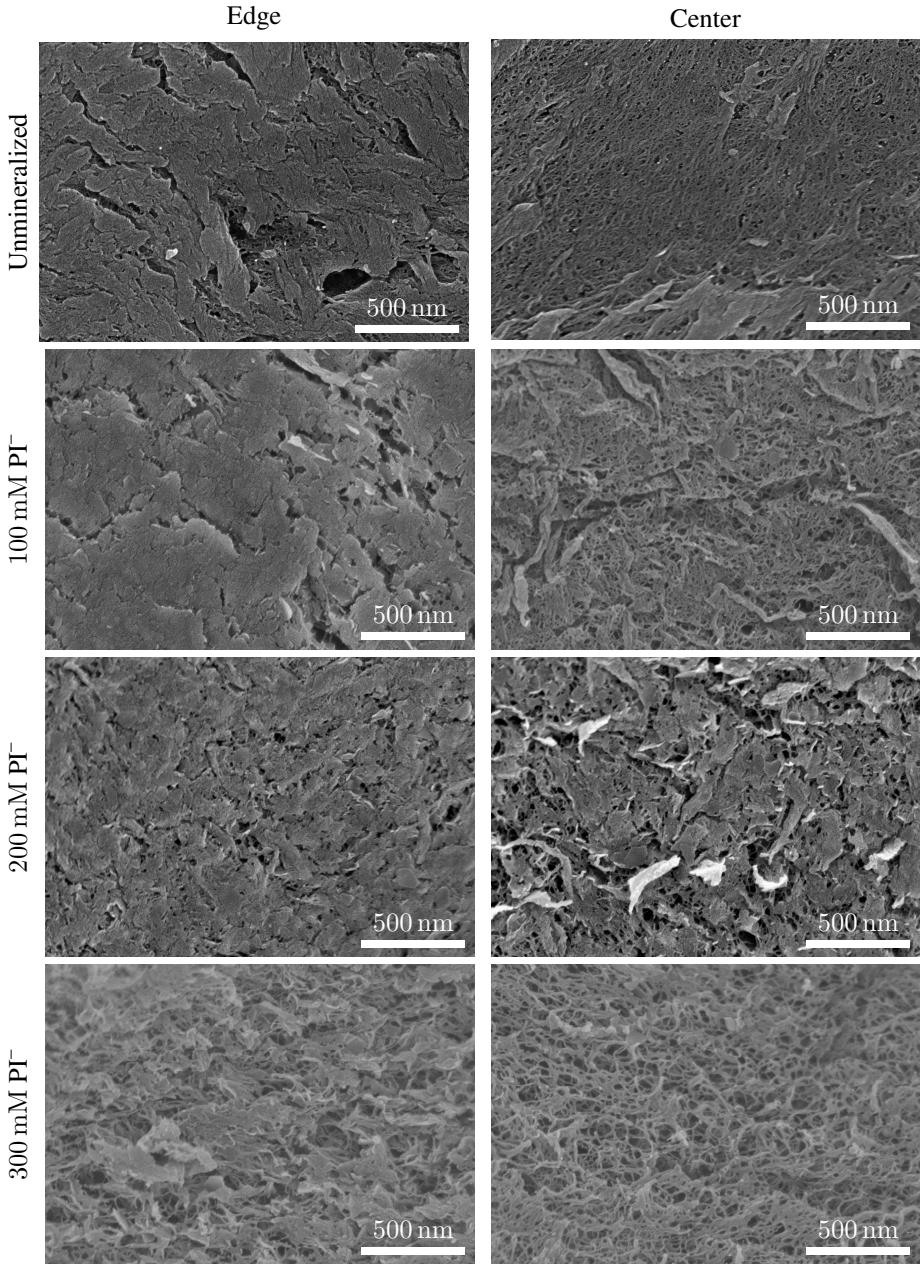

Figure 4.26: FE-SEM micrographs of microstructure in CaA fiber cross sections embedded in agarose. Micrographs in the left column show microstructure of the cross-section close to the fiber perimeter. The right column shows structure in the center of the fiber. PI^-concentration is increasing for each row.

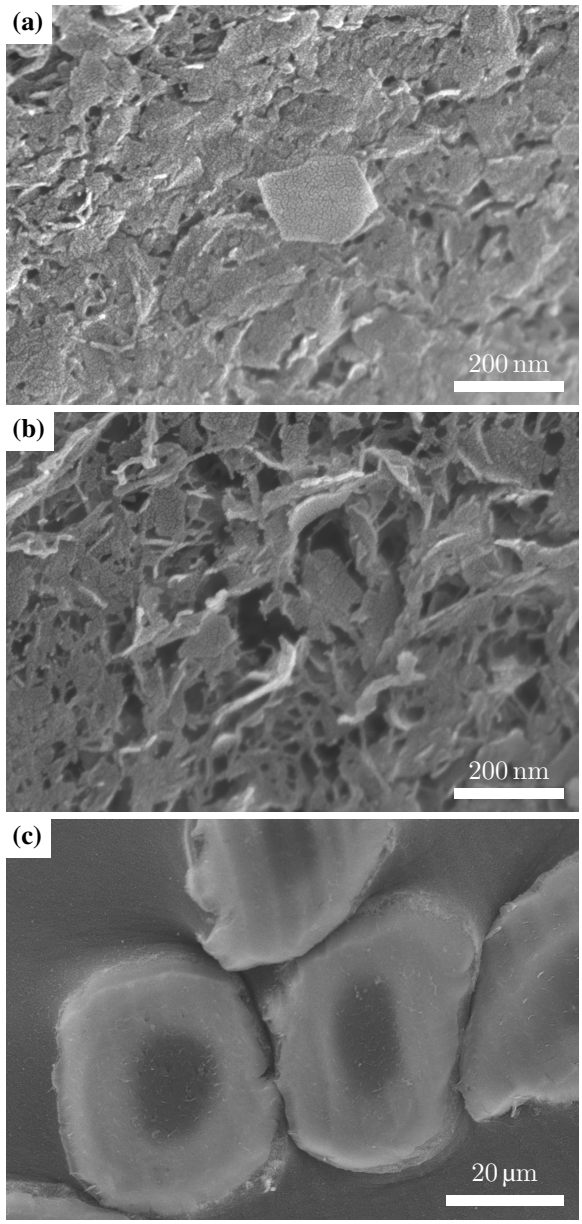

Figure 4.27: FE-SEM micrographs of 200 mM PI^-fiber cross sections show distribution of CaP minerals. **(a)** Dense structure of alginate and phosphate minerals near the edge. **(b)** Less dense structure in the center of the fiber. Calcium phosphate minerals form thin sheets among alginate matrix. **(c)** BSE micrographs reveals anisotropic distribution of minerals in the fibers. $V_{acc} = 10\,kV$ for BSE micrographs

5 Discussion

5.1 Fabrication Strategies

The goal of this work has been to develop a fabrication method for mineralized calcium alginate (CaA) fibers for tissue engineering applications. Two approaches based on different microfluidic devices have been investigated. Both glass capillary and PDMS-based microfluidic devices have several advantages over alternative fabrication methods for alginate fibers. Microfibers of CaA with circular and elliptical cross sections can be produced continuously in a simple and cost effective way with uniform size distribution. Both microfluidic devices examined are flexible in the way that different geometries may be achieved with the control of flow rates without any need for changing the design of the device. The sodium alginate (NaA) flow is only briefly exposed to high concentration $CaCl_2$flow in both designs.

There are important differences between the designs that are essential for the successful fabrication of fibers. The following points will be discussed in detail for the fabrication approaches examined:

- The devices must be fabricated with dimensions that closely match the design. Flow rates and resistances are highly dependent on dimensions of the channels, which must be fabricated with minimal variation between devices to ensure equal flow conditions in all devices.

- Stable coaxial flow must be initiated and maintained to prevent unwanted gelation that results in clogging of the devices.

- Fibers produced must have a narrow size distribution. Control of thickness through flow rates increases the versatility of the device.

- Buildup of debris and gel/minerals inside the device that leads to failure must be avoided.

Devices must be fabricated with reproducible geometries to achieve identical flow conditions between devices. In addition, it is preferable that the devices can be made with standard microfabrication techniques. Glass capillary devices were manufactured using a simple process requiring no special equipment nor cleanroom processing. Due to the manual glass capillary pulling process, there was a large variation in diameter of the capillary tips. Glass capillaries with intended diameter of $100\,\mu m$ could not be supplied in large numbers. The glass capillary devices are based on the work of Jeong et al. [66], where a programmable micropipette puller was used for fabrication of fibers, which resulted in better control of dimensions and uniformity. A programmable micropipette puller was not available at NTNU.

Good control over channel geometry could be achieved in PDMS based devices that were fabricated using photolithography and replica molding. Fabrication in cleanrooms is required for the molds, but the rest of the process can be performed in ambient conditions. Once manufactured, the silanized molds are durable and can be reused for a number of times (> 10). The replica molding process results in identical devices as long as the mold is undamaged, so variations from device to device are avoided. Lithography with polymer film masks using standard parameters results in sufficient resolutions for fabricating channels with width of $50\,\mu m$ or more. Achieving a constant height of the channels proved to be the most challenging aspect of fabrication as shown in height measurements in Figure 4.10. Due to the size of the microfluidic device, the channels covered almost the entire diameter of 2 inch wafers, and large thickness variations were observed close to the perimeter due to edge beads. Increasing wafer size to 4 inch allows the design to be centered in the region of flatter resist in the center of the wafer, and edge beads to be removed without interfering with the design.

The rapid gelation when NaA and $CaCl_2$ flows meet complicates the initiation of flow in glass capillary devices. Plugs of CaA form where the two flows meet, either in the pulled glass capillary or outlet pipe. For unmineralized fibers the plugs can in most cases be cleared by increasing flow rates of the NaA or $CaCl_2$. For NaA soltution containing PI^-, the mineralized mass forming could not be removed. Shin et al. [23] fabricated CaA fiber with the same approach and did not report any issues with upstream gelation using a similar setup and stepwise introduction of flows. A smaller pulled pipette was used with ($35\,\mu m$) diameter that is less prone to reverse flow due to higher flow resistance. Prefilling the glass capillary device with DI water may be a possible solution for avoiding plug formation. A region of water between the NaA and $CaCl_2$ solution could act as a diffusion barrier to prevent gelation inside the device.

PDMS devices are less prone to unintended gelation during flow initiation due to the addition of a buffer flow. Filling all channels with DI water and achieving stable flow of buffer and $CaCl_2$ before initiation of NaA is an effective way of preventing reverse flow. Gelation may be initiated and terminated by modifying buffer flow rate allowing more control of the gelation process compared to the glass capillary devices. However, care must be taken to prevent reverse flow into the buffer channels during device operation. Three parameters have been found to be important for maintaining stable coaxial flow in the PDMS device: flow rates, viscosity of the flows and channel geometry which affect pressures and resistances in the channels and junctions. Device failure was primarily caused by reverse flow into the buffer channel. Flow rate of the buffer and $CaCl_2$ flow had to be kept above

a minimum to prevent reverse flow. Increasing the viscosity of the buffer and $CaCl_2$ flow with the addition of dextran allowed stable flow to be achieved over a larger range of flow rates. Resistance channels consisting of curved, narrow regions of channel upstream of the junctions further improves stability of the devices. The addition or resistance channels increases the complexity of fabrication. Narrow channels are prone to defects during photolithography, while increased channel length increase the problems related to bubbles in resist and delamination. A balance must be found between ease of fabrication and flow stability.

Buildup of debris in PDMS devices occurs in the NaA channel downstream of the filters and is concentrated in narrowing portions of the channels as well as in bends. Micrographs in Figure 4.21 shows buildup this buildup. Table top SEM images of filters in the finished device in Figure 4.11 reveal some widening of the filters due to rounding of the edges, but debris significantly larger than the filter spacing are observed in the channels, downstream of the filters. If filters do not bond well to the glass slide , debris can pass between the pillars and the glass. Pillars may deform or the debris themselves can squeeze through the features. A more effective removal of debris can be achieved by adding a filtering step during preparation of the NaA solution. Sodium alginate solutions can be filtered through a series of membrane filters with decreasing pore sizes from $1.2\,\mu m$ to $0.2\,\mu m$ in order to eliminate most of the contaminating particles [75, p. 249]. Performing filtering during preparation of the solutions, allows the filter in the PDMS device to be removed. Photolithography is simplified as the smallest design features are now the channels ($> 50\,\mu m$) instead of filters ($12.5\,\mu m$).

Both glass capillary and PDMS microfluidic devices were successful in fabricating unmineralized fibers with flow rate dependent thickness with low variations as shown in Figures 4.4 and 4.20. Results indicate that coaxial flow can be generated and maintained over a period of time for both investigated devices. The residence time of the alginate inside the outlet channel is sufficient for gelation to occur resulting in fibers that may be handled as soon as the exit the device. Fabrication in glass capillary devices results in fibers with circular cross sections due to the shape of the pulled capillary. Identical devices with smaller pipette diameter of $35\,\mu m$ were used by Shin et al. [23] to make fibers with diameter in the range $20\,\mu m$ – $50\,\mu m$, showing that smaller fibers may be fabricated with the appropriate pipette geometry.

PDMS devices result in fibers with elliptical cross sections due to the rectangular channel geometry. For all flow rates investigated, at least one of the axes of the fiber cross sections shown in 4.20 is less than the channel height of $90\,\mu m$, indicating coaxial flow is generated in the outlet channel, where the highly viscous NaA flow is lubricated by buffer/$CaCl_2$ flow. PDMS devices are more flexible as fibers with larger variations in thickness can be made with the same device. Thickness variations for fibers fabricated with both devices are likely caused by variations in flow rates or elongation due to mechanical forces during handling.

The addition of phosphate ions the NaA stream results in buildup of CaA and calcium phosphate minerals (CaP) along device walls for both designs. For glass capillary devices buildup occurs at tip of capillary, precipitation and gelation happens almost instantaneously when the two flows meet. CaP minerals forming at the tip of the pulled glass pipette serve as a base for further accumulation of alginate and minerals. The addi-

tion of a buffer flow in the PDMS devices acts as a diffusion barrier that delays gelation and prevents buildup at the junction. However, buildup of CaA/CaP occurs downstream in the outlet channel. The outwards diffusion of PI^- into the buffer channels will result in precipitation of CaP minerals when in contact with inwards diffusing Ca^{2+}-ions. Minerals precipitate along the top and bottom surfaces of the outlet channel are observed in SEM micrographs in Figure 4.24 that grow and result in clogging of the outlet channel. The widening shape of the deposited minerals further downstream in the channel in Figure 4.23 indicates that this is a diffusive process as it increases with residence time in the channel. The PDMS device is effective at separating the NaA flow from device walls in the device plane due to the wide buffer and $CaCl_2$ flow. However, alginate fibers are not well separated from the top and bottom device surfaces inside the outlet channel. For example a $40\,\mu m$ thick fiber in a $90\,\mu m$ has only $25\,\mu m$ separation on each side. This distance is even less when flow disturbances occur. A strategy to avoid minerals forming along top/bottom is to increase the distance between fiber and surfaces. The fibers can be separated more from top/bottom walls by using a 3D nozzle geometry similar to the glass capillary devices where a narrow channel containing NaA and buffer flows is injected into a wider cylindrical PDMS channel and surrounded with a sheath flow of $CaCl_2$. An even separation from surfaces controlled by device geometries would be achieved with a nozzle design. Kang et al. [76] describe a 3D microfluidic nozzle device fabricated using PDMS replica molding. The fabrication process for SU-8 molds is considerably more advanced compared to standard 2D photolithography used in this work.

5.2 Structure and Composition of Fibers

PDMS microfluidic devices have been used for the fabrication of CaA fibers. Short sections of mineralized fibers have successfully been fabricated from NaA solutions containing up to $300\,mM$ PI^- ions using a triple flow design in PDMS devices. Fibers were collected and characterized using optical microscopy and FE-SEM.

Fibers are visibly deformed by the sample preparation procedure for SEM as shown in Figure 4.25 and degree of deformation decreases with PI^- content of the NaA flow. Deformation is likely to be caused by mechanical stress during vibratome cutting or surface tension during drying which results in collapse of the alginate network. Increased resistance to deformation could be caused by higher stiffness of the fibers due to the presence of CaP minerals in the gel. Compression studies on mineralized alginate beads by Olderøy et al. [47] show that the apparent Young's and the related shear modulus is increased compared to unmineralized beads. For mineralization with the counter diffusion approach, the apparent Young's modulus increases with increasing mineral content. The elastic component of the response was shown to become more important as mineral content increased as reorganization of the polymer network was slower and probably hindered by the presence of mineral particles. The increased stiffness and dominating elastic response of mineralized fibers could explain the decreased destruction and shrinking when preparing fiber cross sections. The fiber collection, sectioning and drying process has many parameters that could lead to collapse of the gel structure. Mechanical testing of the fibers will therefore have to be performed before any conclusions about mechanical properties can be drawn.

Fibers containing 300 mM PI^- have an irregular structure with cross sections that are

not elliptical as observed for minerals with lower PI^-content in Figure 4.25. The irregular structure is also apparent in optical micrographs of the fibers in Figure 4.22 where the fibers have a less smooth surface. Experiments with fabrication of mineralized alginate beads by the counter diffusion method also result in deformed structure for PI^-concentrations of $300\,\mathrm{mM}$ [17]. Calcium ions are likely provided at a too low rate for combined rapid gelation and CaP precipitation. The competitive binding of Ca^{2+}ions may put an upper limit for the concentration of PI^-in the NaA flow. Increasing $CaCl_2$concentration in the gelling flow and decreasing buffer width could be done to increase flux of Ca^{2+}ions. Buildup of gel/minerals along device walls disturbs flow which could result in deformed fibers as well.

The inhomogeneous distribution of CaP minerals seen observed in the BSE micrograph in Figure 4.27c is likely caused by the outwards diffusion of PI^-as the inwards diffusion Ca^{2+}-ions leads to precipitation of CaP from the fiber perimeter and inwards. This process has been observed in alginate discs, resulting in a ring of minerals along the perimeter, but little minerals in the center [1]. Mineralized microbeads produced by the counter-diffusion method have previously been shown to have a inhomogeneous structure with CaP minerals concentrated around the perimeter of the beads[77].

5.3 Future Work

Additional process optimization is required in order to achieve stable fabrication of mineralized fibers. A major limitation is the buildup of minerals along fiber walls. Design modifications have been proposed for PDMS devices, but they result in an increased complexity of making the devices. An alternative approach involves using the same devices, but with a different mineralization process. Mineralization of alginate beads may be done in an enzymatic process utilizing alkaline phosphatase (ALP)[18]. Alkaline phosphatase is one particularly important enzyme involved in the bone formation process which liberates phosphates necessary for mineralization. A precursor of NaA and ALP is flown the center flow and gelation occurs as previously, but no mineralization is preformed inside the device. The fibers are collected and incubated in a bath of $CaCl_2$and β-glycerophosphate in tris-buffer for 24hr. Mineralization takes place outside the device, when phosphate ions are released from enzymatic breakdown of β-glycerophosphate by ALP. The ALP mineralization approach prevents the formation of CaP inside the outlet channel, which is the primary cause of device failure.

Fibers must be collected in a controlled way for future use. Uneven pulling that may deform the fibers or lead to breaking must be avoided and the collected fibers must be prevented from drying. Yamada et al. [74] collected fabricated fibers on a partially submerged roller. Rotation speed of the roller was adjusted to match flow velocity in the devices. A similar design may be set up using a PVC collection roller mounted to a geared electrical motor. Rotation speed is adjusted by changing power supply voltage.

6 Conclusion

Calcium phosphate mineralized hydrogels are promising materials for the use as synthetic extracellular matrix in bone tissue engineering. Mineralized alginate fibers embedded in unmineralized alginate gel have been proposed as a method for mimicking the directional structures found in bone tissue. The goal for this project has been to develop a method for microfluidic fabrication of mineralized calcium alginate fibers. Two strategies involving coaxial flow in microchannels have been investigated.

A glass capillary microfluidic device was investigated for the fabrication of unmineralized fibers. Fibers were fabricated with circular cross section and uniform size distribution controlled by relative flow rates of the sodium alginate (NaA) and $CaCl_2$. Simultaneous gelation and mineralization by a counter diffusion approach was attempted by adding phosphate ions to the sodium alginate flow. Rapid accumulation of mineralized calcium alginate (CaA) gels along device walls resulted in irreversible clogging of the glass capillary devices. Buildup of mineralized CaA occurred where NaA and $CaCl_2$streams joined next to the glass capillary wall.

Based on results with glass capillary devices, and new device was developed where a third flow of DI water was flown between the NaA and $CaCl_2$flow to delay the onset of gelation until the flows clear the device walls. Unmineralized alginate fibers were fabricated with elliptical cross sections with geometry controlled by flow rates. It was necessary to increase the viscosity of the buffer and $CaCl_2$flow by adding dextran in order to achieve stable flow and fiber formation. Flow stability was further improved by increasing flow resistance for buffer and $CaCl_2$flows. Short stretches of calcium phosphate mineralized alginate fibers with phosphate ion content between $100\,\mathrm{mM}$ and $300\,\mathrm{mM}$ were successfully fabricated. Precipitation of CaP minerals and subsequent alginate buildup along channel walls resulted in failure of the device.

Synthesized fibers were characterized using optical and scanning electron microscopy. FE-SEM micrographs of fiber cross sections revealed a core shell structure where CaP mineralized were concentrated around the perimeter of the fiber. CaP minerals were observed as sheets in the alginate network. Minerals were also visible in optical microscopes as a dark region around the perimeter of the fiber. Mineralized fibers were less prone to

shrinking and deformation during sample preparation for SEM characterization which is indicative of higher mechanical strength, although this requires further mechanical characterization to conclude.

Further development of the process is required for the stable fabrication of mineralized fibers. Proposed approaches include modified device geometry or a modified mineralization process. Geometry modifications for the device have been proposed to further separate the mineralized fibers from the device walls in order to prevent buildup and clogging. An alternative enzymatic mineralization strategy has been proposed, in where mineralization inside the microchannel is avoided. A setup for collection of fibers has also been discussed.

Bibliography

[1] Stefan Mandaric. Microfabrication for mineralized, hydrogel-based materials for tissue engineering applications. *Project Thesis*, 2014.

[2] Matilde Bongio, Jeroen J. J. P. van den Beucken, Sander C. G. Leeuwenburgh, and John A. Jansen. Development of bone substitute materials: from 'biocompatible' to 'instructive'. *Journal of Materials Chemistry*, 20(40):8747, October 2010.

[3] Gail Chan and David J Mooney. New materials for tissue engineering: towards greater control over the biological response. *Trends in biotechnology*, 26(7):382–92, July 2008.

[4] Kuen Yong Lee and David J Mooney. Alginate: properties and biomedical applications. *Progress in polymer science*, 37(1):106–126, January 2012.

[5] Siddhesh N Pawar and Kevin J Edgar. Alginate derivatization: a review of chemistry, properties and applications. *Biomaterials*, 33(11):3279–305, April 2012.

[6] Magnus Ø Olderøy. Bioinspired mineralization of alginate hydrogels. *Doctoral thesees at NTNU*, 239, 2011.

[7] U. G. K. Wegst and M. F. Ashby. The mechanical efficiency of natural materials. *Philosophical Magazine*, 84(21):2167–2186, July 2004.

[8] Hans-Jürgen Weiss Wolfgang Pompe, Gerhard Rödel. Biomineralization. In *Bio-Nanomaterials: Designing Materials Inspired by Nature*, chapter 6, pages 237–366. Wiley-VCH Verlag GmbH & Co. KGaA, first edit edition, 2013.

[9] James D Kretlow and Antonios G Mikos. Review: mineralization of synthetic polymer scaffolds for bone tissue engineering. *Tissue engineering*, 13(5):927–38, May 2007.

[10] Therese Andersen, Bent L Strand, Kjetii Formo, Eben Alsberg, and Bjørn E Christensen. Alginates as biomaterials in tissue enginneering. In Thisbe Pilar Rauter, Amelia, Lindhorst, editor, *Carbohydrate Chemistry : Volume 37*. The Royal Society of Chemistry, London, 2012.

[11] Alexander D Augst, Hyun Joon Kong, and David J Mooney. Alginate hydrogels as biomaterials. *Macromolecular bioscience*, 6(8):623–33, August 2006.

[12] Britt Iren Glarum Svanem, Gudmund Skjåk-Bræk, Helga Ertesvag, and Svein Valla. Cloning and Expression of Three New Azotobacter vinelandii Genes Closely Related to a Previously Described Gene Family Encoding Mannuronan C-5-Epimerases. *J. Bacteriol.*, 181(1):68–77, January 1999.

[13] P. A. J. Gorin and J. F. T. Spencer. Exocellular alginic acid from Azobacter Vinelandii. *Canadian Journal of Chemistry*, 44(9):993–998, May 1966.

[14] Meirigeng Qi, Berit Løkensgard Strand, Yrr Mørch, Igor Lacik, Yong Wang, Payam Salehi, Barbara Barbaro, Antonio Gangemi, Joseph Kuechle, Travis Romagnoli, Michael A Hansen, Lisette A Rodriguez, Enrico Benedetti, David Hunkeler, Gudmund Skjå k Braek, and José Oberholzer. Encapsulation of human islets in novel inhomogeneous alginate-ca2+/ba2+ microbeads: in vitro and in vivo function. *Artificial cells, blood substitutes, and immobilization biotechnology*, 36(5):403–20, January 2008.

[15] Maritie Grellier, Pedro L Granja, Jean-Christophe Fricain, Sílvia J Bidarra, Martine Renard, Reine Bareille, Chantal Bourget, Joelle Amédée, and Mário A Barbosa. The effect of the co-immobilization of human osteoprogenitors and endothelial cells within alginate microspheres on mineralization in a bone defect. *Biomaterials*, 30(19):3271–8, July 2009.

[16] Jon A. Rowley, Gerard Madlambayan, and David J. Mooney. Alginate hydrogels as synthetic extracellular matrix materials. *Biomaterials*, 20(1):45–53, January 1999.

[17] Minli Xie, Magnus Ø Olderøy, Jens-Petter Andreassen, Sverre Magnus Selbach, Berit L Strand, and Pawel Sikorski. Alginate-controlled formation of nanoscale calcium carbonate and hydroxyapatite mineral phase within hydrogel networks. *Acta biomaterialia*, 6(9):3665–75, September 2010.

[18] Minli Xie, Magnus Ø. Olderøy, Zhibing Zhang, Jens-Petter Andreassen, Berit L. Strand, and Pawel Sikorski. Biocomposites prepared by alkaline phosphatase mediated mineralization of alginate microbeads. *RSC Advances*, 2(4):1457, January 2012.

[19] Marita Westhrin. Encapsulation of Human Mesenchymal Stem Cells in Phosphate Mineralized Alginate Beads. *Master Thesis*, 2011.

[20] Teresa R Cuadros, Olivier Skurtys, and Josè M Aguilera. Mechanical properties of calcium alginate fibers produced with a microfluidic device. *Carbohydrate polymers*, 89(4):1198–206, August 2012.

[21] Ali Tamayol, Mohsen Akbari, Nasim Annabi, Arghya Paul, Ali Khademhosseini, and David Juncker. Fiber-based tissue engineering: Progress, challenges, and opportunities. *Biotechnology Advances*, 31(5):669–687, 2013.

[22] C. M. Hwang, Y. Park, J. Y. Park, K. Lee, K. Sun, A. Khademhosseini, and S. H. Lee. Controlled cellular orientation on PLGA microfibers with defined diameters. *Biomedical Microdevices*, 11(4):739–746, 2009.

[23] Su-Jung Shin, Ji-Young Park, Jin-Young Lee, Ho Park, Yong-Doo Park, Kyu-Back Lee, Chang-Mo Whang, and Sang-Hoon Lee. "On the fly" continuous generation of alginate fibers using a microfluidic device. *Langmuir : the ACS journal of surfaces and colloids*, 23(17):9104–8, August 2007.

[24] TJ Painter, O Smidsrød, and A Haug. A computer study of the changes in composition-distribution occurring during random depolymerisation of a binary linear heteropolysaccharide. *Acta Chem Scand*, 22:1637–1648, 1968.

[25] O Smidsrød and Gudmund Skjåk-Bræk. Alginate as immobilization matrix for cells. *Trends in Biotechnology*, 8:71–78, 1990.

[26] Hans Grasdalen. High-field, 1H-n.m.r. spectroscopy of alginate: sequential structure and linkage conformations. *Carbohydrate Research*, 118:255–260, July 1983.

[27] A Martinsen, I Storrø, and G Skjårk-Bræk. Alginate as immobilization material: III. Diffusional properties. *Biotechnology and bioengineering*, 39(2):186–94, January 1992.

[28] Yrr A Mørch, Ivan Donati, Berit L Strand, and Gudmund Skjåk-Bræk. Effect of Ca2+, Ba2+, and Sr2+ on alginate microbeads. *Biomacromolecules*, 7(5):1471–80, May 2006.

[29] E Onsøyen. Commercial applications of alginates. *Carbohydr. Eur*, 14:26–31, 1996.

[30] Gregor T. Grant, Edwin R. Morris, David A. Rees, Peter J.C. Smith, and David Thom. Biological interactions between polysaccharides and divalent cations: The egg-box model. *FEBS Letters*, 32(1):195–198, May 1973.

[31] Bjørn T. Stokke, Olav Smidsrød, Flavio Zanetti, Wenche Strand, and Gudmund Skjåk-Bræk. Distribution of uronate residues in alginate chains in relation to alginate gelling properties — 2: Enrichment of β-d-mannuronic acid and depletion of α-l-guluronic acid in sol fraction. *Carbohydrate Polymers*, 21(1):39–46, January 1993.

[32] Edwin R. Morris, David A. Rees, David Thom, and Jonathan Boyd. Chiroptical and stoichiometric evidence of a specific, primary dimerisation process in alginate gelation. *Carbohydrate Research*, 66(1):145–154, October 1978.

[33] Ivan Donati, Synnøve Holtan, Yrr A Mørch, Massimiliano Borgogna, Mariella Dentini, and Gudmund Skjåk-Bræk. New hypothesis on the role of alternating sequences in calcium-alginate gels. *Biomacromolecules*, 6(2):1031–40, 2005.

[34] K I Draget, B Strand, M Hartmann, S Valla, O Smidsrød, and G Skjåk-Bræk. Ionic and acid gel formation of epimerised alginates; the effect of AlgE4. *International journal of biological macromolecules*, 27(2):117–22, April 2000.

[35] A Martinsen, G Skjåk-Bræk, and O Smidsrød. Alginate as immobilization material: I. Correlation between chemical and physical properties of alginate gel beads. *Biotechnology and bioengineering*, 33(1):79–89, January 1989.

[36] J.-M. Duez, M. Mestdagh, R. Demeure, J.-F. Goudemant, B. P. Hills, and J. Godward. NMR studies of calcium-induced alginate gelation. Part I?MRI tests of gelation models. *Magnetic Resonance in Chemistry*, 38(5):324–330, May 2000.

[37] Beate Thu, Olav Gåserød, and Didrik Paus. Inhomogeneous alginate gel spheres: An assessment of the polymer gradients by synchrotron radiation induced x-ray emission, magnetic resonance microimaging,. . . . , 53:60–71, 2000.

[38] Berit L. Strand, Yrr a. Mø rch, Terje Espevik, and Gudmund Skjå k Bræ k. Visualization of alginate-poly-L-lysine-alginate microcapsules by confocal laser scanning microscopy. *Biotechnology and Bioengineering*, 82:386–394, 2003.

[39] YA Mørch. *Novel Alginate Microcapsules for Cell Therapy–A study of the structure-function relationships in native and structurally engineered alginates*. PhD thesis, NTNU, 2008.

[40] Sergey V Dorozhkin. Calcification and Biomimetic Applications Calcium Orthophosphates. *Biomatter*, 1(2):121–164, 2011.

[41] Sergey V Dorozhkin and Matthias Epple. Biological and medical significance of calcium phosphates. *Angewandte Chemie (International ed. in English)*, 41(17):3130–46, September 2002.

[42] G. Daculsi, R. Z. LeGeros, and D. Mitre. Crystal dissolution of biological and ceramic apatites. *Calcified Tissue International*, 45(2):95–103, 1989.

[43] Timothy E L Douglas, Elzbieta Pamula, and Sander C G Leeuwenburgh. Biomimetic Mineralization of Hydrogel Biomaterials for Bone Tissue Engineering. In *Biomimetics*, pages 51–67. Scrivener Publishing LLC, Beverly, MA, 2013.

[44] Marita Westhrin, Minli Xie, Magnus Ø. Olderø y, Pawel Sikorski, Berit L. Strand, and Therese Standal. Osteogenic Differentiation of Human Mesenchymal Stem Cells in Mineralized Alginate Matrices. *PLOS ONE*, 10(3):e0120374, 2015.

[45] Ingrid Le. Biomineral-inspired fabrication of semi-permeable calcium phosphate–polysaccharide microcapsules. pages 10–12, 2002.

[46] Minli Xie, Magnus ØOlderø y, Jens-Petter Andreassen, Sverre Magnus Selbach, Berit L Strand, and Pawel Sikorski. Alginate-controlled formation of nanoscale calcium carbonate and hydroxyapatite mineral phase within hydrogel networks. *Acta biomaterialia*, 6(9):3665–75, September 2010.

[47] Magnus O. Olderø y, Minli Xie, Jens Petter Andreassen, Berit L. Strand, Zhibing Zhang, and Pawel Sikorski. Viscoelastic properties of mineralized alginate hydrogel beads. *Journal of Materials Science: Materials in Medicine*, 23(7):1619–1627, 2012.

[48] John Dingley. The photo-mask guide. `http://en.calameo.com/read/0001274256f3e90753b8a`, 2014. Online. Accessed: 2015-04-27.

[49] Su-8 2000 permanent epoxy negative photoresist. `http://www.microchem.com/pdf/SU-82000DataSheet2000_5thru2015Ver4.pdf`, 2015. Online. Accessed: 2015-04-27.

[50] H. Lorenz, M. Despont, N. Fahrni, J. Brugger, P. Vettiger, and P. Renaud. High-aspect-ratio, ultrathick, negative-tone near-UV photoresist and its applications for MEMS. *Sensors and Actuators A: Physical*, 64(1):33–39, January 1998.

[51] Paul M. Dentinger, Karen L. Krafcik, Kelby L. Simison, Richard P. Janek, and John Hachman. High aspect ratio patterning with a proximity ultraviolet source. *Microelectronic Engineering*, 61-62:1001–1007, July 2002.

[52] Emmanuel Delamarche, David Juncker, and Heinz Schmid. Microfluidics for processing surfaces and miniaturizing biological assays. *Advanced Materials*, 17(24):2911–2933, 2005.

[53] J. Quirk, M. Serda. *Semiconductor Manufacturing Technology*. Prentice Hall, Upper Saddle River, NY, 1st edition, 2000.

[54] Younan Xia and George M. Whitesides. Soft Lithography. *Annual Review of Materials Science*, 28(1):153–184, 1998.

[55] J Cooper McDonald and George M Whitesides. Poly (dimethylsiloxane) as a Material for Fabricating Microfluidic Devices. *Accounts of Chemical Research*, 35(7):491–499, 2002.

[56] J Cooper Mcdonald, David C Duffy, Janelle R Anderson, and Daniel T Chiu. Review - Fabrication of microfluidic systems in poly (dimethylsiloxane). *Electrophoresis*, 21:27–40, 2000.

[57] M K Chaudhury and G M Whitesides. Direct Measurement of Interfacial Interactions between Semispherical Lenses and Flat Sheets of Poly(Dimethylsiloxane) and Their Chemical Derivatives. *Langmuir*, 7(5):1013–1025, 1991.

[58] JoshuaI Molho, RonaldJ Adrian, KendraV Sharp, and JuanG Santiago. Liquid Flows in Microchannels. In *MEMS*, The CRC Press Series in Mechanical and Aerospace Engineering, pages 10–53. CRC Press, November 2005.

[59] Steffen Hardt and Friedhelm Schönfeld. *Microfluidic technologies for miniaturized analysis systems*. 2007.

[60] Venkatachalam Chokkalingam, Boris Weidenhof, Michael Krämer, Wilhelm F Maier, Stephan Herminghaus, and Ralf Seemann. Optimized droplet-based microfluidics scheme for sol-gel reactions. *Lab on a chip*, 10(13):1700–1705, 2010.

[61] M Denn. *Process Fluid Mechanics*. Prentice Hall, Upper Saddle River, NY, 1980.

[62] Ha Stone. CMOS Biotechnology. *Biography An Interdisciplinary Quarterly*, 2007.

[63] G Falkovich. *Fluid Mechanics*. Cambridge University Press, Cambridge, 2011.

[64] J. P. Holman. *Heat Transfer*. McGraw-Hill, 2002.

[65] D. J Acheson. *Elementary Fluid Dynamics*. Oxford University Press, Oxford, 1990.

[66] Wonje Jeong, Jeongyun Kim, Sunjeong Kim, Sanghoon Lee, Glennys Mensing, and David J Beebe. Hydrodynamic microfabrication via"on the fly" photopolymerization of microscale fibers and tubes. *Lab on a chip*, 4(6):576–80, December 2004.

[67] Thomas Cubaud and Thomas G. Mason. Interacting viscous instabilities in microfluidic systems. *Soft Matter*, 8:10573, 2012.

[68] Ray F. Egerton. *Physical Principles of Electron Microscopy*. Springer Science + Business Media, Inc, New York, NY, 2005.

[69] R Goodhew, Peter J., Humphreys, J, Beanland. *Electron Microscopy and Analysis*. Taylor & Francis Inc, New York, NY, third edit edition, 2001.

[70] Vegar Ottesen. Bacterial Microarrays by Microcontact Printing. *Master Thesis*, 2014.

[71] L Reimer. *Scanning Electron Microscopy*. Springer-Verlag, Heidelberg, 2nd editio edition, 1998.

[72] Thomas F Anderson. Techniques for the presevation of three-dimensional structure in preparing specimens for the electron microscope. *Transactions of the New York Academy of Sciences*, 13(4 Series II):130–134, 1951.

[73] M E Smith and E H Finke. Critical point drying of soft biological material for the scanning electron microscope. *Investigative ophthalmology*, 11(3):127–132, 1972.

[74] Masumi Yamada, Sari Sugaya, Yoji Naganuma, and Minoru Seki. Microfluidic synthesis of chemically and physically anisotropic hydrogel microfibers for guided cell growth and networking. *Soft Matter*, 8:3122, 2012.

[75] M. Hjortso. *Cell Adhesion in Bioprocessing and Biotechnology*. Biotechnology and Bioprocessing. Taylor & Francis, 1994.

[76] Edward Kang, Su-Jung Shin, Kwang Ho Lee, and Sang-Hoon Lee. Novel PDMS cylindrical channels that generate coaxial flow, and application to fabrication of microfibers and particles. *Lab on a chip*, 10(14):1856–61, July 2010.

[77] Minli Xie, Magnus Ø. Olderø y, Zhibing Zhang, Jens-Petter Andreassen, Berit L. Strand, and Pawel Sikorski. Biocomposites prepared by alkaline phosphatase mediated mineralization of alginate microbeads. *RSC Advances*, 2(4):1457, 2012.

Appendices

A Photolithography Protocol

The following protocol was used for fabrication of molds for PDMS microfluidic devices.

1. **Wafer cleaning:** The wafer was cleaned by spraying with acetone, followed by isopropanol, 70% ethanol and subsequent blow drying with nitrogen gas. The wafer was plasma cleaned using 50 % O_2 and 50 W generator power for 5 min.

2. **Dehydration bake:** The wafer was placed on a $180\,^{\circ}\mathrm{C}$ hot plate for 10 min and cooled on an aluminum block for $> 10\,\mathrm{s}$.

3. **Spin-coating:** A thin adhesion layer of SU-8 was uniformly applied by using spin coating. The wafer was centered on the spin coater and $1\,\mathrm{mL}$ photoresist per inch of wafer diameter was dispersed on the center using a disposable plastic Pasteur pipette. An initial spread cycle at 500 rpm for 5 seconds was used to disperse the photoresist, followed by a spin cycle at 8000 rpm for 30 seconds. Acceleration of 300 rpm/s was used for both cycles.

4. **Soft bake:** Performed immediately after spin coating at two temperatures using separate hotplates. Baked at $65\,^{\circ}\mathrm{C}$ for 1 min, transfered to second hotplate and baked at $95\,^{\circ}\mathrm{C}$ for 3 min. Transferred to aluminum block for cooling.

5. **Exposure:** Flood exposure (whole wafer exposed without the use of a photomask) using i-line UV light (λ = $365\,\mathrm{nm}$) from a $275\,\mathrm{W}$ Hg-lamp in a MA6 mask aligner with a total dose of $100\,\mathrm{mJ}$.

6. **Post-exposure bake:** Immediately after exposure, the wafer was baked on hot plates using a two-step process. The first baking step was performed at $65\,^{\circ}\mathrm{C}$ for 1 min followed by $95\,^{\circ}\mathrm{C}$ on a second hot plate before cooling on a aluminum block.

7. **Spin-coating:** The wafer was centered on a spin coater and $1\,\mathrm{mL}$ per inch wafer diameter of SU-8 2100 resist was poured in center of the wafer using a disposable plastic spoon. Spin coating was performed at 500 rpm for 5 sec followed by 3000 rpm for 30 s with 300 rpm/s acceleration. Edge beads around the wafer perimeter were removed with a cotton swab.

8. **Soft bake:** performed immediately after spin coating at two temperatures using separate hotplates. Baked at $65\,^{\circ}\mathrm{C}$ for 5 min, transfered to second hotplate and baked at $95\,^{\circ}\mathrm{C}$ for 20 min. Transferred to aluminum block for cooling.

9. **Exposure:** The polyester mask was mounted on a square 4 inch glass plate using adhesive tape. The mask was mounted in the mask holder of a MA6 mask aligner and brought in contact with the sample using hard contact mode. The resist was exposed with i-line UV light (λ = $365\,\mathrm{nm}$) with a total dose of 600 mJ.

10. **Post-exposure bake:** Immediately after exposure at $65\,^{\circ}\mathrm{C}$ for 5 min. Using the same hotplate, baking temperature was ramped up to $95\,^{\circ}\mathrm{C}$ where the wafer was baked for 10 min. The wafer was transferred to an aluminum block for cooling.

11. **Development:** Development was performed using mr-Dev 600 developer solution. The wafer was submerged in developer for 10 min at room temperature. The developer bath was gently agitated. The developed wafer was rinsed in a bath of fresh developer solution for a few seconds, followed by spraying with isopropanol and drying with N_2 (g).

12. **Inspection:** The finished structure was inspected using optical microscope and profilometer and SEM. Wafers with large defects were scrapped.

B Soft Lithography Protocol

1. **Silanization:** The SU-8 mold vas silanized to simplify PDMS peeling. Approx $100\,\mu L$ of Trichloro(1H,1H,2H,2H,perfluorooctyl)silane was placed in a glass beaker on the bottom of a glass desiccator and wafers were places horizontally in a wafer holder above the beaker. The desiccator was evacuated for 15 min and sealed using the stopcock. The wafer was left in the desiccator overnight. The chamber was gently vented and the wafers were removed. The mold was baked at $80\,^{\circ}C$ for 2 hours.

2. **Mixing and pouring:** A 1:10 ratio of PDMS curing agent (cross-linker) and base (siloxane) was measured using a digital scale. Using a plastic spoon, the two components were thoroughly mixed for 5 min. The wafer was placed inside a 3 inch plastic petri dish and approx. 20 g mixed PDMS was gently poured over the wafer.

3. **Degassing:** The poured PDMS was degassed for 30-45 min in a vacuum desiccator. The chamber was vented every 15 min for improved pumping efficiency. Any remaining bubbles were removed using a plastic spoon.

4. **Curing:** The PDMS was cured at $65\,^{\circ}C$ for 2 hours.

5. **Peeling:** After cooling, a scalpel was used to cut the PDMS around the wafer edge. The PDMS was peeled from the mold slowly, using a plastic tweezer. Excess PDMS surrounding the features was cut away with a scalpel.

6. **Hole punching and cleaning:** The PDMS was placed with the feature side up and inlet were made using a $1.5\,mm$ UniCore hole puncher. The device was cleaned by applying and peeling tape several times.

7. **Glass bonding:** A glass microscope slide was cleaned by spraying with acetone, followed by isopropanol, 70% ethanol and subsequent blow drying with nitrogen gas. The slide was dehydration baked on a $180\,^{\circ}C$ hot plate for 10 min and cooled on an aluminum block for $> 10\,s$. The glass and PDMS surfaces were activated using a plasma cleaner with 50% O_2 and $50\,W$ RF generator power for 24 s. The surfaces were brought in contact by hand so that the outlet channel (end of the wide channel) was positioned at the edge of the glass slide. The bond was finalized by curing at $80\,^{\circ}C$ for 15 min. After curing, PDMS exceeding the glass slide was cut away with a scalpel and the inlet holes holes were covered with tape to prevent contamination.

C Mask Designs

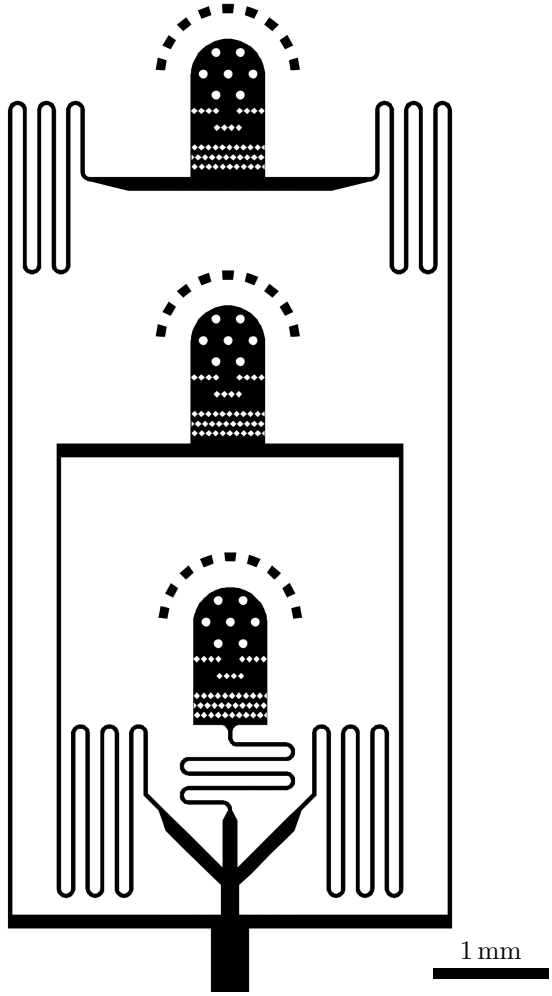

Figure C.1: Original design of PDMS microfluidic device

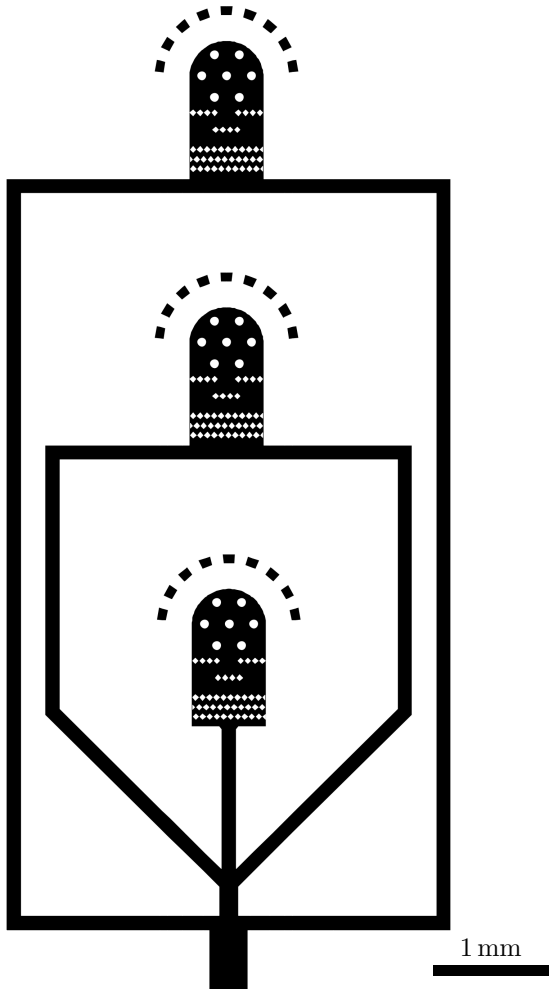

Figure C.2: Modified design 1: No resistance channels

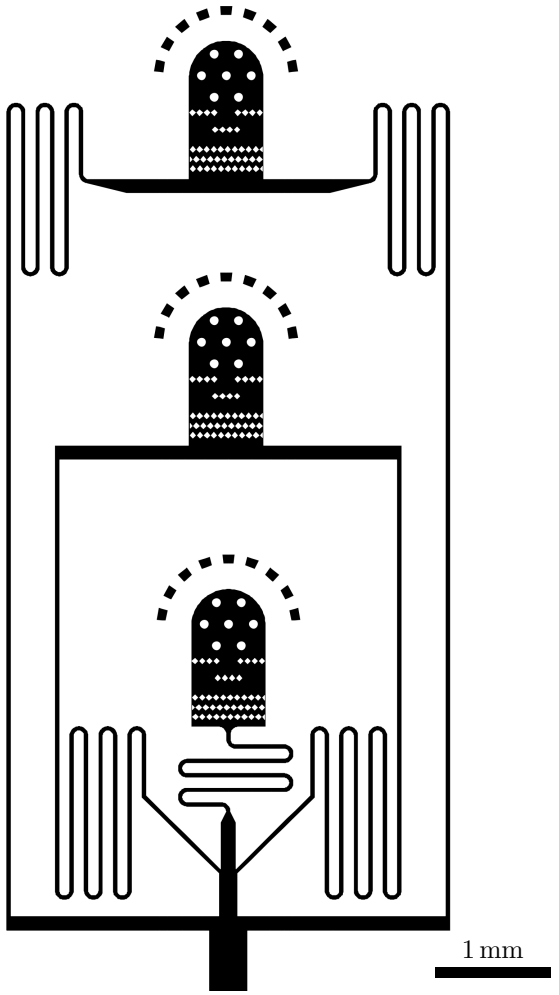

Figure C.3: Modified design 2: Narrow buffer channels